# NUMERICAL SIMULATION OF UNIFORM CIRCULAR MICROJET AND MONO DISPERSED MICRO DROPLET STREAMS FOR IMPINGEMENT COOLING

A Thesis

by

Syed Mohammad Hameed Ul Haq

Submitted to the Office of Graduate and Professional Studies of
Texas A&M University
in partial fulfillment of the requirements for the degree of

MASTER OF SCIENCE

| | |
|---|---|
| Chair of Committee, | Jorge Alvarado |
| Co-Chair of Committee, | Michael Pate |
| Committee Members, | Diego Donzis |
| Head of Department, | Andreas A. Polycarpou |

December 2018

Major Subject: Mechanical Engineering

# ABSTRACT

Effective cooling of electronic chips is essential for optimum performance. With the exponential growth of computers, there has been a sharp rise in the heat generation of these devices. Therefore, an utmost need has developed to utilize alternative cooling methods to ensure low operating temperatures. Some of the cooling techniques under consideration include spray cooling and jet impingement cooling. While jet impingement cooling is fairly easy to understand, Spray cooling still remains one of the most parameter intensive physical mechanisms. A common practice to simplify spray cooling is modeling it as a continuous stream of droplets, which is also followed in this study. A comparison between the two aforementioned techniques is necessary to understand which of them performs better for this particular application. For this purpose, a study based on computational fluid dynamics simulations was performed. Both cooling technique were simulated with parameters in line with the experimental conditions.

To accurately depict the impingement process and fluid flow, a 2D axisymmetric structured grid was constructed. For accurate spatial resolution, grid was refined using static mesh adaption for jets and dynamic mesh adaption for droplets. A time dependent patching method was utilized to simulate a single stream of droplets. A Volume of Fluid approach coupled with the Level Set method (CLS-VOF) was employed in ANSYS Fluent for simulating the flow. A good agreement was reached between experimental and numerical data for both cooling techniques, in terms of temperature profile, heat transfer coefficient, Nusselt number, impact crater diameter and film thickness in the impingement zone.

Heat transfer characteristics and hydrodynamics of jet impingement and droplet train impingement were compared and it was found that droplet train impingement outperformed the latter. Improved performance of droplet train impingement was due to the convective heat transfer across the surface, which was driven by fluid momentum. Droplet train impingement produced higher momentum across the impingement zone, compared to jet impingement, resulting in greater heat transfer. Higher momentum also led to larger crater diameters for droplet impingement. Despite its periodic behavior, a smooth temperature profile, with lower temperature gradients across the heat surface, was produced by droplet impingement as compared to jet impingement. This was attributed to the sweeping motion of the fluid at higher momentum, removing the generated heat, further away from the impingement zone. Thermal boundary layer of droplets was thinner than the thermal boundary layer of jets, indicating better heat transfer.

# ACKNOWLEDGEMENTS

It is with great pleasure that I write this thesis, final phase of research work for my Master's Degree. First and foremost, I would like to mention and whole heartedly express my gratitude to my research advisor, Dr. Jorge Alvarado. He was instrumental in guiding me through research work and always had the best ideas that put me on the right track. It was an honor being his student. Secondly, I would like to thank Jayaveera Muthusamy, who was always available to share his knowledge along with conducting his own research. Also, I would like to thank my co-chair, Dr. Pate and my committee member, Dr. Diego Donzis for their valuable input.

Personally, I want to mention my friends, Syed Ali Hasnain and Zain Hanif, whom I could always count on. Finally, I want to thank my parents, Mr. Muhammed Mobinul Haque and Mrs. Ghazala Mobin, for their continuous support and encouragement throughout my life. They made sure I was always loved and gave me the confidence to step up and achieve.

# CONTRIBUTORS AND FUNDING SOURCES

This work was supervised by a thesis committee consisting of Professor Jorge Alvarado and Professor Michael Pate of Department of Mechanical Engineering and Professor Diego Donzis of Department of Aerospace Engineering. This study was made possible with the availability of data from previous research, included in Chapter 4, conducted by Dr. Zhang and Dr. Muthusamy. All other work conducted for the thesis was completed by the student independently.

For conducting this study, all the support was provided from Texas A&M University with a special mention of the Texas A&M High Performance Computing center (HPRC).

# NOMENCLATURE

| | |
|---|---|
| $d_{impingement}$ | Diameter of impingement region |
| D | Diameter of the impinging fluid |
| $d_{cra}$ | Crater Diameter |
| $d_d$ | Droplet diameter |
| $d_{orf}$ | Orifice diameter |
| G | Mass Velocity |
| h | Heat transfer Coefficient |
| k | Thermal Conductivity |
| L | length of orifice plate |
| $q"_c$ | Critical heat Flux |
| $h_{fg}$ | Latent Heat of liquid |
| h | Heat transfer coefficient |
| $\dot{m}$ | Mass flow rate |
| P | Pressure |
| $r_j$ | Radius of the jet |
| $r_d$ | Radius of the droplet |
| R | Radial distance along heat surface |
| t | Time |

| | |
|---|---|
| T | Temperature |
| $T_i$ | Averaged Temperature at Time step i |
| $T_D$ | Temperature of the droplet |
| $T(r,z)$ | Instantaneous temperature |
| $T_w(r)$ | Temperature of the Wall at location R |
| Z | Vertical height from the heated surface |
| Nu | Nusselt Number $\left(\frac{h\,d}{k}\right)$ |
| Re | Reynolds Number $\left(\frac{\rho\,.\,V\,.\,d}{\mu}\right)$ |
| $V_R$ | Averaged Radial Velocity |
| Pr | Prandtl Number $\left(\frac{C_p}{\mu\,.\,k}\right)$ |
| α | Volume Fraction |
| $\rho$ | Density |
| $\emptyset$ | Level Set Function |
| $\sigma$ | Surface Tension |
| ɳ | Efficiency of Liquid Usage |
| $\delta_{Tdt}$ | Thermal boundary layer momentum thickness |
| $\bar{\bar{\tau}}$ | Averaged Fluid Shear Stress |
| μ | Dynamic Viscosity |

# TABLE OF CONTENTS

Page

# LIST OF FIGURES

Page

# LIST OF TABLES

Page

# CHAPTER I

# INTRODUCTION

Transistors have revolutionized electronics by reducing size of electronic devices to fit within our hands. However, there is a problem of significant heat generation per unit area in these devices that require effective heat dissipation. Failure to do so, results in decreased lifetime and reduction in performance. With semiconductors growth following the Moore's Law [2], it is fast becoming a necessity to come up with techniques to cool microprocessor chips with high heat transfer rates while maintaining the portability and dimensions of such devices. This can only be stressed by noting that one of the major causes of failure of electronic components is thermal overstressing [3]

Traditionally, forced convection of air is used as the primary form of heat dissipation technique, which is augmented by fins. This method of cooling remains useful for personal computers but it is not effective for large data centers, which then require temperature controlled environment to function optimally. Researchers have investigated liquid cooling methods as possible alternatives. Most of these techniques have shown capabilities to remove high thermal loads, with spray cooling and jet cooling being notable among them [4]. Graphical depictions of jet impingement and spray cooling systems can be seen in Figures 1 and 2, respectively.

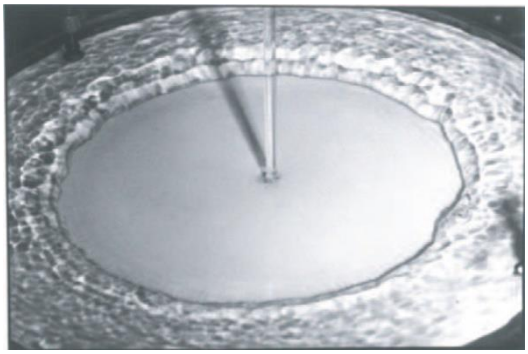

Figure 1. Jet Impingement phenomenon. Reprinted from Lienhard [5]

Figure 2. Spray cooling phenomenon. Reprinted from Spray cooling [6]

## 1.1 Motivation

Both of the aforementioned methods, namely jet impingement and spray cooling are widely employed, at a larger scale, in manufacturing processes of metal parts. However, in many circumstances, both methods involve phase change as a part of the cooling process [7-11]. Compared to spray cooling heat transfer, jet impingement heat transfer is relatively well understood due in part to its continuous nature. On the other hand, spray cooling is affected by several parameters, which are difficult to vary independently. Therefore, understanding spray cooling and the parameters affecting it are

still subjects of intense research. Although all the parameters of spray cooling cannot be factored into a single study, isolation of monodispersed droplets found in spray cooling system is a necessary building block for uncovering the key physical mechanisms of spray cooling. Very few studies are available that compare the heat transfer performance of uniform jets with droplet impingement. Lewis *et al.* [12] conducted a numerical study comparing heat transfer performance of both thermal management methods. This in part motivated the concurrent numerical study of droplet and jet impingement cooling.

## 1.2 Research objectives

The main objective of this numerical study is to probe and validate heat transfer performance of two forms surface cooling mechanisms, namely single microjet and single stream droplet impingement. Using microjets and mono dispersed droplets are used to cool down a heated surface, which resembles a microprocessor chip. To complete this objective, numerous cases were simulated to first understand the flow field of impinging jets and droplets before understanding their heat transfer characteristics. Hydrofluoroether (HFE-7100) was used as working fluid. All of these studies were performed at constant heat flux and constant wall-to-nozzle distance for both modes of cooling.

The jet impingement cooling phenomenon was studied in detail to understand the effect of flow rate and heat flux on the radial distribution of temperature on the cooled surface. Flow characteristics including film thickness, crater diameter and boundary layer profile were also analyzed to understand the effect of microjets to heat transfer performance. Experimental results obtained from Zhang [1] have been compared and validated with numerical data for different sets of flow and heat flux conditions. In the single stream impingement study, heat transfer characteristics including temperature

profile were investigated and analyzed for different flow rates. The effects of parameters such as droplet diameter, impingement velocity, droplet frequency, droplet Weber number (We) on the heat transfer performance were carefully examined. The relationship between droplet induced film hydrodynamics and heat transfer was analyzed. Like in the jet impingement cases, numerical results for droplet impingent were compared and validated with experimental data for different sets of flow and heat flux conditions.

Finally, a comparison of the two liquid cooling techniques was undertaken by considering identical flow and heat flux conditions.

## 1.3 Overview

This thesis presents validation of experimental heat transfer results from uniform microjets and microdroplet impingement cooling cases. It also includes heat transfer performance comparison of both methods. It begins with a literature review of previous studies undertaken by researchers in liquid cooling technologies with the main focus on jet impingement and spray cooling. Chapter III discusses the aspects numerical modeling of these physical phenomenon and the methodologies employed in the study, from grid generation to fluid models. Chapter IV presents the numerical results along with the experimental results of Zhang [1]. It also includes a comprehensive comparison of both methods from the heat transfer performance point of view. Chapter V includes concluding remarks and summary of the overall study.

# CHAPTER II

# LITERATURE REVIEW

## 2.1 Jet impingement cooling

Jet impingement has been used in industry for cooling heated surface and has garnered considerable interest over the years. Metals that are being formed or rolled are usually cooled using jets. At a smaller scale, it has been used for cooling electronic components.

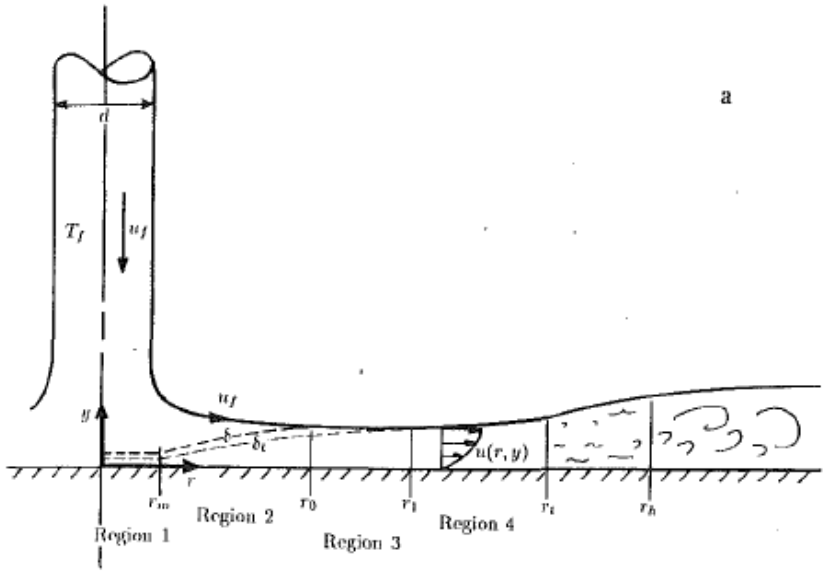


Figure 3. Reprinted from Watson's [13] radial division of jet impingement flow

Jet impingement phenomenon was first studied analytically by Watson [13]. As shown in Fig. 3, he broke up the circular jet flow in four successive regions radially, including the stagnation region, boundary layer region with surface velocity equal to the jet speed, and a region of viscous similarity with decreasing surface velocity. He postulated and proved that the film flow would be terminated by a hydraulic jump at a location independently controlled by downstream conditions. He also concluded that the

thickness of the film initially decreases and then increases with radial distance as viscous wall effects slow the spreading film. Watson employed both viscous similarity and momentum integral solutions. Watson's expressions were experimentally verified by Hashimo and Azuma [14] for the laminar boundary layer and similarity region velocity profiles and film thickness. They measured the turbulent transition radius in their system and also measured the subsequent velocity profiles. The turbulent film was well characterized by standard boundary layer results, but it did appear to slow down and return to laminar regime farther downstream as the film slowed while its stability increased.

Chen and Tseng [15] experimentally studied heat transfer characteristics associated with jet cooling, used in rolling processes. They investigated parameters including heat flux, heat transfer coefficient, cooling efficiency, and heated surface velocity and found that the effect of surface motion substantially influences local heat transfer behavior. Cooling efficiency and heat flux increased as surface motion increased. Moreover, decreasing the jet temperature led to higher heat transfer coefficient values. Furthermore, increasing jet velocity also led to increased heat transfer coefficient within the laminar regime. Based on their findings, they suggested that for controlled cooling, a planar jet system consisting of collinear jets is ideal. They also found out that circular jets should be arranged in a staggered configuration to achieve optimal performance. Seraj [16] numerically studied long free circular jets for steel cooling with Reynolds numbers between 16,669 and 50,068. Circular water jets were simulated by solving the Navier-Stokes equations using the finite volume method along with VOF method using FLUENT as solver. Higher velocity gradients were obtained for long turbulent jets, which led to enhanced heat transfer within the impingement zone. He also found that long water jets

resemble short jets before impacting the impingement zone. Within impingement zone, velocity increases linearly up to $r/d_{impingement}$ of 0.8.

Several investigations of jet impingement at a micro scale are also available in the literature. Lienhard [5] studied free surface with circular liquid jets, where he summarized theoretical and experimental results within the laminar stagnation zone. He used the analytical method devised by Watson [13] and provided a summary of correlations for fluid flow and heat transfer. He also studied turbulent jets and postulated that for turbulent jets, nozzle-to-surface distance is not relevant, within a certain range. He also studied the effects of heated surface roughness on heat transfer performance of jet impingement. Higher surface roughness resulted in better heat transfer and this effect was augmented as the Reynolds number increased. Behnia and Parneix [17] studied cooling of a heated pedestal on top of a surface by an axisymmetric isothermal fully developed turbulent jet to identify a correct model for computations. There computation domain is shown in Fig. 4. They compared different turbulence models to predict heat transfer results and validated them with experimental data. They concluded that normal-velocity relaxation model (V2F model) agreed very well with the experiments over a range of Reynold numbers. The local heat transfer coefficient exhibits a minimum in the stagnation region, which is rather different from the behavior of an impinging jet on a flat plate. It was noticed that the k-ε model does not properly represent the flow features, highly over-predicts the rate of heat transfer and yields physically unrealistic behavior. In all cases, the k-ε model excessively over-predicted the stagnant point. The V2F model was used to find out the relation between Nusselt number and Reynolds number ($Nu\ \alpha\ (Re)^{0.51}$ ) for heat transfer on top of the pedestal which was corroborated using published results [18].

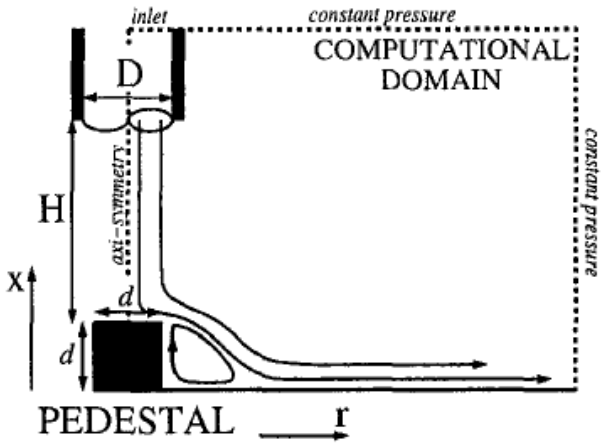


Figure 4. Domain used by Parneix and Behnia. Image reprinted from [17]

Liu *et al*. [19] conducted an experimental and analytical study of surface cooling using liquid jets cooling. They used their own previously developed integral solution, which divided the post impingement flow into regions based on thermal and hydrodynamic boundary layers. They developed separate equations for performance predictions for Prandtl number greater and less than 1.0, and for Uniform Heat Flux (UHF) and Uniform Wall Temperature (UWT) conditions. The experiments were performed with water at 4 °C to observe heat transfer performance of an undisturbed laminar jet. They measured the wall temperature distribution and calculated Nusselt number within the jet impingement cooling zone. These results were than compared with the predictions from the analytical solutions for different Prandtl Numbers ranges. The measurements agreed well with the predictions, and the maximum difference for Nusselt Numbers was less than 10%. More favorable agreement of heat transfer performance was obtained for liquid metal in the Prandtl number range of 0.1. They also studied the turbulent transition for post impingement flow at a transition radius for which a correlation was presented based on previous literature. Beyond this transition radius, a separate turbulent analysis was

constructed and a correlation was suggested. Narumanchi *et al*. [20] conducted a CFD study of a free surface single jet of water. They used the k-omega turbulence model with wall treatment and a Volume of Fluid (VOF) method for fluid interaction. They conducted a mesh independent study to make the solution up to 5% accurate. The Reynolds numbers varied from 3,000-46,000. The results were compared to experimental heat transfer coefficient data from Womac *et al*. [21], which were a reasonable match with a maximum difference of 20%. They also compared confined and submerged jet heat transfer performance, which showed better agreement. These results were then used to conduct a CFD study on insulated-gate bipolar transistors (IGBTs) used in hybrid vehicles. Water and glycol-water coolant were used to cool the IGBTs and the respective heat transfer performance was compared at various temperature and inlet velocity conditions. It was found that heat transfer performance of glycol-water mixture was almost half of water.

Chaudhari *et al.* [3] experimentally investigated the impingement heat transfer characteristics for synthetic jets of air. These jets were synthesized at the edge of an orifice by a periodic motion of a diaphragm creating a flow of Reynolds number between 1150–4180. They concluded that averaged heat transfer coefficient is affected by several geometric parameters including orifice diameter, length of the orifice plate and the orifice plate thickness. They also mentioned that Nusselt number is affected by different geometric ratios, one of them being L/d (length of orifice plate by orifice diameter). They presented a correlation based on their experimental data for Nusselt number for different L/d and Reynolds number, as follows.

$$\frac{Nu_{avg}}{Pr^{1/3}} = 7.624\,(Re)^{0.792}\left(\frac{L}{d}\right)^{-2.186}\left(\frac{R}{d}\right)^{2.258}\left(\frac{z}{d}\right)^{-0.632} \quad (1)$$

$7.86 < L/d < 22$
$1.5 < R/d < 4$
$1150 < Re < 4180$

Morris *et al*. [22] conducted a numerical study of turbulent jet impingement cooling using the k-ε model. They selected various configuration of jet impingement by varying parameters including Reynolds number, nozzle diameter, and Z/d (nozzle to target spacing). Heat transfer coefficient trend after impingement was plotted using the temperature profiles obtained from numerical simulations and compared with various Prandtl number models available in literature and experimental results of Garimella and Rice [23]. A bell-shaped heat transfer distribution was found from numerical simulations with the maximum value occurring at the stagnation point. The curves compared favorably (within 20%) with the experimental trend in the range $r/d < \pm 1.5$. Beyond this point, a sharp decrease in heat transfer coefficient trend was observed in numerical simulation results, which led a significant underprediction of averaged heat transfer coefficient. In summary, the experimental results and numerical predictions compared well.

In summary, jet impingement has been investigated in detail with experiments. Analytical solutions of heat transfer performance are also available, which have been validated by numerous experimental studies. These publications [8, 13-16, 19, 21, 23-28] show various configurations of single jets and jet arrays for surface cooling and comparisons with other cooling processes. Several correlations are also available in publications for Nusselt number values at the stagnation point and beyond [28]. Numerical studies that employ CFD for liquid jet impingement heat transfer are mostly available for turbulent jets. Limited literature is available for laminar liquid jets.

## 2.2 Spray cooling

Spray cooling is a phenomenon whereby a spray of small droplets impinge on a heated surface. Spray cooling is a very effective cooling mechanism even without phase change (boiling) or evaporation [29]. Sprays are formed by supplying high pressure liquid through a small orifice or by atomizing the liquid particles using high pressured air. Researchers have been interested in understanding spray cooling as a physical phenomenon and efforts have been made to control and change its parameters.

Moriyama *et al*. [10], theoretically and experimentally, studied and measured heat transfer coefficient in spray cooling. He suggested a heat transfer coefficient prediction equation, which was derived starting from heat extraction per droplet impinged onto hot surfaces.

$$h_s = \frac{1.584\ \rho\ h_0\ q_w \overline{D^4 v}}{\pi \sigma (d_{30})^3} \tag{2}$$

This expression accounts for the drop size and velocity distributions at any specified location in sprays, as well as both dynamic and thermal behavior of each droplet impinging onto the hot surface. Comparing the theoretical local heat-transfer coefficient, with the results obtained by analyzing the experimental data, it was apparent that their theory was fundamentally valid.

Chen *et al*. [30] conducted multiple studies using different types of nozzles to study the effects of droplet velocity, droplet per time and droplet diameter on cooling of a heated surface. They varied one parameter at a time while keeping the rest constant. They were able to determine that the droplet velocity is the principal factor that affects the critical heat flux (CHF) and heat transfer coefficient, followed by droplet flux. Increasing these

parameters resulted in an increasing heat transfer coefficient and critical heat flux. Sauter diameter, which is averaged droplet diameter, in case of spray cooling, did not have a noteworthy impact on heat transfer performance. In a follow up study [31], Chen *et al*. investigated the dependence of the efficiency of liquid usage (ɳ) at CHF. Efficiency of liquid usage was defined as the ratio of ratio of the critical heat flux ($q_c$") over the latent heat of the liquid ($h_{fg}$) and flux delivered by the spray nozzle.

$$\eta = \frac{q"_c}{G\ h_{fg}} \tag{3}$$

Using regression analysis on an experimental data, they found the following relations:

$$\eta \propto N^{-\frac{2}{3}} \quad (Droplet\ Flux)$$

$$\eta \propto {d_{32}}^{-\frac{14}{5}} \quad (Sauter\ Dia)$$

$$\eta \propto V^{\frac{1}{4}} \quad (Droplet\ Velocity)$$

Also, they found out that

$$CHF \propto N^{\frac{1}{6}} \qquad CHF \propto V^{\frac{1}{4}}$$

Based on their finding, they were able to conclude that for producing maximum CHF with the lowest amount of water, a nozzle had to be selected that kept the droplet diameter small but allowed high droplet velocities.

Cheng *et al*.[32] conducted an experimental study on spray cooling that measured temperature distribution of a heated surface using infrared as well as thermocouples. The surface temperature non-uniformity and its influencing factors were analyzed. A mathematical model for heat transfer characteristics was suggested that divided the flow

into five regions, namely 1) impaction heat transfer, 2) film surface convection heat transfer, 3) environmental heat transfer 4) surface nucleation bubbles and 5) secondary nucleation bubbles. Based on the mathematical models, a numerical simulation was performed, which produced agreeable results with the experimental data. The surface temperature non-uniformity was found to be effected by the spray characteristics, nozzle-to-surface distance, inlet pressure of the nozzle, heat flux, spray angle and the system pressure. It was also observed that temperature non-uniformity of spray cooling was very sensitive to nozzle-to-surface distance. However, it was not a monotonic function of this parameter and reduced after reaching a peak value. Furthermore, it was also noted that non-uniformity increased with a decrease in inlet pressure. Heat flux values were found to be linearly proportional to non-uniformity. In the case of the same heat flux, the surface temperature non-uniformity was reduced by the small spray angle, low system pressure, low nozzle-to-surface distance, and the high inlet pressure.

Mudawar and Estes [33] studied the cooling of hot surface using Fluorinert FC-72 and FC-87. They built a theoretical model to predict the volumetric distribution of liquid per unit area per unit time and used it to calculate critical heat flux. These results were validated using experimental data in which they also determined the effects of nozzle-to-surface distance on the heat transfer performance specifically the critical heat flux. It was found that CHF can be maximized when the spray was constructed in a way that spray just imposed on the square surface of the heater. A correlation for prediction of critical heat flux was presented for a broad range of nozzles with different flow rates.

Theoretical and numerical simulations of droplet impingement processes, as they relate to spray cooling applications, have been undertaken by several researchers as described in greater detail below.

## 2.3 Droplet impingement cooling

Droplets are generally produced by spray nozzles, which generate non-uniform sized droplets with different velocities. To simplify the study of spray cooling, researchers have isolated droplets from spray cooling phenomenon. This way, the numbers of parameters are manageable.

Figure 5. Droplet train imaging conducted by Zhang [1] and Muthusamy [24]. Image reprinted from Zhang [1]

Zhang [1] and Muthusamy [24] investigated droplet impingement hydrodynamics using dielectric engineered fluid, HFE-7100. Zhang [1] conducted experiments, producing a steady stream of droplets, as shown in fig. 5. Muthusamy [24] performed a numerical study to understand the effect of droplet velocities, droplet collision and breakup, effect of Weber number on spreading and splashing of droplets after impingement. He conducted multiphase computational fluid dynamics (CFD) simulations using Volume of Fluid (VOF) method. He found out that for a single stream of droplets, the smooth spreading was limited to Weber numbers less than 280, and transition from spreading to splashing occurred between Weber numbers 280 and 489. Numerically calculated film thickness showed that higher frequency of impingement led to thinner film post impingement. Hass and Wenhoff [34] simulated nano-droplets using molecular dynamics (MD) impingement

on a heat surface. They found that critical droplet temperature exist as a function of droplet size and confirmed the previous findings that maximum heat transfer occurs at droplet impact zone.

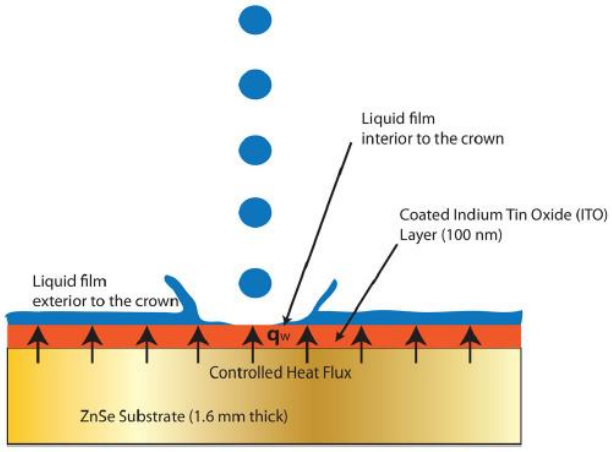


Figure 6. Droplet impingement simulation. Reprinted from Trujillo *et al.* [35]

Trujillo *et al.* [35] studied mono dispersed droplet impingement in a combined experimental and numerical study using an HFE-7100 droplets striking a prewetted surface, as depicted in fig. 6. In the experimental study, an infrared thermography technique was used to measure the temperature distribution of the surface. Heat flux was varied to investigate the heat transfer behavior of periodic droplet impingement at the solid–liquid interface. Temperature profiles found experimentally were validated using numerical simulations using commercial CFD code. They found that temperature distribution inside the crater region was found to be significantly reduced. Due to the radial flow originating from each successive droplet impact, the fluid inside the crater walls remained well below its saturated value. No evidence of bubble nucleation was observed in this region providing further evidence of the single phase cooling nature in the vicinity

of droplet impact locations. Therefore, convective heat transfer was concluded to be the main driving force for this heat transfer.

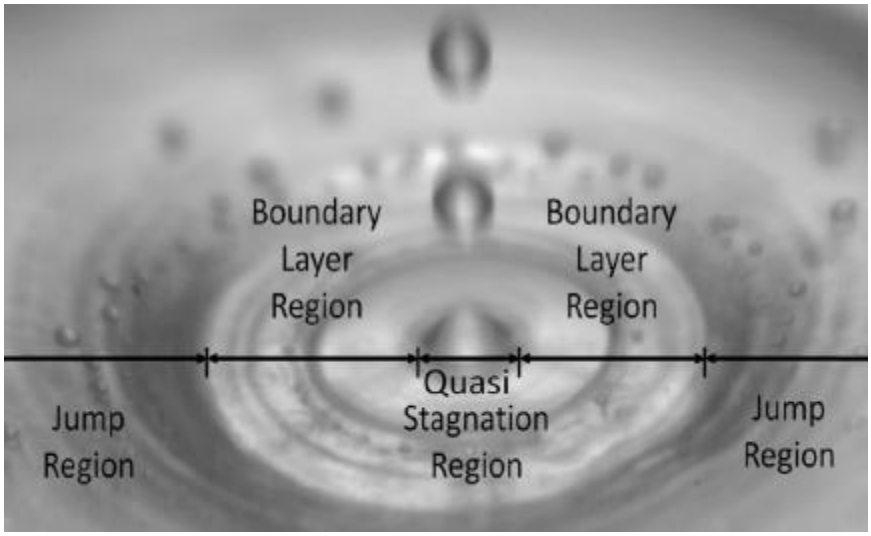


Figure 7. Droplet impingement imaging. Reprinted from Soriano *et al*. [36]

Soriano *et al*. [36] experimentally studied single and multiple streams of impinging droplets using HFE-7100 as the cooling liquid under constant heat flux condition. Film thickness inside the impact crater was measured using the Total Internal Reflection (TIR) technique. Hydrodynamic phenomena of the droplet impact craters were analyzed using a high speed imaging technique, as shown in fig. 7. The study supported the notion that forced convection is the main heat transfer mechanism inside the impact crater mainly due to the high frequency and periodic nature of droplet impingement. It was found that flow rate, droplet impingement frequency, velocity and spacing between adjacent impinging droplet streams play significant roles in film dynamics and heat transfer behavior Furthermore, droplet impingement regimes such as spreading and splashing were observed to play an important role in the overall heat transfer behavior. Additionally, the

postulated CHF correlation for single droplet stream impingement was in good agreement with literature.

## 2.4 Comparative study of single stream droplets and free surface liquid jets

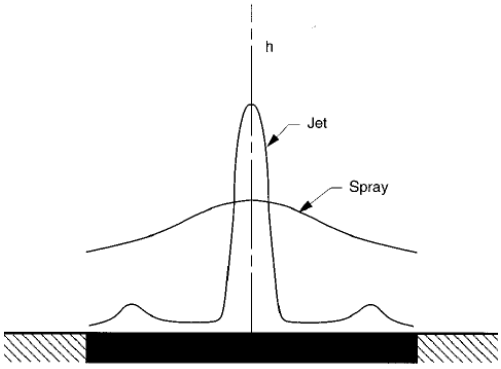


Figure 8. Heat transfer coefficient spatial variation of jet and spray variation. Reprinted from Mudawar. [33]

A comparison of liquid cooling techniques, jet impingement and droplet impingement has been previously done in the literature. Mudawar [4] compared several cooling mechanisms for heated surfaces. He compared spatial variation of heat transfer coefficient across the surface, as shown in Fig 8. Lewis *et al*. [12] did a numerical study comparing free surface jet with uniform velocity profile, free surface jet with fully developed velocity profile and monodispersed droplets using a commercial CFD code OpenFOAM. A Volume-of-Fluid (VOF) method was used to model multiphase flow. They compared fully developed and partially developed jets with droplets. Results showed that jet configurations have better cooling performance than the droplet train, locally and globally, with the fully-developed case being the most effective of the two jet arrangements for the same flow rate and velocity. Under the conditions of the study, the free surface jet had a noticeably smoother hydrodynamic and thermal transition from the

stagnation region to the far field when compared to the droplet train, as depicted in fig. 8. They also concluded that liquid film within the impingement region of the droplet train exhibited pronounced variations in velocity magnitude and film thickness. As a result, there was a larger area being effectively cooled in the jet impingement cases, as measured by the smaller radial profiles of thermal boundary layer thickness and the higher heat transfer coefficients.

Zhang [1] conducted experimental study for his PhD dissertation comparing a droplet impingement cooling and jet impingement cooling. Studies were performed at fixed flow rate and fixed orifice diameter conditions. Properties of the droplet trains and jet impingement were exactly the same. He observed that droplet train impingement leads to higher crater diameter (about 30% more) at fixed flow rate conditions. He confirmed previous findings related to convective heat transfer as being the main mechanism of heat transfer. Results suggested that the periodic droplet-induced crown propagation lead to a more effective mixing of the cooling liquid. Overall, his results showed that circular jets were outperformed by monodispersed droplets.

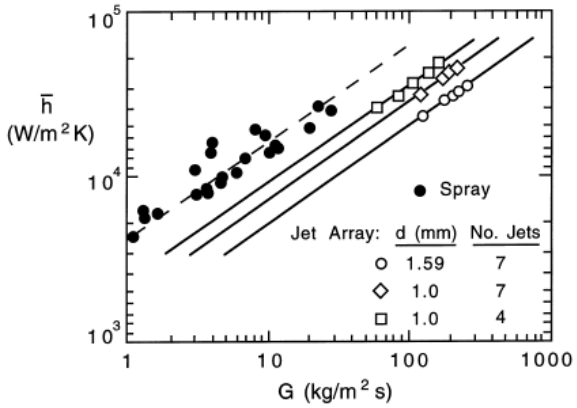


Figure 9. Jet impingement and Spray cooling heat transfer coefficient variation. Reprinted from Oliphant [37]

Oliphant *et al*. [37] conducted an experimental study comparing jet array impingement and spray cooling at non-boiling temperatures. As shown in Fig. 9, they observed that spray cooling had its heat transfer coefficients in the same order of magnitude as jet array cooling despite having very different mass flux values. If the spray cooling data were extrapolated into the jet mass flux region, it was seen that the spray impingement was significantly more effective than the liquid jet arrays. It was suggested that both these methods could have different heat transfer mechanisms. While jets array led to a continuous flow resulting in a thicker boundary layer, sprays formed a thinner boundary layer.

## 2.5 Gaps in research knowledge

There is a significant amount of literature available for jet impingement, spray cooling and single droplet train impingement cooling. For jet impingement, several experimental studies can be found, which have been validated using analytical methods. However, numerical studies using finite volume methods are not widely available. Furthermore, not all of these studies have been experimentally validated. Droplet train impingement cooling studies for single, double and triple streams were conducted by my fellow graduate student, Muthusamy [24] using CLS-VOF approach. The results showed good agreement between experimental and numerical data.

Focusing on comparative studies of jet impingement and droplet train impingement cooling, Zhang [1] had a part of his PhD dissertation devoted to experimental comparison of single droplet train impingement with circular jets. Although there are several studies showing individual performance of these cooling mechanisms, there is little to no experimental or numerical research solely on the comparison of these methods. Most of the published work has been either experimental or numerical analysis without explicit or direct validations. Moreover, the studies mentioned above differ in their findings with Zhang [1] and Oliphant [37] stating that droplets perform better in cooling heated electronics while Lewis *et al*. [12] results show jets outperform droplet impingement. Therefore, a detailed analysis that shows and compares results from both experiment and numerical methods of jet impingement and droplet train impingement still is needed.

## 2.6 Study objectives

For the purpose of identifying a better liquid cooling technique and gaining a better understanding of heat transfer of droplet train impingement cooling and jet impingement cooling, numerous numerical simulations have been performed with specific objectives. Tables 1 and 2 show the parameters and test matrix, respectively. Main tasks for this study are as follows:

- Visualize the hydrodynamic and thermal profiles of both impingement processes and relate them to heat transfer performance. This is done by finding
    - Fluid Crater diameter
    - Liquid Film thickness
    - Velocity profiles after impact, from within impingement zones up to crater diameter
    - Temperature variation of the plate within impingement zone
    - Complete Temperature profile of the heated plate
- Understand the effects of flowrate on the heat transfer performance of impingement cooling
- Validate the heat transfer numerical data with the experimental data
- Compare both forms of impingement cooling processes and identify the one that results in better cooling of the heated place

Experimental results obtained by Zhang [1] were available for validating the numerical results.

Table 1. Parameters of the numerical study

| **Parameters** | **Impingement Cooling Method** | |
|---|---|---|
| | **Circular Jet** | **Mono dispersed Droplets** |
| **Cooling Fluid** | HFE-7100 | HFE-7100 |
| **Flow Rate (mL/hr.)** | 180/210 | 180/210 |
| **Velocity (m/s)** | 2.83/3.3 | 3.52/3.99 |
| **Weber Number** | N/A | 328/443 |
| **frequency (Hz)** | N/A | 6300/6500 |
| **diameter of orifice (μm)** | 150 | 150 |
| **diameter of flow (μm)** | 150 | 237/249 |
| **Heat Flux (W/cm$^2$)** | 3.6 | 3.6 |

Table 2. Test matrix for numerical study

| **Flow Rate:** | **180, ml/hr.** | **210, ml/hr.** |
|---|---|---|
| **Heat Flux (W/cm$^2$)** | 3.6 | 3.6 |
| **Cooling Fluid** | HFE-7100 | HFE-7100 |
| **Impingement Mode** | | |
| **Circular Jet** | X | X |
| **Mono dispersed Droplets** | X | X |

# CHAPTER III

# NUMERICAL MODELING SETUP

## 3.1 Computational fluid dynamics and its advantages

Studying and visualizing a physical phenomenon at a micro level is practically challenging. It requires precise instrumentation and high speed visualization equipment. Not only does it take considerable effort to design and build a set up for such investigations, the cost involved is also considerable. Although there is no alternative for real life experimental results, conducting experiments without prior knowledge of the physical behavior under consideration can result in several unsuccessful attempts. Numerical modeling techniques rely on iterative calculations of algebraic equations that are approximates of partial differential equations (PDEs) that represent different physical phenomena. Numerical methods have been available for a while but there effectiveness was limited due to lack of computational power. With the advent and open availability of advance computers with sizeable memories, numerical techniques are now widely employed to understand and predict physical phenomena.

Computational fluid dynamics is a numerical technique employed by experts to solve complex fluid flow and heat transfer problems. It uses a finite difference scheme to approximate PDEs such as Navier-Stokes equation and Euler equation. Nowadays, CFD methodologies are routinely employed in the fields of aircraft, turbomachinery, car, and ship design [38]. Fig. 10 shows a standard CFD analysis process [39] employed widely in the industry and academia.

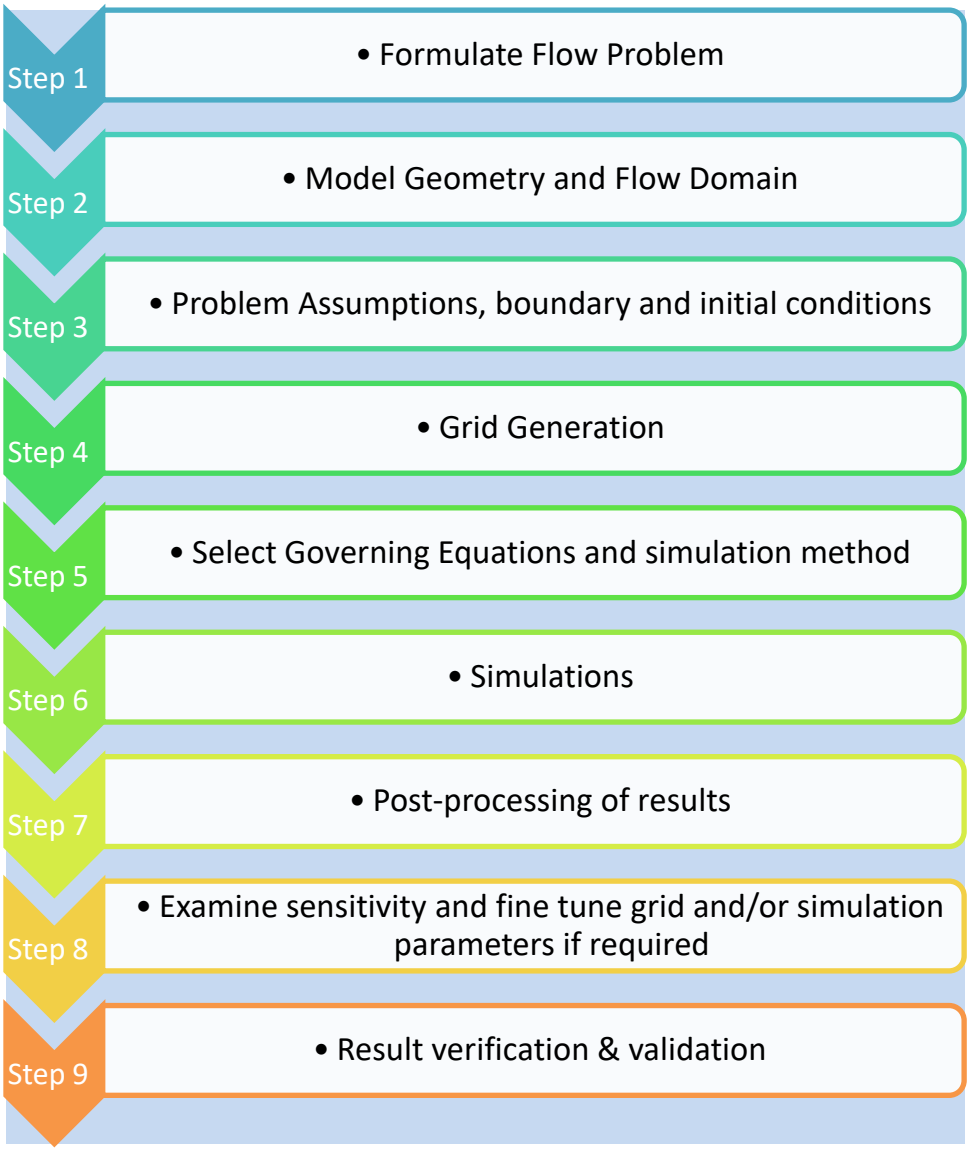


Figure 10. Flow Diagram for CFD Analysis

## 3.2 CFD approach

As detailed in Chapter I and II, the objective of the study was to conduct numerical simulations to better understand and compare surface cooling capabilities of two liquid cooling techniques, namely, jet impingement and single stream droplet impingement. These numerical results are also to be validated using the experimental data presented by Zhang [1]. First step towards achieving this objective is setting up the numerical models for each of these techniques. All of the numerical modeling and simulations have been done using ANSYS®.

### *3.2.1 Fluid selection and cooling technique definition*

The fluid used for this investigation is an engineering fluid called HFE-7100 ($C_4F_9OCH_3$). It is manufactured by 3M™ Novec™ and has several applications including usage as lubricant carrier, water drying agent and for surface cooling applications [40]. One of its most well-known applications is in the BitFury's 40MW data center that employed two-phase immersion cooling. The properties that make it an ideal cooling liquid for electronics is its low boiling point and its dielectric properties [24]. Past literature shows that this liquid has been used widely. Muthusamy [24] used it for his droplet steam impingement simulations. Lewis *et al.* [12] used it for his numerical comparison of jet impingement and droplet train impingement cooling techniques and Zhang [1] utilized it for his experimental research. Since the results from this study were to be validated with experimental data sets from Zhang [1], HFE-7100 was chosen as the liquid for all the numerical simulations. Fluid properties are shown in Table 3.

Table 3. Properties of 3M Novec HFE-7100

| Property | Value |
|---|---|
| Density ($\rho$) | 1520 kg/m$^3$ |
| Dynamic viscosity ($\mu$) | 6.1 x 10$^{-4}$ Pa-s (6.1 x 10$^{-5}$ Poise) |
| Thermal conductivity ($k$) | 0.07 W/m-K |
| Specific heat ($c_p$) | 1173 J/kg-K |
| Surface tension ($\sigma$) | 1.36 x 10$^{-2}$ N/m |
| Saturation point, ($T_{sat}$) | 61 ºC (141 F) |
| Latent heat of vaporization ($h_{fg}$) | 111.6 kJ/kg |

This fluid did not exist in the ANSYS® Fluent Database and had to be modeled using the properties provided by the manufacturer.

The second fluid in the simulation is air. It is based on the properties present in ANSYS® Fluent Database. Air occupies the locations where HFE-7100 is not present. Material Properties of air used in simulations are shown in Table 4.

Table 4. Material properties of air

| Property | Value |
|---|---|
| Density ($\rho$) | 1.225 kg/m$^3$ |
| Dynamic viscosity ($\mu$) | 1.7894x10$^{-5}$ kg/m-s |
| Thermal conductivity ($k$) | 0.0242 W/m-K |
| Specific heat ($c_p$) | 1006.43 J/kg-K |

The fluid flows under investigation are uniform circular jet and droplet train that impinge on a heated surface with constant flux, and spread radially. Both of these techniques can be found in previous literature [3,5,9,12]. Since the jet is circular and droplets are spherical, the fluid spreads radially; therefore, the flow problem can be assumed to be axisymmetric.

Fig. 11 shows a visual representation of the jet impingement on a heated surface. A hydraulic jump occurs after the fluid has spread and passed a certain threshold value along the radial direction. Moreover, the hydraulic jump eventually leads to the formation of a crater. After a while, the flow reaches hydrodynamic stability within a central region of low film thickness and surrounding region of higher film thickness. A numerical model has been created to replicate the stable, post impingement fluid profile.

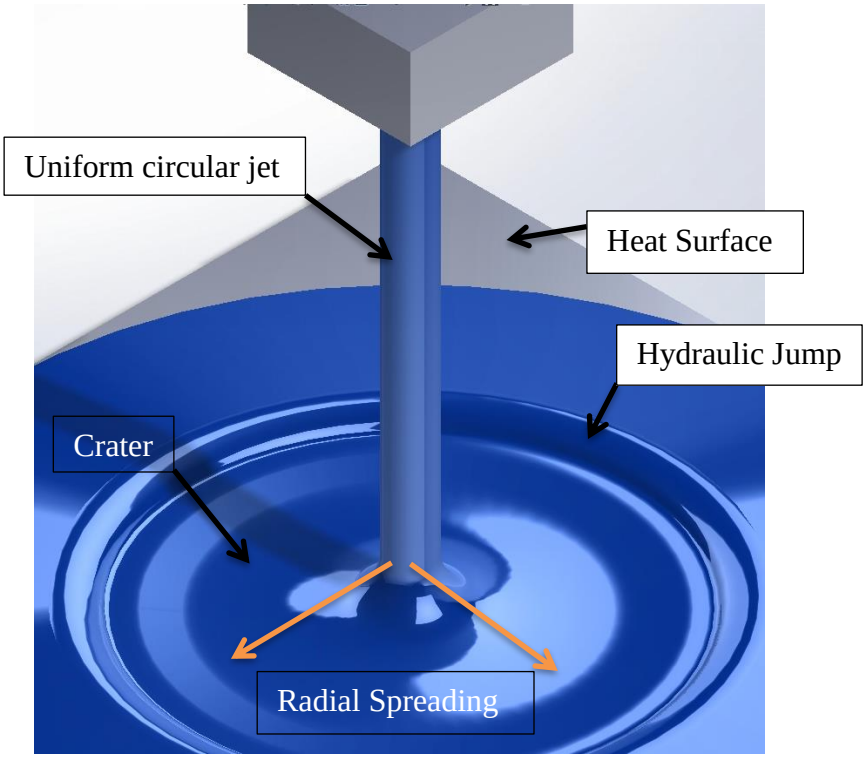


Figure 11. Jet Impingement model

Fig. 12 shows expected fluid behavior with the droplet train impingement onto a heated surface. Upon reaching hydrodynamic stability, it forms a crown shape in the impingement zone from continuous droplet impingement. The fluid spreads radially; therefore, it could be modeled axis-symmetrically. The figure also shows visual representation of important parameters such as droplet spacing and droplet diameter.

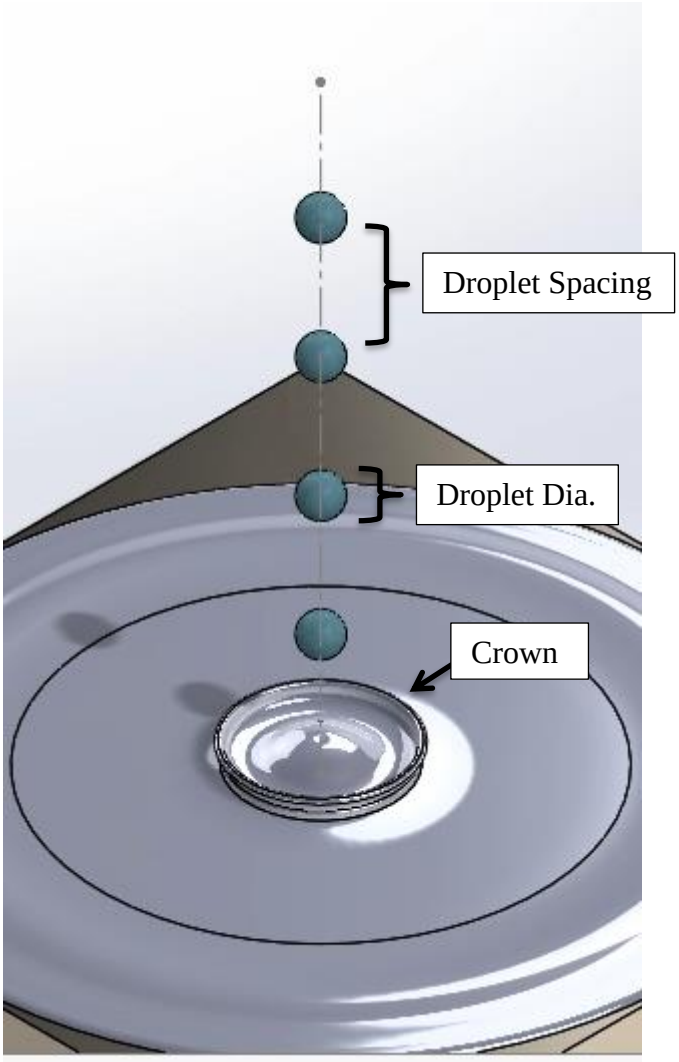


Figure 12. Droplet Train Impingement model

*3.2.2 Physical domain of droplet and jet cases*

In order to simulate the fluid and heat transfer behavior of jet and droplet impingement, a system similar to the experimental arrangement was setup. The simulation system consisted of heater assembly and a fluid domain, as described below.

3.2.2.1 Heater model

Simulation of droplet and jet impingement involved modeling of the heater. In the experimental setup, a three layered assembly was used to create a heated surface. The three layers and their respective properties are shown in Table 5.

Table 5. Material properties and thickness of the heater

| **Material** | **Thickness** | **Thermal Conductivity (W/m-°C)** | **Thermal diffusivity ($m^2/s$)** |
|---|---|---|---|
| **Indium Tin Oxide (ITO)** | 190 nm | 8.7 | 3.6E-06 |
| **Silicon dioxide ($SiO_2$)** | 650 nm | 1.3 | 6.6E-07 |
| **Sapphire Substrate ($Al_2O_3$)** | 0.25 mm | 23.0 | 9.9E-06 |

As shown in Fig. 13, a 10 mm by 10 mm by 0.25 mm thin sapphire substrate, polished on both sides, was used as a base for the assembly. The heater element also had a 190 nm ITO coating on top of the $SiO_2$. A 650 nm $SiO_2$ coating was applied to ensure better emissivity [41]. The ITO layer was used to generate volumetric heat flux *in-situ*. A 1500W power supply was used to generate uniform heat flux throughout the heating element.

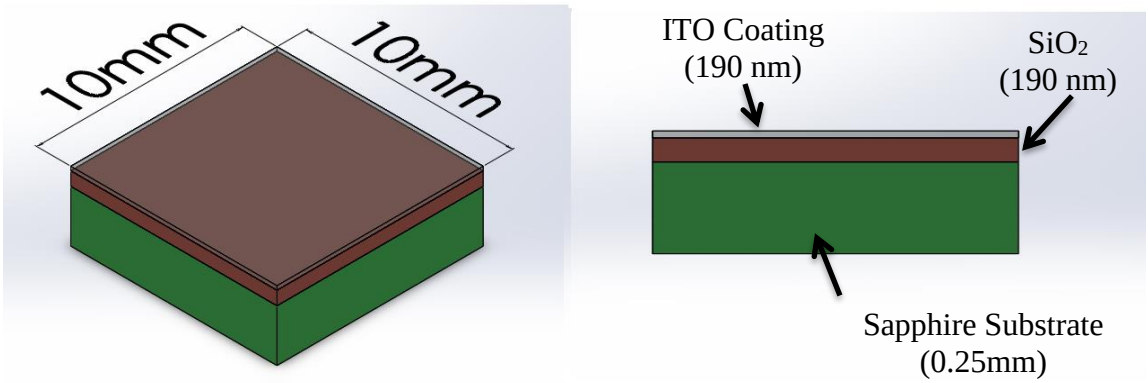


Figure 13. Heater assembly schematic (NOT TO SCALE)

For simulations, the heater assembly was modeled with identical thicknesses and material properties. Three layers of solids were made in ANSYS Geometry using the properties shown in Table 4. To simulate the heat generation, a *volumetric heat source* option was selected in ANSYS Fluent for the ITO layer to ensure comparability with the experimental results.

3.2.2.2 Fluid domain

As mentioned before, these fluid flows were found to be axisymmetric experimentally; therefore, a 2D circular vertical section was used as domain. From previous literature [5, 9, 35-37, 42], it was observed that after jet impingement, fluid spreads radially and forms a thin layer on the heated surface and later experiences a hydraulic jump. For droplet train impingement, past publications [12, 24, 34-36, 43] show that a crown is formed, which propagates radially within the impingement zone. A hydraulic jump is also observed later as the flow spreads as gravity and surface tension effects become dominant. Considering the aforementioned fluid behavior, the fluid

domain had to be sized appropriately to show the entire fluid phenomena observed in jet impingement as well as in droplet train impingement cases.

To size the fluid domain appropriately, the distance from the center of jet impingement to the hydraulic jump, called the crater diameter ($D_{crater}$) was used explicitly for that purpose. Maximum crater diameter value from different sources for the same flowrate (225 ml/hr.) are shown in Table 6, which were used for establishing fluid domain in the current study.

Table 6. Jet impingement crater diameter values in literature

| **Literature** | **$D_{crater}$ (µm)** |
|---|---|
| **Zhang [1]** | 1980 |
| **Bohr *et al.* [44]** | 1755 |
| **Aristoff [26]** | 2740 |

Muthusamy [42] reported a crater diameter of 2600 µm for 225 ml/hr. in his CFD simulations to study crown propagation and hydraulic jump of droplet train impingement. All the cases in the current study had lower flowrates than Muthusamy's [24]. Based on these values, a domain with radius of 3000 µm (3 mm) was considered suitable for the current study.

The second dimension of the 2D domain was the nozzle-to-surface distance. Zhang [1] selected a height of 5 mm in his experiments for jets, because he had to ensure the jets were circular, stable and fully developed when they impinged the heated surface. In order to create a stream of droplets, he used a piezoelectric droplet generator for breaking up jets into a stream of monosized droplets. In CFD simulations, jets remained circular due

to the axisymmetric nature of the simulations, which was in line with experimental observations. Furthermore, a uniform velocity profile was imposed at the inlet of the fluid domain, which developed before impinging the heated surface. In the case of droplet impingement, droplets were generated using a time dependent patching method to avoid simulating the complete jet breakup into monosized droplets. To reduce computational time even further, a nozzle-to-surface height of 2 mm was selected, as shown in Fig. 14.

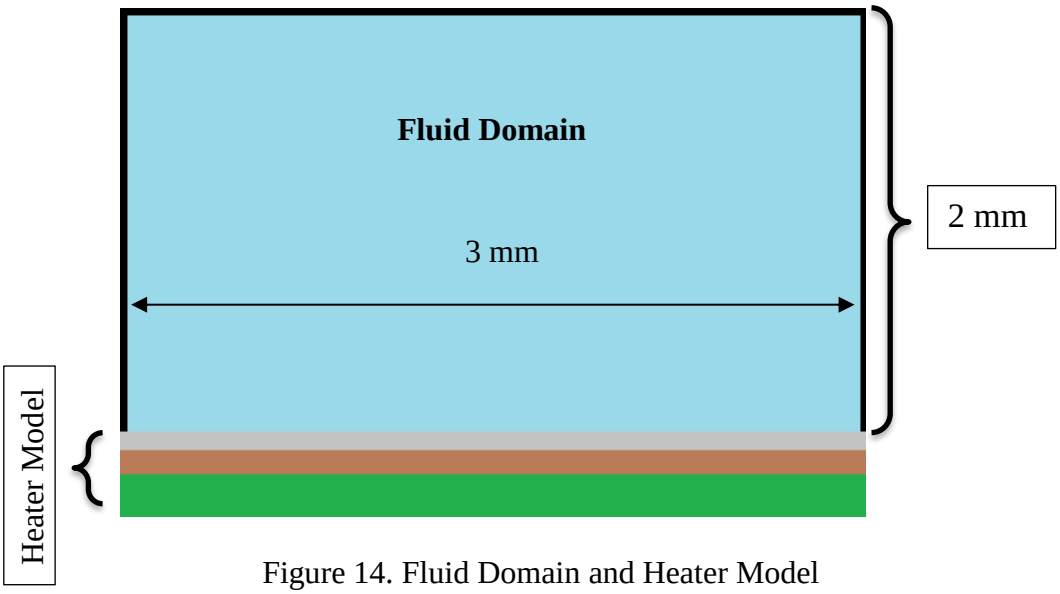


Figure 14. Fluid Domain and Heater Model

*3.2.3 Problem assumptions and boundary conditions*

3.2.3.1 Problem assumptions

Setting up a CFD simulation requires making certain assumptions regarding fluid flow. Reasonable assumptions can lead to an accurate solution while saving computational time and cost. For this study, several assumptions were made based on preliminary simulations and experimental results [1].

For jet impingement and droplet train impingement cases, it was vital to know the fluid flow regime within the impinged liquid film. Accordingly, a film Reynolds number was defined to characterize fluid flow within the impingement zone. A critical Reynolds number value for flow over a flat plate was used as benchmark. Film Reynolds number was defined as follows:

$$Re_{film} = \frac{\rho \overline{V_R} R}{\mu} \tag{4}$$

$Re_{film}$ values for all the jet impingement and droplet impingement cases were between 410 and 3000. For flow over a flat plate, it is known that flow becomes turbulent after Reynolds number values exceeds $5x10^5$ [45]. In comparison with flat plate Reynolds number, $Re_{film}$ values from the current study, it was evident that the surface flow was in the laminar regime. Therefore, for simulations, a laminar fluid flow model was selected for fluid flow within the impinged liquid film. This assumption was supported by several publications, which utilized similar parameters [12, 24, 35-37]. The same studies assumed and used a 2D axisymmetric domain for the simulations. For laminar jets, Lewis *et al.* [12] also used a 2D axisymmetric model in his numerical study. For droplets, Muthusamy [24]

also utilized a 2D axisymmetric models for droplet spreading and transitional cases upon impingement, which produced results in agreement with the experimental data sets.

To find out if gravity and surface tension effects should be considered in the simulations, Froude number and Capillary numbers were calculated, as follows:

$$Fr = \left(\frac{V}{(L * g)^{0.5}}\right) \tag{5}$$

$$Ca = \frac{\mu * V}{\sigma} \tag{6}$$

where
$V$ = Averaged fluid velocity
$\mu$ = Viscosity
$L$ = Characteristic length (droplet/jet diameter
$\sigma$ = Surface Tension
$g$ = gravitational acceleration

For jet impingement cases, Froude number varied between 73 and 86, signifying that inertial forces acting on the jet were much greater than gravitational forces. Therefore, gravitational effects were ignored. It needs to be noted here that flow after jet impingement had Froude number values close to 1, esp. within impingement zone. Therefore gravity effects were considered for post impingement flow. Capillary number was significantly less than 1 for jet impingement cases. Therefore, the surface tension effects were deemed important. Also, this strengthened the argument that fluid flow, before and after impingement, would remain symmetrical. Droplet train impingement cases had similar values for Froude and Capillary numbers. Since surface tension effects were important and more dominant than viscous effects, the smooth and symmetrical droplet train was expected to form during the crown propagation process.

The only assumption related to heat transfer was that HFE-7100 did not evaporate at any instant during the simulation. To keep this assumption valid, heat flux values were selected to ensure that temperatures did not reach the saturation point of the liquid.

3.2.3.2 Boundary conditions and initial conditions

A 2D axisymmetric domain of the same size was selected for both liquid cooling techniques. This has been previously discussed in the Physical Domain section. Various boundary conditions were applied to the physical domain in order to simulate these cooling techniques. Several boundary conditions were common to both cooling techniques. These conditions are detailed in Fig. 15.

As detailed before, the fluid flow was simulated using an axisymmetric domain, which required an axis of rotation. As shown in Fig. 15, the left vertical edge of the domain was selected as the axis of rotation. To simulate a fluid nozzle, a 75 μm face at the top left corner of the domain was used as boundary condition or fluid inlet, where a prescribed fluid velocity was imposed. The size of the face was selected to match the orifice diameter used by Zhang [1] in his experimental setup. In the Physical Domain section, a three-layered subsystem was used to represent the heater assembly, which was used to impose constant heat flux as in the experimental system. For this purpose, a volumetric heat flux of $1.9 \times 10^{11}$ W/cm$^3$ was applied to the 190 nm ITO solid layer. The upper surface of the ITO solid was defined as a solid wall with a no-slip boundary condition ($u$=0). A pressure far-field boundary condition was applied to the top surface to model a free-stream condition of air. The side surfaces were set to 0 Pa. At $t$ = 0 for each case, a HFE-7100 liquid layer of thickness 125 μm was patched over the heated surface, which was within the same order of magnitude of the experimental film thickness

measurements. This was done to accelerate hydrodynamic convergence of both fluid flows.

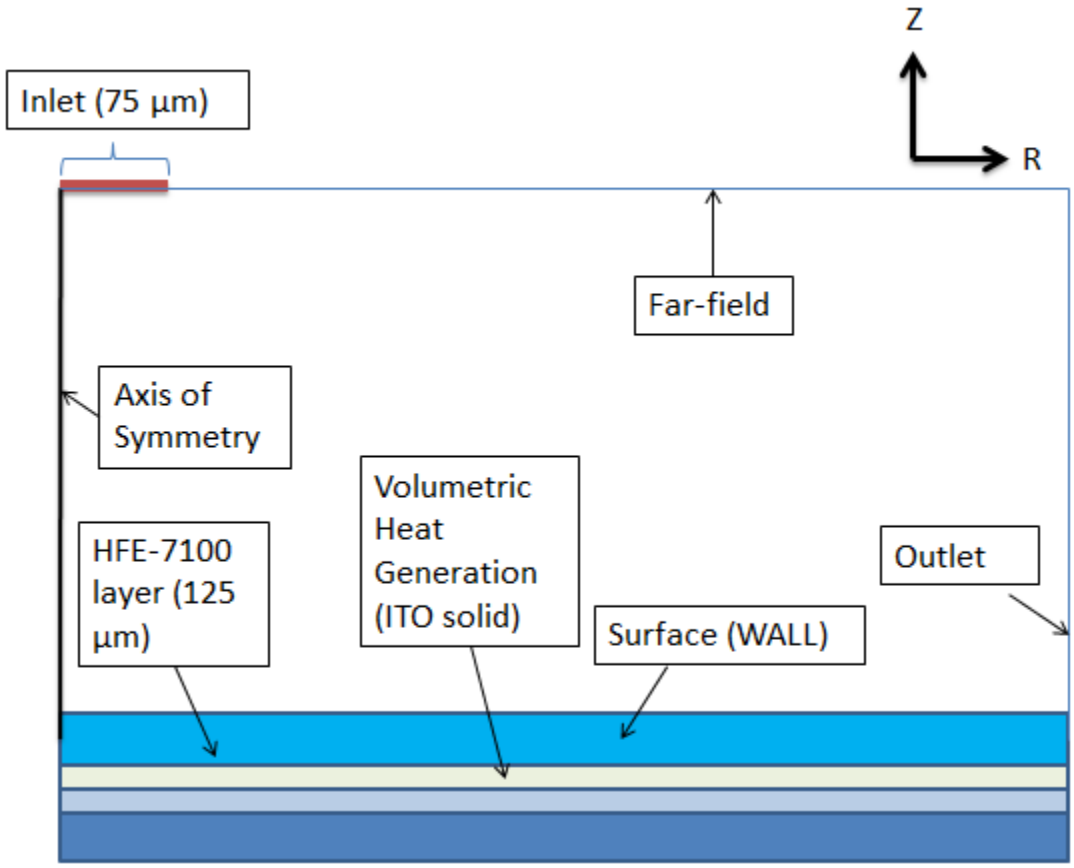


Figure 15. Fluid domain with common boundary conditions

Aforementioned boundary conditions were common to all simulations. However, both cooling techniques had their respective boundary conditions as well. In the jet impingement cases, a uniform velocity profile was applied to the boundary defined as inlet to generate a jet. This led to a simulated uniform circular jet with the same diameter as the orifice. Zhang [1] also stated that in his experimental setup that the jet diameter was same as the orifice diameter. Figure 16 shows the velocity profile across the inlet face of the fluid domain. A uniform velocity jet is generated as a result of this boundary condition.

Preliminary simulations were used to check the velocity profile of the jet just before impingement. Figure 16 shows the velocity profile of the jet at $z/r_j = 24$ or 0.2 mm from the bottom surface (or 1.8 mm from the top surface).. A similar fluid velocity profile was used by Lewis *et al.*[12] in his comparative study of surface cooling techniques.

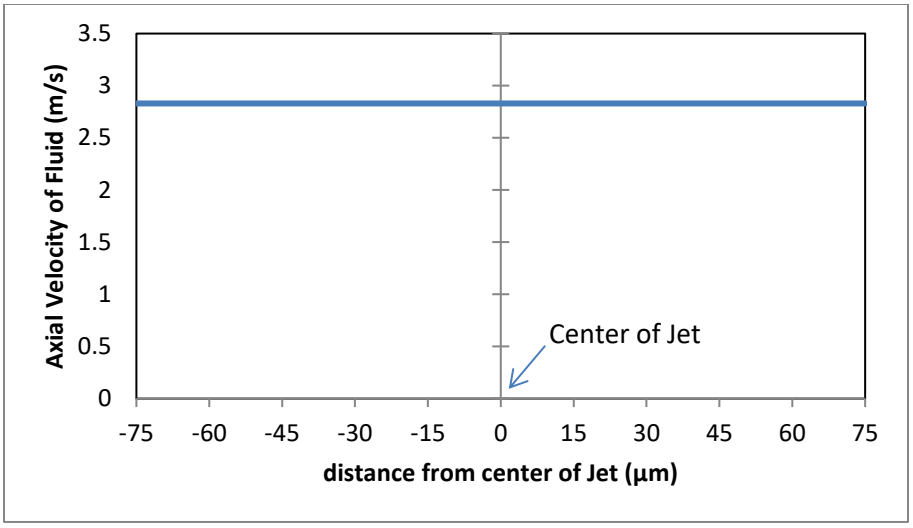


Figure 16. Uniform velocity profile for Case 1 (Jet impingement – 180 ml/hr.)

In droplet impingement, boundary conditions were applied to produce smooth and symmetrical droplets. There were two simulation parts including the pre-impingement droplet train and the post impingement flow. Experimentally, Zhang [1] used a function generator to create a microdispersed droplet train that did not separate or form secondary droplets before impingement. He adjusted the nozzle-to-surface distance and frequency of the generator to achieve this. For numerical simulations, creating a droplet train required careful application of boundary conditions to ensure accurate depiction of the experimentally generated droplets. Specifically, the following boundary conditions were set to ensure accurate depiction of the physical droplets:

1) Droplet temperature: 295 K

2) Droplet Velocity: 2.83 to 3.99 m/sec

Muthusamy [24] used a method called square wave velocity input at the inlet face. He reported that droplet formation required a larger domain, which further entailed breaking up of droplets and loss in shape. This method was somewhat based on the experimental technique of Zhang [1]. Since the emphasis of the study is one fluid-surface interactions taking place during the post impingement phase, a couple of continuously patched single droplets at fixed time intervals were used to account for a complete droplet train, with similar pre-impingement droplet properties. This idea was materialized by using a time dependent patching technique [42]. Patching of fluid in numerical simulations means a certain amount and shape of fluid can be placed at a certain location inside the domain. This technique involved patching of droplets with liquid fraction of 1 for HFE-7100 and a temperature of 295 K, after a fixed time interval. The time intervals were set to maintain droplet spacing and flow rate. Velocity of the droplet was also assigned, as required, in each case. A patched droplet is shown in Fig. 17. Three user defined commands were used as part of the technique to minimize computational cost.

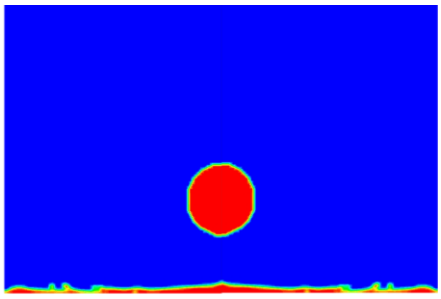

Figure 17: Volume fraction plot of droplet formed by time dependent patching scheme (HFE-7100 = Red, Air = Blue)

*3.2.4 Grid generation*

A crucial part of numerical simulation is to discretize the domain into finite control volumes, on which, finite volume difference equations are later solved. The step of breaking up the domain to run a CFD simulation is called grid generation, or meshing. Grid generation can affect the computational cost as well as the accuracy of the results. Therefore, it is vital to produce a grid that is able to capture all minor details and represent the entire physical phenomena of the fluid flow in question.

The physical domain for this simulation is 2 mm by 3 mm. A grid was generated inside the domain for that purpose. Grid type and grid spacing were the two primary parameters that were selected. Furthermore, Fig. 18 shows the key elements in a mesh, including the cell structure, cell center, cell face and grid spacing. As a common practice for 2D problems, either a structured (quadrilateral) or an unstructured (triangular) mesh is built. Structured mesh, as shown in Fig. 19, is easier to form and requires less number of cells to discretize the complete domain, which leads to reduced computational time. However, they cannot be formed in geometries with sharp acute or obtuse angles.

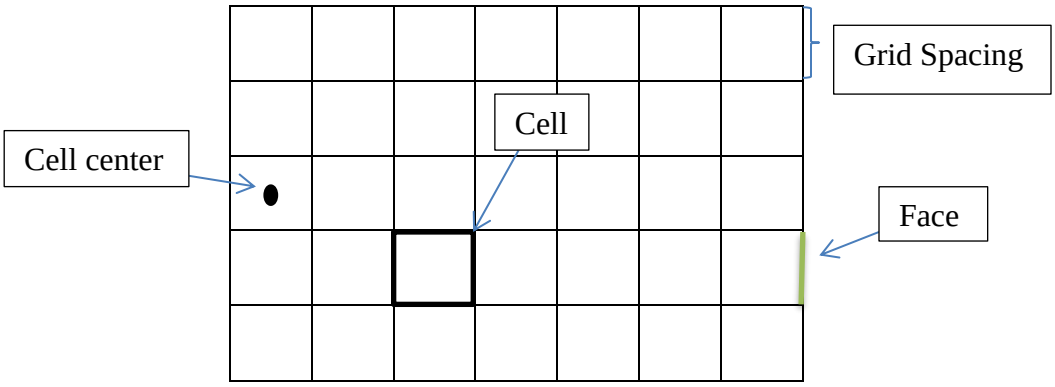


Figure 18. 2D Computational Domain

Since our domain was in the shape of a rectangle, a structured quadrilateral mesh was selected. The second primary parameter in grid generation was grid spacing. Grid spacing can reduce or increase the inaccuracy in the results. A benchmark was required to select an initial grid spacing size. Since one of the objectives of this study was to capture the liquid-air interface accurately, experimental value of film thickness was initially selected as a grid spacing size. Based on these two parameters, an initial mesh of 15000 cells was used, as shown in Fig. 20.

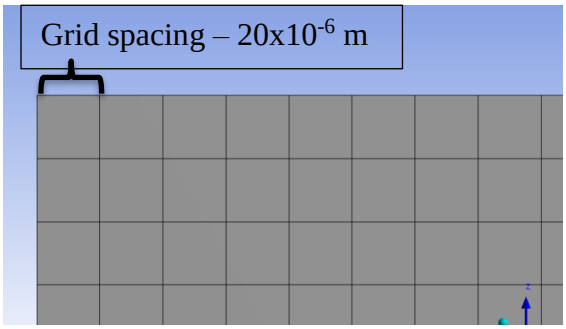


Figure 19. Structured grid for jet and droplet impingement with grid spacing of 20 µm

As a part of grid independence study detailed in the next chapter, grid was successively refined. Finally, a grid with structured mesh and a grid spacing of 2 µm was selected for jets and a grid spacing of less than 1 µm was selected for droplet trains. However, these meshes millions of elements, which increased the computational cost significantly. To reduce computational time while maintain accuracy of results, static mesh adaption technique was used for jet impingement as a method of refinement while for droplet cases, both static and dynamic mesh adaption techniques were used. Both of these techniques will be discussed in detail later [46].

*3.2.5 Governing equations and solution methods*

Next step in any CFD simulation was to select and apply the correct governing equations. These governing equations define the fluid flow principles. They are converted to finite volume equations, which are solved iteratively to obtain the desired results. Equation (7), (8) and (9) are the continuity equation, linear momentum (Navier-Stokes equation) and conservation of mass (energy) equation, respectively. These are the basic governing equations solved in any single or multiphase flow fluid and heat transfer problem [46].

$$\frac{\partial \rho}{\partial t} + \nabla.(\rho \vec{V}) = 0 \tag{7}$$

$$\rho\left[\frac{\partial \vec{V}}{\partial t} + (\vec{V}.\nabla)\vec{V}\right] = -\nabla \mathrm{p} + \nabla.\bar{\bar{\tau}} + \rho f \tag{8}$$

$$\rho\left[\frac{\partial h}{\partial t} + \nabla.(h\overrightarrow{V})\right] = -\frac{Dp}{Dt} + \nabla.(k\nabla T) + (\bar{\bar{\tau}}.\nabla)\vec{V} \tag{9}$$

For modeling the liquid-liquid multiphase flow, two approaches are available in the current CFD commercial codes. They are namely, the Euler-Euler approach and the Euler-Langragian approach. Eulerian-Langrangian approach involves the solution of Navier-Stokes equation for the continuum while each particle of the second phase is being tracked. It is generally used for dispersed flow (Small particles in a fluid inside a vortex separator) and is very numerically intensive. The Euler-Euler approach operates on the assumption that a volume occupied by one phase cannot be occupied by another. Therefore, a total volume fraction of one is considered throughout the domain[46] with each phase given its appropriate volume fraction. This concept is described as

interpenetrating continua [47]. The most common and widely used [13-30] multiphase model based on Euler-Euler approach is Volume of Fluid model. Several flow problems present in the literature [30-34] are solved using this model. VOF is especially computationally efficient as it solves one momentum equation for the whole domain. A volume fraction of each phase is calculated in each finite volume, and the volume fractions of all phases sum to unity. This calculation was also used to define an interface between the two phases throughout the domain. The continuity equation in the Fluent VOF model [47] for the $q^{th}$ is

$$\frac{1}{\rho_q}\left[\frac{\partial}{\partial t}(\alpha_q \rho_q) + \nabla.(\alpha_q \rho_q \overrightarrow{v})\right] = \frac{1}{\rho_q}\left[\sum_{p=1}^{n}(\dot{m}_{pq} - \dot{m}_{qp})\right] \tag{10}$$

where α is the volume fraction and ρ is the density of the phase.

The terms on the right hand side are for mass transfer between the phases, which is not considered in this problem. This equation is solved for only the primary phase, in this case, HFE. Volume fraction of air was calculated using the restriction, as follows:

$$\sum_{n}^{q=1} \alpha_q = 1 \tag{11}$$

Since each finite volume cell is divided based on volume fraction, the material properties are also calculated based on the volume fraction. A general equation for all properties based on volume fractions is as follows

$$R_q = \sum \alpha_q R_q \tag{12}$$

where R is the material property of the $q^{th}$ fluid

For calculating the velocity field, momentum (Navier-Stokes) equation is solved. In the VOF model, only one momentum equation is shared between the phases and the resulting velocity field is shared among the phases. The momentum equation (13), shown below, is dependent on the volume fractions of all phases through the properties ρ and μ.

$$\frac{\partial}{\partial t}(\rho\vec{v}) + \nabla.(\rho\vec{v}\vec{v}) = -\nabla \mathrm{p} + \nabla.[\mu(\nabla\vec{v} + \nabla\vec{v}^{T})] + \rho.\mathrm{g} + \vec{F} \qquad (13)$$

where F is the surface Tension force

Last of the basic governing equations is the energy equation (14) used for heat transfer calculations. The VOF model energy equation treats energy and temperature as mass-averaged entities. This equation, like the momentum equation, is shared between phases. The energy of each phase is defined by the specific heat capacity of that phase and the mass-averaged temperature. Properties including density and thermal conductivity are shared by the phases as well. A source term is also a part of this equation, which is also used for setting up the constant flux value. Energy equation for VOF is as follows:

$$\frac{\partial}{\partial t}(\rho E) + \nabla.\left(\vec{v}(\rho E + p)\right) = \nabla.\left(k_{eff}\nabla \mathrm{T}\right) + S_h \qquad (14)$$

This covers all the governing equations for multiphase flow VOF model. As mentioned previously, this model calculates phases within each cell and uses that to form an interface between two fluids. This kind of study warranted a good interfacing tracking method in order to correctly simulate a flow behavior, especially in the case of droplet impingement. VOF model's interface tracking is based on mass conservation [24], where in each cell the mass is conserved while the interface is advected. This is desirable property of this model, which leads to its common use. However, its interface resolution is not the

most accurate, as it uses linear slopes to calculate the interface between two fluids using the piecewise-linear algorithm (PLIC), developed by Youngs [48] A much more accurate method for interface construction with sharper resolution is the Level-Set (LS) Method, also available in Fluent. A sharper interface reconstruction leads to a more accurate surface tension calculation, which is of critical importance in microscale two-phase flows. LS method, however, has a major disadvantage of not conserving mass. Lorenzini [28] reported that LS method can lose up to 20% mass within a cell. To solve this problem, Sussman and Puckett [27] developed a combined method called CLSVOF method which has the desirable traits of each algorithm. In the CLSVOF model, the advection equation for the level-set function ϕ is incorporated (in addition to the volume fraction equation (1)) for the phase-tracking

$$\frac{\partial \emptyset}{\partial t} + \nabla.(v\emptyset) = 0 \qquad (15)$$

Where ∅ is the level set function and v is the characteristic velocity

This method addresses the mass loss problem of the LS algorithm and the sharper resolution problem of interface by using both LS and VOF values to building up interfaces. It used volume fractions values calculated using VOF approach and the gradient values from LS function to identify the direction of the interface. The PLIC algorithm is used for the interface reconstruction, and after this step is completed, all of the possible distances from a given point to the front-cut segments are minimized to reinitialize the LS function. A study [28] comparing VOF and CLSVOF technique showed that VOF technique lead to underpredicted temperature calculations as vapor-phase in a liquid-gas flow become more prominent.

Once the governing equations are finalized, CFD solution methods, models and solvers were selected in the commercial software. The geometry had solids and fluid zones. The fluid zones were solved with mixture as a fluid. Mixture means it can be either air or HFE-7100 or both. Table 7 details the solver method.

Table 7. Solvers and models used in the numerical study

| **Parameters** | **Definition** |
|---|---|
| Solver | 2D-Axisymmetric, pressure-based, transient, double precision |
| Viscous Model | Laminar |
| Energy Model | Turned On |
| Multiphase model | Volume of Fluid with CLS turned on (Solved with explicit scheme) |

Any CFD solution method that solves the finite volume equations iteratively can also impact the solution accuracy and convergence behavior. The CFD solution methods can have a direct effect on the pressure, velocity and temperature solutions. CFD commonly employs the pressure and velocity correction equations to solve for pressure and velocity fields using the SIMPLE Algorithm. A more refined scheme called Pressure-implicit with splitting of operators (PISO) is employed for multiphase flow with two additional correction equations called neighbor and skewness corrections. For solving convection diffusion equation, a quadratic upwind scheme is used. This scheme is called QUICK scheme. It uses a quadratic law between two upstream nodes and one downstream node for interpolating variables in the scheme. Table 8 details the solution methods employed in this study.

Table 8. Solutions methods employed for fluid dynamics and heat transfer

| **Parameters** | **Solution Method** |
|---|---|
| Pressure-Velocity Flow field | PISO |
| Pressure | PRESTO |
| Momentum | Second order Upwind, Quick |
| Volume Fraction | Geo-reconstruct |
| Transient Formulation | First Order Implicit<br>Time Step size (1e-6 to 1e-8) |
| Pressure - Under relaxation factor | 0.3 |
| Momentum - under relaxation factor | 0.7 |

*3.2.6 Solution process*

The solutions were obtained using a commercial CFD code, Fluent. Since the solutions were transient and computationally intensive, they had to be run on the high performance computational research (HPRC) super computer at Texas A&M University. Each of the cases simulated lasted a flow time of no more than 3 seconds with a time step size varying from 1 μs to 0.1 nanoseconds. Convergence criteria for pressure, velocity and LS function in each time step are given in Table 9.

Table 9. Convergence criteria for different parameters

| Parameter | convergence criteria |
|---|---|
| Velocity | 1.0E-04 |
| Pressure | 1.0E-04 |
| LS function | 1.0E-06 |

A relative convergence criterion was defined for the averaged temperature to determine convergence of the solution. It is defined as follows:

$$\frac{(T_{i-1} - T_i)}{T_{i-1}} < 1e-4 \tag{16}$$

i – timestep

T – Area Averaged Temperature

In all four cases, an exponential decay in temperature was observed over time as shown in the Results and Discussion Chapter of this thesis.

### *3.2.7 Post Processing*

Once results were obtained from numerical simulations, they were collected and compiled for post-processing. Post-processing involved analysis of the data by different tools including CFD-POST, Fluent post-processing and MS Excel. These included visualization of different parameters over spatial and temporal regimes, variation of different parameters over regions of importance and inference about flow and heat transfer from these results.

Post impingement behavior of jet and droplet train impingement was observed and understood by various physical parameters. Those parameters were averaged and used during the simulations to quantify the effects of impingement parameters on fluid hydrodynamics and heat transfer. Once the results converged, the parameters were extracted from the solution data. These include film thickness, temperature variation on the heater surface, and crater diameter. These were then compared with the experimental data to validate the numerical approach and results, as detailed in Chapter IV.

To better understand the heat transfer behavior and make strong inferences from the data, parameters representative of flow and heat transfer behavior such as boundary layer, thermal boundary layer, heat transfer coefficient and the Nusselt number were plotted as a function of radial distance along the heater surface.

The next chapter presented and discusses the simulation results for various cases.

# CHAPTER IV

# RESULTS AND DISCUSSION*

In this chapter, the simulation results for all the jet impingement and droplet train impingement cases are presented, and discussed based on the main objectives of the study. This chapter begins with a grid sensitivity study, which was conducted to ensure that the results were grid independent. Two grid refinement techniques were adopted in this study, namely static mesh adaption and dynamic mesh adaption, which are also discussed.

The grid independent results obtained from the simulations were compared with the experimental data available in the literature [1]. A comparison is necessary to ensure that simulated fluid flow accurately depicts fluid and heat transfer behavior seen in the experiments. This was achieved by comparing experimental and numerical heat transfer results of both cooling techniques, along the heated surface.

Lastly, a comparison of heat transfer behavior of jet impingement and droplet train impingement is presented. Superior performance of droplet impingement cooling over the jet impingement cooling is shown and analyzed.

---

"Reprinted from “Numerical and experimental investigations of crown propagation dynamics”, volume 57, by T. Zhang, J.P. Muthusamy, J. Alvarado, A. Kanjirakat and R. Sadr, 2016, Pages No., pg.24–33, Copyright 2015 with permission from Elsevier

## 4.1 Grid sensitivity and time dependence study

A common practice in CFD studies is to perform grid sensitivity or a grid independence study to ensure accurate results. To ensure optimal results, the solution should not vary due to changes in the density of the grid. By selecting and monitoring a value of interest in the solution after each grid refinement, the grid dependence of the results can be checked. When the monitored value stops varying, or varies within an acceptable range, the solution is considered to be grid independent.

### *4.1.1 Grid refinement*

As mentioned in the previous chapter, a structured grid was constructed in the fluid domain with an initial grid spacing of 20 µm. This initial grid was gradually refined as part of the grid independence study. Refinement of the structure mesh was done splitting cells into four equal parts, as shown in Fig. 20. To achieve this, the grid spacing was cut in half for each refinement.

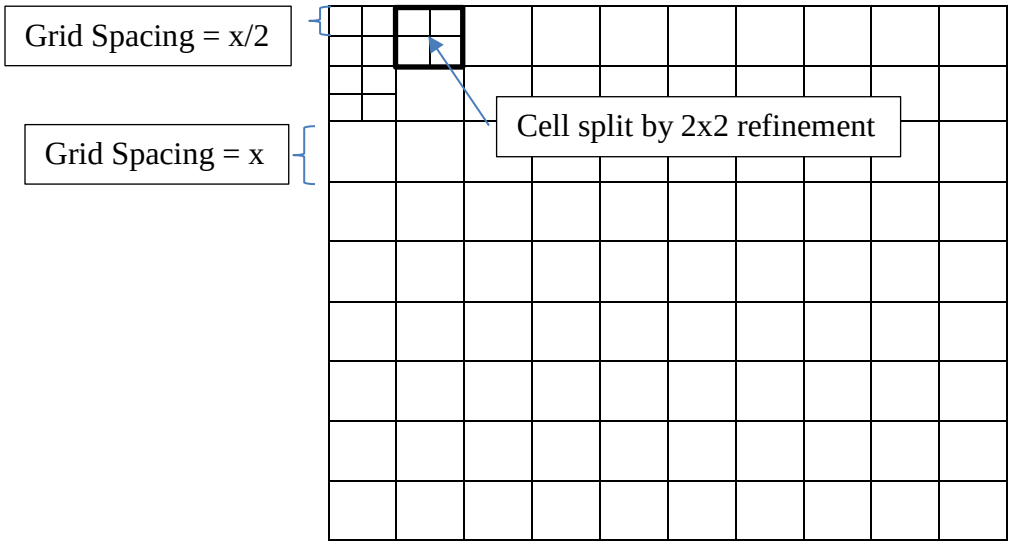


Figure 20. 2 by 2 refinement of structured mesh of the fluid domain

Grid refinement steps and the corresponding mesh sizes for the fluid domain are listed in Table 10. Grids with grid spacing as small as 1 μm, with a mesh element count of 5.9 million, were investigated as a part of the grid independence study. The grid refinement scheme was common to both cooling techniques since the same fluid domain was used for both simulations.

Table 10. Grid spacing and mesh element count for grid refinements

| **Grid spacing (μm)** | **Mesh Element count** |
|---|---|
| 20 | 1,500 |
| 10 | 6,000 |
| 8 | 93,750 |
| 4 | 371,250 |
| 2 | 1,490,000 |
| 1 | 5,896,448 |

*4.1.2 Grid independence for jet impingement cases*

For jet impingement cases, the value of interest for the grid independence study was the film thickness of the fluid flow within the crater. From the experimental data [1], film thickness value was available at a distance of 0.35 mm ($r/r_j = 4.67$) from the center of the jet. Therefore, film thickness value at this location was extracted from the CFD results for each grid refinement, in order to compare the value of interest with experimental data.

Fig. 21 shows the variation of film thickness value with grid spacing. From the grid refinement study, it was determined that a grid spacing of 4 µm (mesh element count = 371,250) was sufficient. A 371250 element mesh element count was computationally expensive and simulations were time consuming. Therefore, an approach was sought to reduce the mesh element count while maintaining accuracy as describe below.

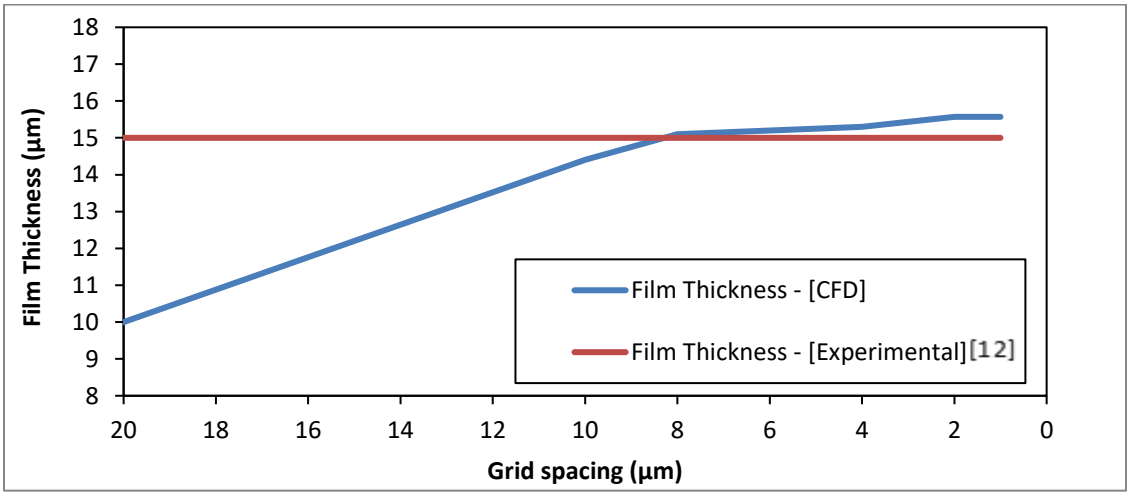


Figure 21. Grid independence study for jet impingement grid with film thickness as value of interest

4.1.2.1 Static mesh adaption

Static mesh adaption is a local mesh refinement technique commonly used in CFD studies. Using this technique, the mesh can be refined in regions where accurate solution is sought while the remainder of the mesh can be kept relatively coarse. Fig. 22 shows an example of static mesh adaption. A 2D mesh is refined in regions upstream and downstream of the cylinder to capture crucial regions of the flow accurately.

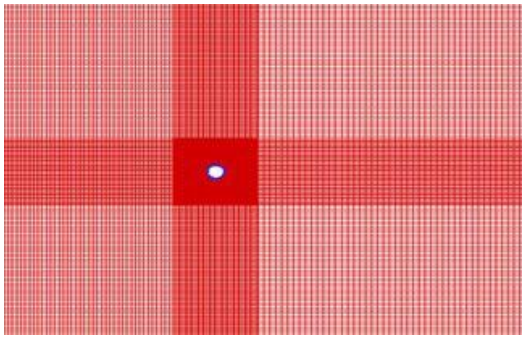

Figure 22. An example of static mesh adaption and refinement in regions of interest

For jet impingement cases, the hydrodynamics and heat transfer behavior from the stagnation point to the crater was crucial. Therefore, cells in these locations were refined by using a refinement region. For estimating this region, film thickness measurement of Zhang [1] was considered as a benchmark. Zhang [1] measured a film thickness value of 15 μm for both jet impingement cases. A region of 8 times larger than the film thickness was marked as a refinement region. Fig. 23 shows the mesh with the refinement region of 120 μm. Notice the grid spacing value of 2 μm was selected in the refinement region. This was done to better capture the hydrodynamic of jet impingement and thermal boundary layer profiles, as shown later.

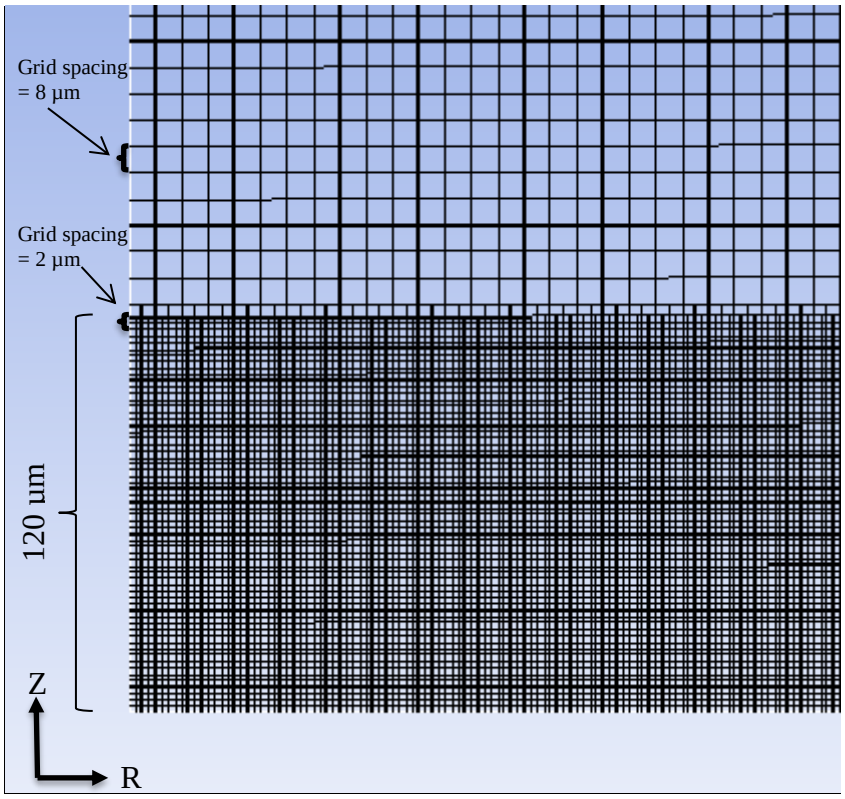


Figure 23. Static mesh refinement region for jet impingement grid

The mesh element count of the grid after static mesh adaption was 109,000. A grid formed with a grid spacing of 2 µm, without static mesh adaption, had 1.49 million elements. The film thickness value was same for both grids. Using static mesh adaption, the element count of the grid was brought down by 15 times, while maintain the accuracy of the results. A grid with static mesh adaption was used for both jet impingement cases.

*4.1.3 Grid independence for droplet train impingement cases*

Droplet train impingement hydrodynamics were different from jet impingement due to the periodic nature of flow. While jet impingement flow reached hydrodynamics stability after a while, droplet impingement flow varied each time a droplet impinged. Therefore, film thickness was not used for grid independence. Muthusamy [24] used the crown rim diameter for grid independence and compared the values with experimental results of Zhang [1]. Muthusamy [24] reduced the grid size element from 20 μm to 1 μm to find the optimum mesh resolution. Fig. 24 shows the grid independence trend for droplet impingement cases conducted by Muthusamy [24].

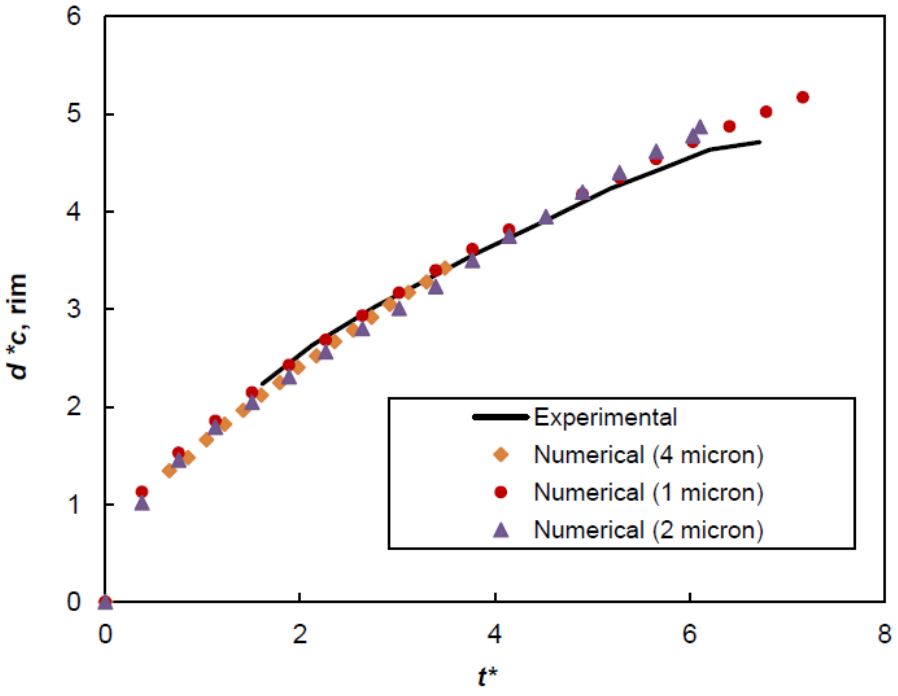


Figure 24: Crown rim diameter as a function of grid or element size for droplet jet impingement [24]

Muthusamy [24] used the static mesh adaption to refine the grid in different regions during the droplet impingement simulations. He divided the grid into different

zones and set up different grid spacing values in each of them. This led to the total grid size of 400,000 elements. In this study, a similar refinement scheme was used for the two droplet cases considered in the study. Fig. 25 shows the grid refinement scheme by Muthusamy [24].

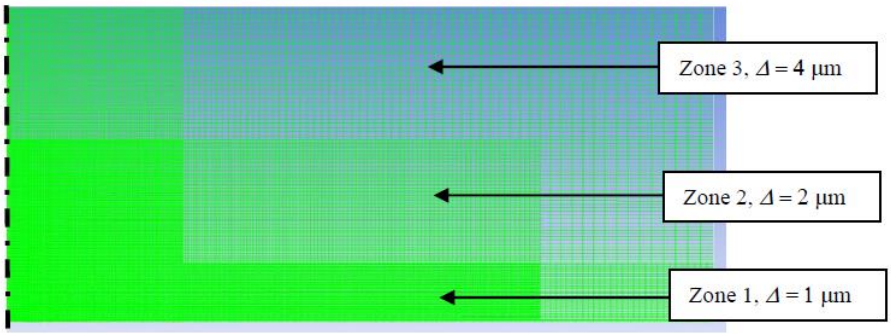


Figure 25: Grid Refinement scheme used by Muthusamy [24]

*4.1.4 Time sensitivity study and CFL number*

Jet impingement and droplet impingent simulations were transient solutions and were set up within a domain of 6 $mm^2$. The nozzle-to-surface distance for both cooling techniques was 2 mm. Therefore, to accurately capture fluid behavior and ensure that vital fluid movement was captured by the simulations, a correct time-step size was selected. For this purpose, a dimensionless constant called Courant–Friedrichs–Lewy (CFL) number was utilized. Equation (17) shows the CFL number.

$$CFL = \frac{u\Delta t}{\Delta x} \tag{17}$$

Where,
$u$ is the maximum flow velocity,
$\Delta t$ is the time step size
$\Delta x$ is the grid spacing

To ensure convergence of the numerical simulations, the Courant number should be less than 1. For this purpose, an initial time step size of 0.1 nanoseconds was used to run simulations and corresponding CFL numbers were checked. Based on these initial CFL values, a range of time step values from 1 μs to 0.1 nanoseconds were identified as sufficient to keep the CFL number below 1. The software, Fluent provides an option to set up adaptive time stepping scheme while keeping the CFL number less than 1. It requires a range of time step values to keep CFL number less than 1. The time step values identified earlier were used as input for the adaptive time stepping scheme.

## 4.2 Numerical results and validation using experimental data

CFD simulations are perform to solve all the sets of governing equations taking into account heat transfer and fluid flow. Therefore, the results obtained from these simulations require validation using experimental data. In this study, experimental results obtained from Zhang [1] were available for validation for jet impingement and droplet train impingement. For this purpose, experimental and numerical values of averaged temperature profiles, Nusselt number and heat transfer coefficients for both cooling techniqus were compared.

For a measure of the temperature value of the heated surface, an area averaged temperature was used. The experimental results were averaged over a square of 2.5 mm by 2.5 mm. Since the fluid domain in the CFD set up was axisymmetric, the heater model had a circular surface. For comparison of temperature, temperatures values from the CFD were averaged over an equivalent circular area. Using the area of the square (2.5 mm x 2.5 mm) and equating it with $\pi r^2$, the radius of the averaging area was found out to be 1.41 mm. All the CFD results shown below have temperatures averaged over a circle with a radius 1.41 mm.

### *4.2.1 Jet impingement*

Two jet impingement cases were investigated and their results were compared with experimental results. Heat flux was kept constant for both cases. The details are given in the Table 11.

Table 11. Parameters of the jet impingement cases

| *Case number* | *Q (mL/h)* | *dj (µm)* | *Vj (m/s)* | *Heat Flux (W/cm$^2$)* |
|---|---|---|---|---|
| 1 | 180 | 150 | 2.83 | 3.6 |
| 2 | 210 | 150 | 3.30 | 3.6 |

Both of these cases were simulated until the relative convergence criterion, defined in the previous chapter, reached a value of 1e-4. For both cases, once this value was reached, the simulation was considered as converged and the results were compared with experimental values. Fig. 26 shows the behavior of the convergence criterion as the simulation of Case 1 progressed. As the figure shows, the simulation converged after 2.6 seconds of simulation time.

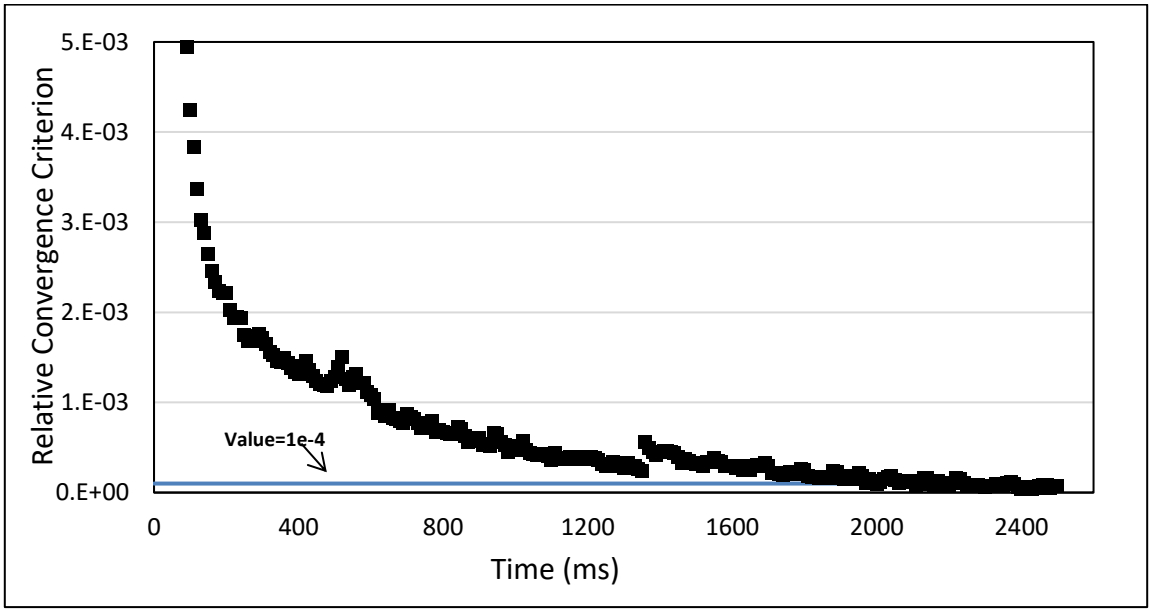


Figure 26. Relative Convergence Criterion of Temperature vs Simulation Time for Jet Impingement Case 1 - 180 ml/hr. - 3.6 W/cm$^2$

For both jet impingement cases, a final value for the area averaged temperature was available from the experimental results [1]. The averaged temperature values in each simulation were monitored throughout. Fig. 27 shows the variation of area averaged temperature with flow time. As the simulation converged, the gap between experimental and numerical temperature values was reduced. In both jet impingement cases, numerical results were able to attain temperature values within 0.2 K of the experimental values.

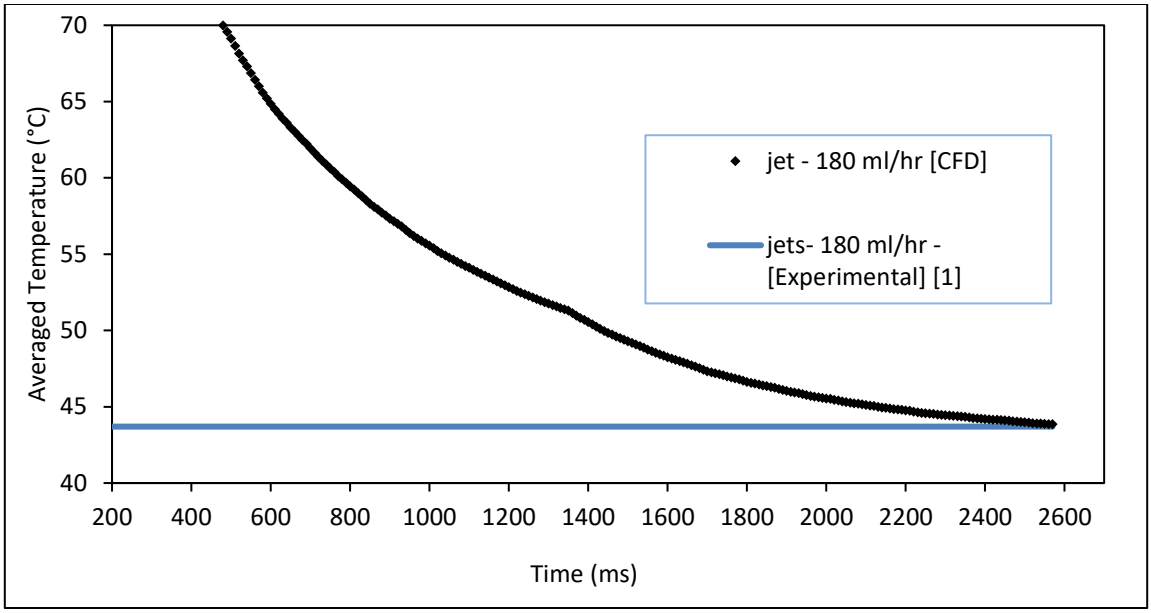


Figure 27. Averaged Temperature on the heated surface vs Flow Time for Jet Impingement Case 1 - 180 ml./hr. - 3.6 W/cm$^2$

It was vital to study the variation of temperature across the heated surface to understand how the impingement produced a cooling effect on the surface. The variation of temperature values across the heater surface was also available in the experimental data. Comparison of experimental and numerical values for each jet impingement cases is shown in Fig. 28 and Fig. 29, respectively. Numerical results agreed well with the experimental results. Averaged temperature values were found within 5% of the experimental data for both cases. CFD results were marginally over predicting the cooling effect of the circular jet with lower surface temperature values across the surface. It was also observed that jets with higher flow rate cooled the surface better

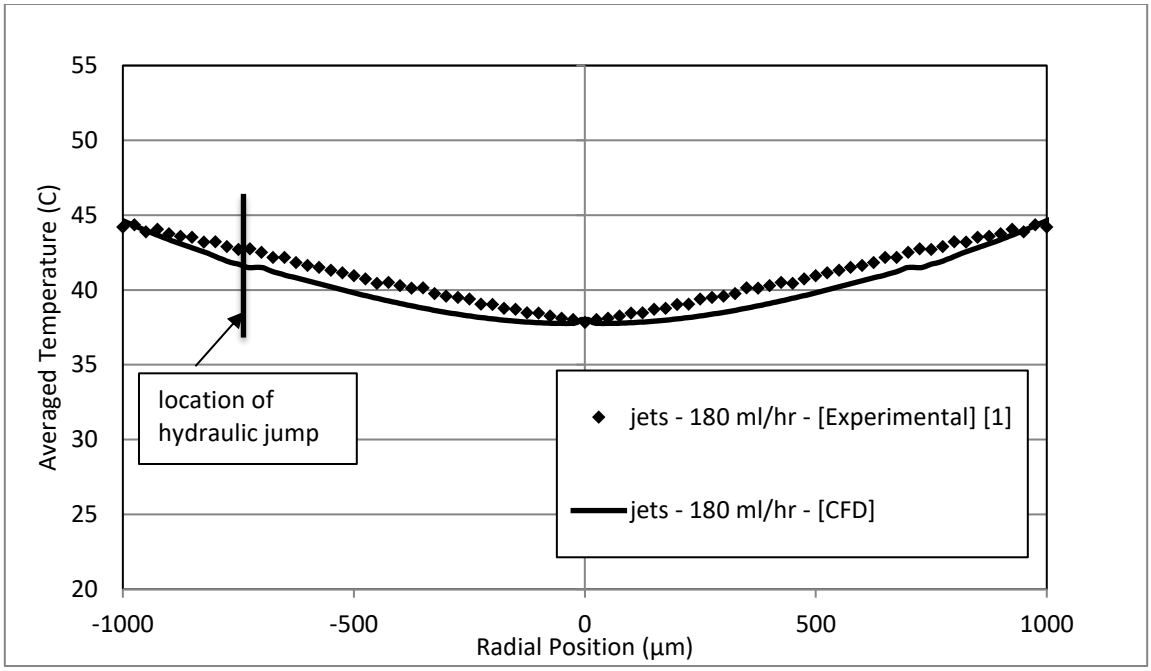


Figure 28. Temperature versus radial position comparison between Zhang [1] and CFD simulations - jet impingement case 1 (180 ml/hr. – 3.6 W/cm$^2$)

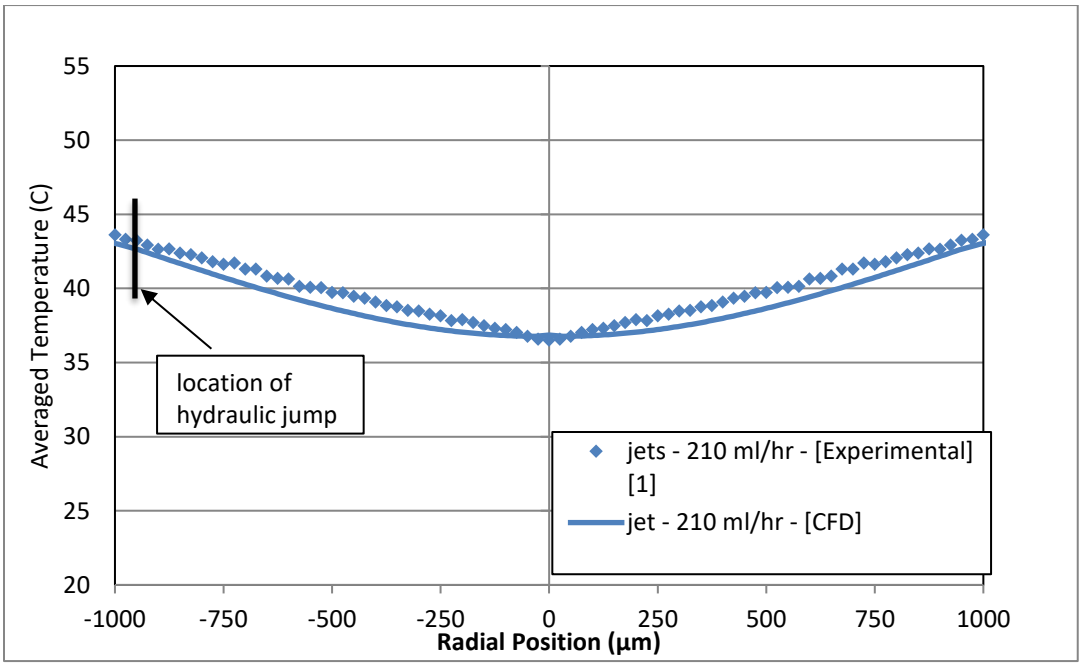


Figure 29. Temperature versus radial position comparison between Zhang [1] and CFD simulations - jet impingement case 2 (210 ml/hr. – 3.6 W/cm$^2$)

To understand the enhancement of heat transfer behavior due to convection, the Nusselt number was calculated from temperature values from CFD using equation (18), as follows:

$$Nu_{dorf}\,(r) = \frac{q^{"}}{T(r) - T_0}\,\frac{d_{orf}}{k_l} \tag{18}$$

*Where*
$q^{"}$ – Heat Flux
$T(r)$ - Temperature at the radial position
$T_0$ – Initial Temperature of the fluid
$k_l$ – Thermal conductivity of the fluid
$d_{orf}$ – Diameter of the Orifice

These values were then compared with the experimental results [1] for both jet impingement cases. Fig. 30 and 31 show the Nusselt number variation for each jet impingement case from the center of the jet. As expected, Case 2 has higher Nusselt number values due to lower temperature values across the surface, as shown in Fig. 29. Nusselt numbers from CFD are slightly higher than experimental values in both cases due to the lower temperatures predicted by CFD.

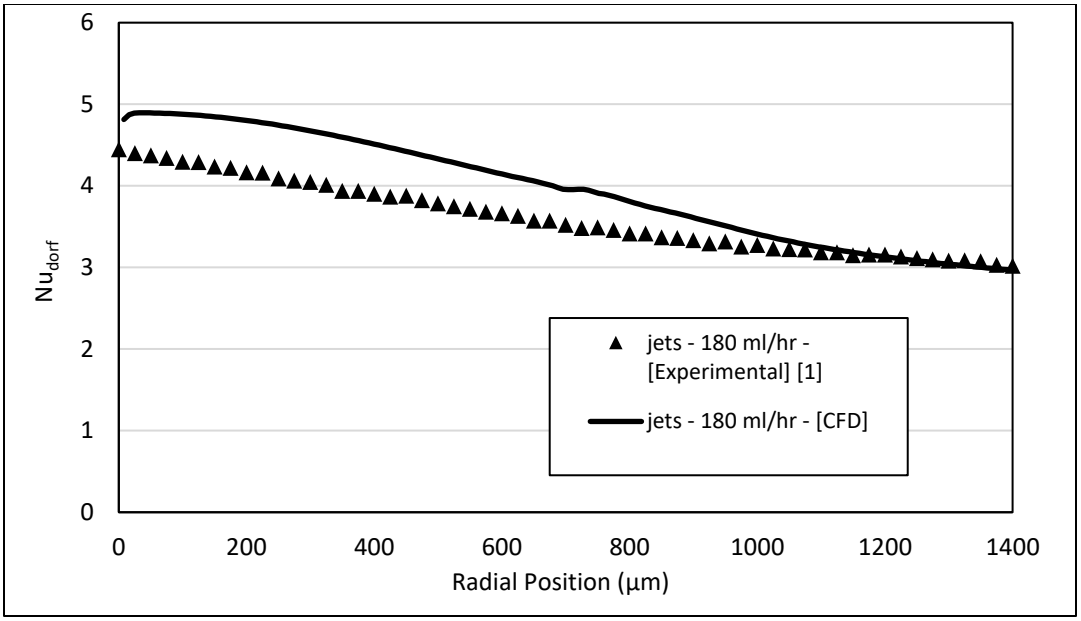


Figure 30.Nusselt number versus radial position comparison of Zhang [1] and numerical results from CFD simulations for jet impingement case 1 (180 ml/hr. – 3.6 W/cm$^2$)

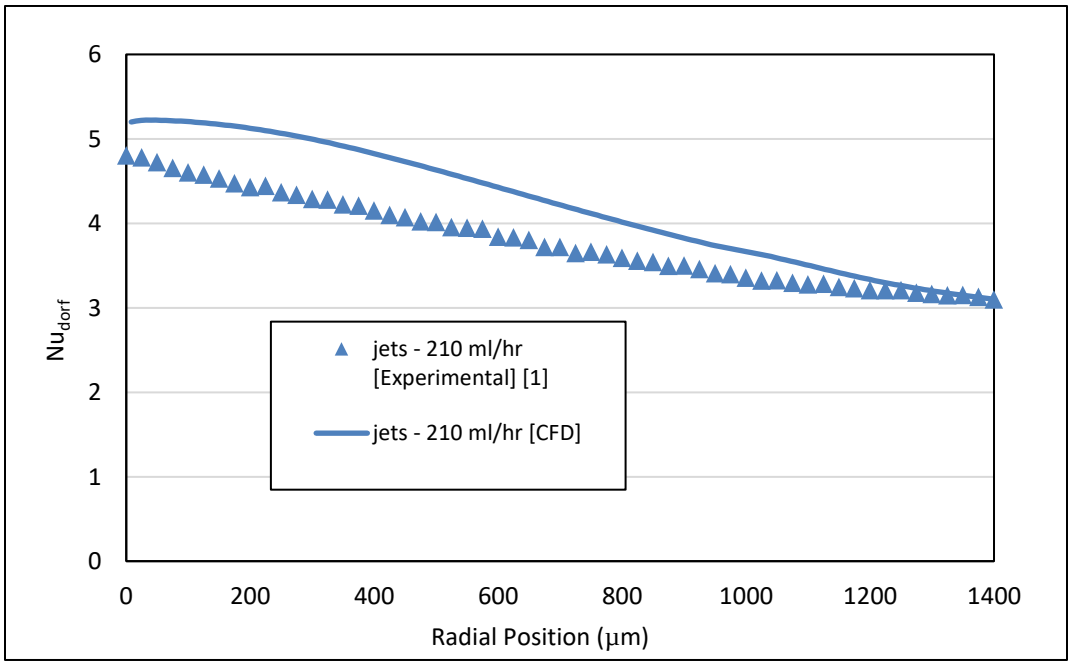


Figure 31. Nusselt number versus radial position comparison of Zhang [1] and numerical results from CFD simulations for jet impingement case 2 (210 ml/hr. – 3.6 W/cm$^2$)

The most important indicator of convective heat transfer performance is the heat transfer coefficient. Using the Nusselt number profiles available from CFD, heat transfer coefficients were calculated along the heated surface. Fig 32 and 33 show the heat transfer profiles of both cases. The highest heat transfer coefficient values occurs close to the stagnation point due to impingement. As the fluid spreads, heat transfer coefficient values decrease as the velocity of the fluid decreases. Due to higher flow rate, Case 2 produces higher heat transfer coefficient values.

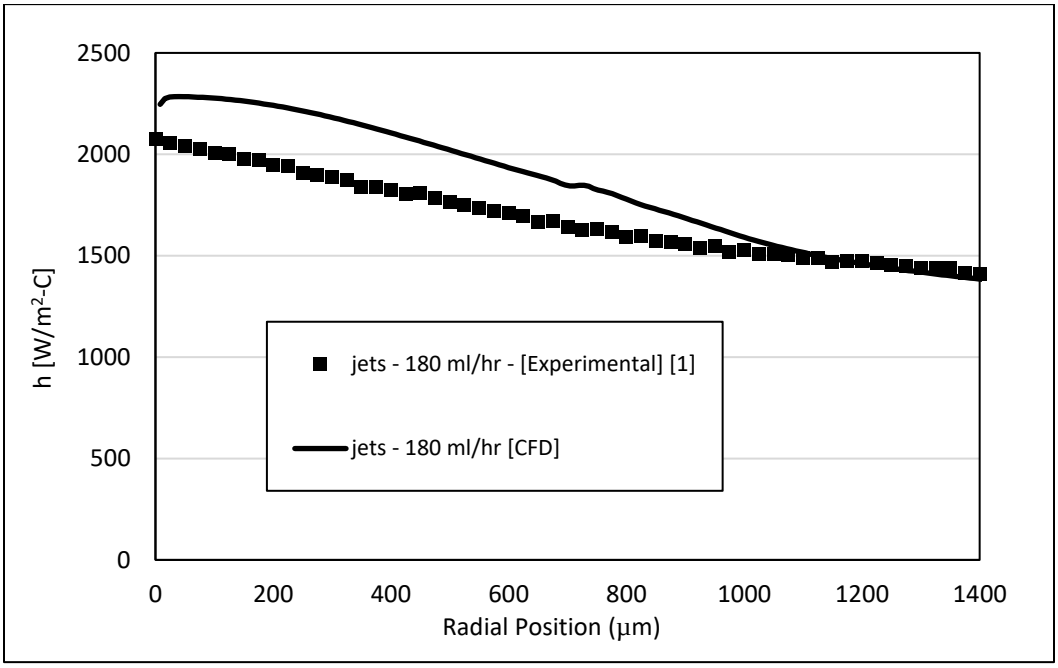


Figure 32. Comparison of Zhang [1] and CFD for Heat transfer coefficient variation along the heated surface for jet impingement case 1 (180 ml/hr. – 3.6 W/cm$^2$)

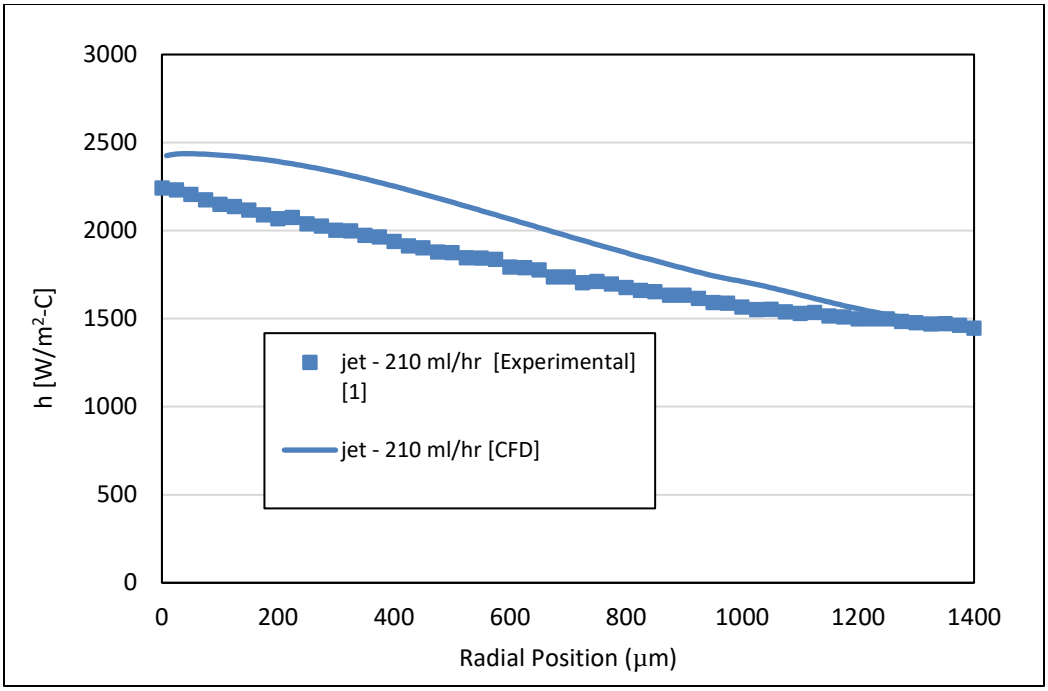


Figure 33. Comparison of Zhang [1] and CFD for Heat transfer coefficient variation along the heated surface for jet impingement case 2 (210 ml/hr. – 3.6 W/cm$^2$)

*4.2.2 Droplet train impingement*

Two cases of droplet impingement cooling, with similar parameters as jet impingement, were investigated in this study. For droplets, the diameter of orifice was different from the diameter of droplet. The details of these cases are shown in Table 12.

Table 12. Parameters of droplet impingement cases

| *Case number* | *Q* (mL/h) | $d_d$ (µm) | $V_d$ (m/s) | *Heat Flux* ($W/cm^2$) | *Weber Number* |
|---|---|---|---|---|---|
| 3 | 180 | 237 | 3.52 | 3.6 | 328 |
| 4 | 210 | 249 | 3.99 | 3.6 | 443 |

Similar to jet impingement cases, the relative convergence criterion was used to determine convergence. The simulation was considered as converged once the criterion reached the value of 1e-4. The variation of the convergence criterion with flow time for Case 4 (210 ml/hr. – 3.6 $W/cm^2$ – We=443) is shown in Fig. 34.

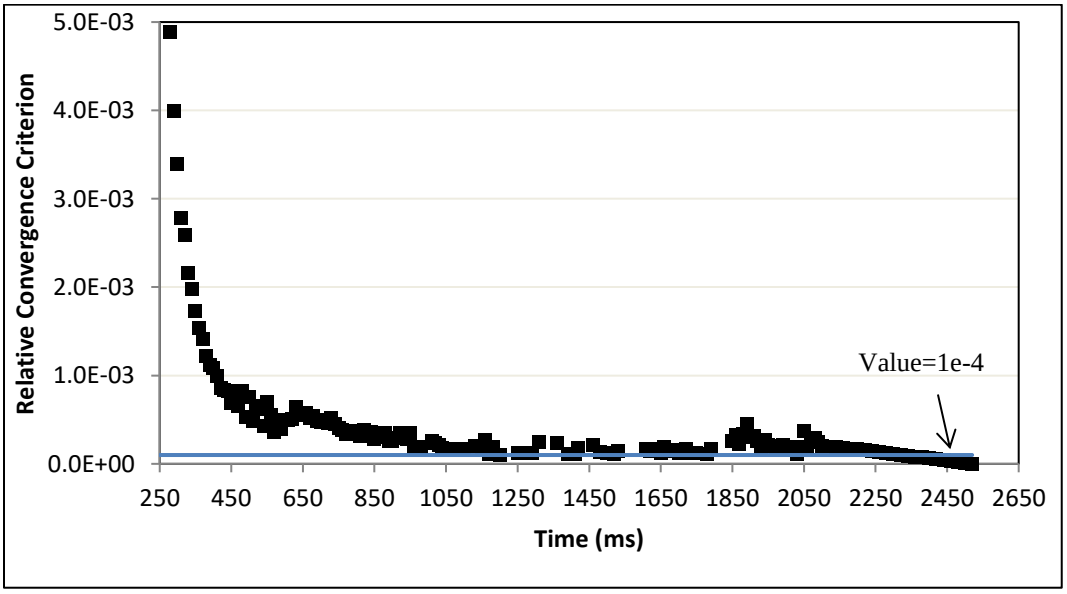


Figure 34. Convergence Criteria and Relative Convergence Value of Temperature vs Simulation Time for Droplet Impingement Case 4 - 210 ml./hr. - 3.6 $W/cm^2$ - We=443

Fig. 35 shows the variation of area averaged temperature with flow time for case 4. A similar behavior to jet impingement simulation was observed as the gap between experimental and numerical temperature values reduced with flow time. Despite the periodic nature of this cooling technique, a smooth cooling trend is observed over time. In both droplet impingement cases, numerical results were able to attain temperature values within 0.2 C of the experimental values.

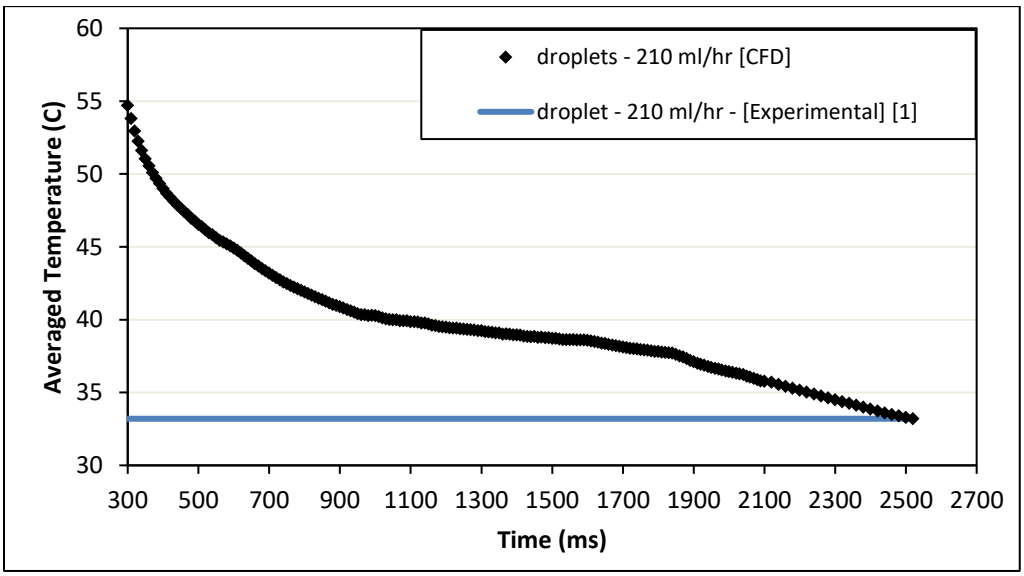


Figure 35. Averaged Temperature on the heated surface vs Flow Time for Droplet Impingement Case 4 - 210 ml./hr. - 3.6 W/cm$^2$ - We=443

Fig. 36 and Fig. 37 show the temperature profile across the heat surface for case 3 and case 4, respectively. Numerical results agreed well with the experimental results for droplet impingement cases. Averaged temperature values were found within 8% of the experimental data for both cases. All the CFD generated profiles were relatively smooth due to the high number of cells points and better time averaging of the data. A marginal over prediction of temperature near the center of the droplet impingement region is

observed in the CFD results. CFD and experimental values are almost similar as the flow spread radially. A change in temperature profile due to hydraulic jump was not as evident in droplets compared to jumps. Compared to case 3 (180 ml/hr.), case 4 (210 ml/hr.) had lower temperature at the center of impingement due to higher velocity of the droplets.

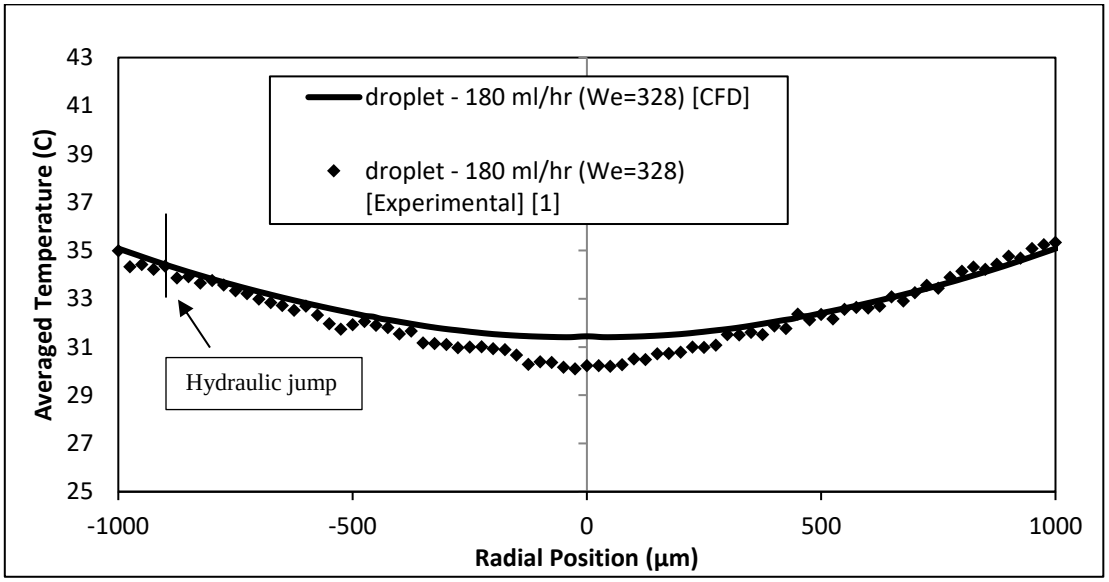


Figure 36. Temperature versus radial position comparison between Zhang [1] and CFD simulations - droplet impingement case 3 (180 ml/hr. – 3.6 W/cm$^2$ – We=328)

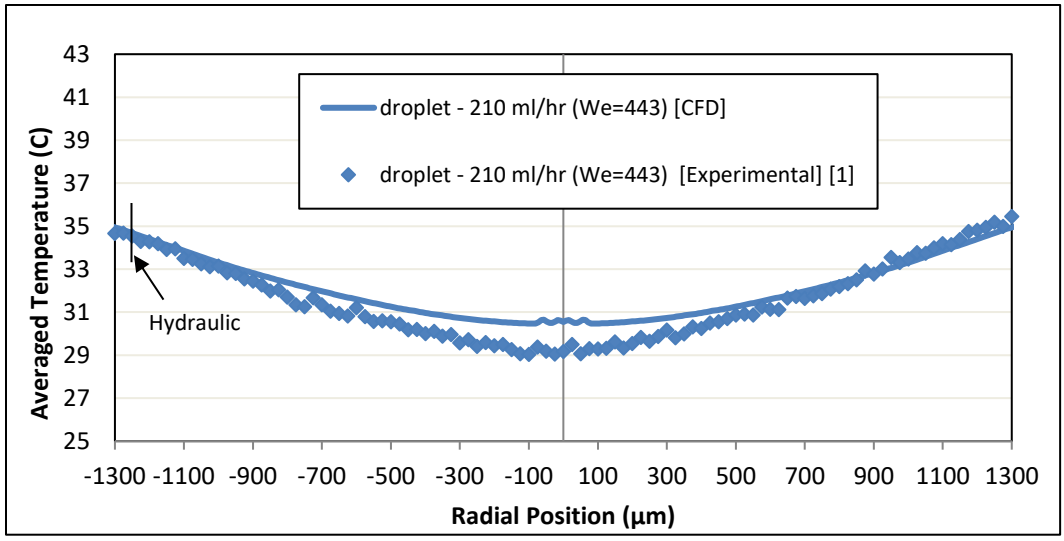


Figure 37. Temperature versus radial position comparison between Zhang [1] and CFD simulations - droplet impingement case 4 (210 ml/hr. – 3.6 W/cm$^2$ – We=443)

Nusselt numbers were calculated and plotted for droplet impingement cases using Equation (18). Fig. 38 and 39 show the Nusselt number variation for each droplet impingement case from the center of the impingement zone, up to radial position of 1400 μm. As expected, Case 4 has higher Nusselt number values compared to Case 3, due to higher flow rate and momentum. Nusselt number profiles marginally underpredicted the Nusselt number near the impingement zone for both cases. This is relatable to Fig. 36 and Fig 37, which show an over prediction of temperature values in this region.

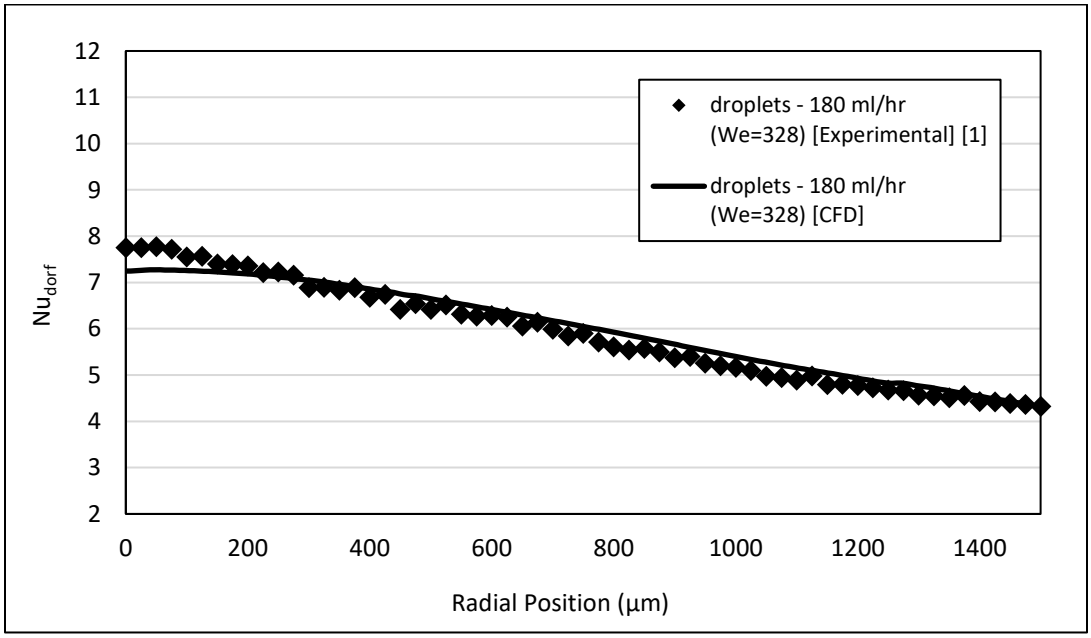


Figure 38. Nusselt number versus radial position comparison of Zhang [1] and numerical results from CFD simulations - droplet impingement case 3 (180 ml/hr. – 3.6 W/cm$^2$ – We=328)

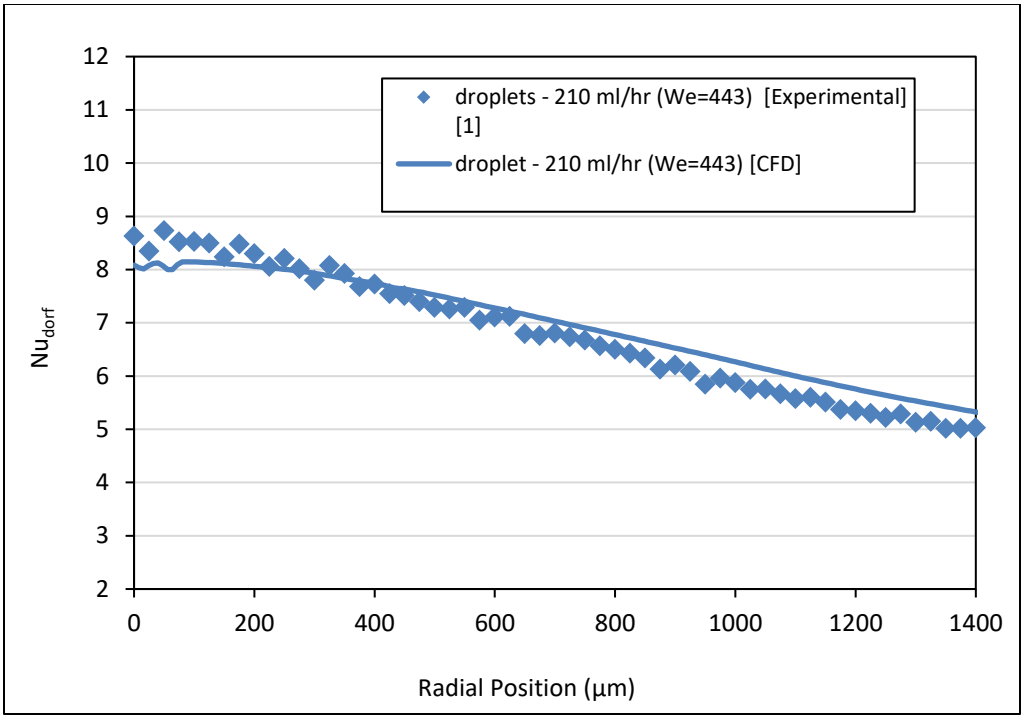


Figure 39. Nusselt number versus radial position comparison of Zhang [1] and numerical results from CFD simulations - droplet impingement case 4 (210 ml/hr. – 3.6 W/cm$^2$ – We=443)

Heat Transfer coefficient was also plotted for droplet impingement cases using the Nusselt number results. Fig 40 and 41 show the heat transfer coefficient profiles for both cases. The highest heat transfer occurs close to the stagnation point due to impingement, as in jet impingement cases. As the fluid spreads, heat transfer coefficient values decrease as the velocity of the fluid decreases. Overall, a good agreement was found between experimental and numerical values. Heat transfer coefficients values for case 4 (210 ml/hr.) were 10% higher than case 3 (180 ml/hr.), indicating better heat transfer from higher flow rate.

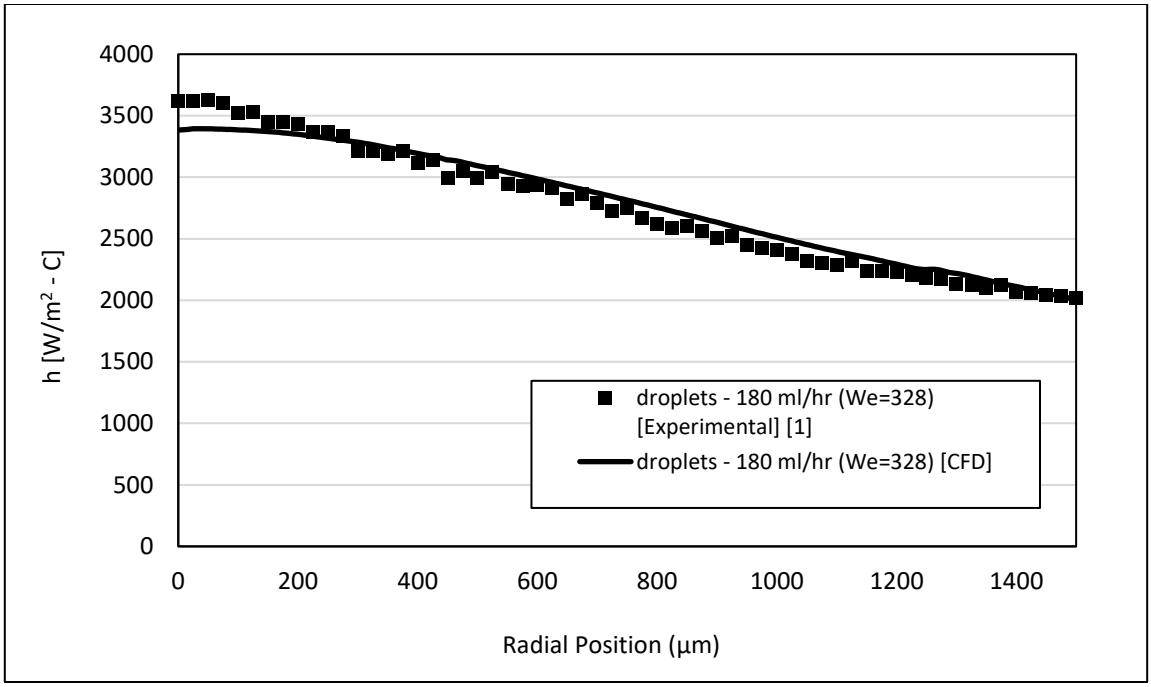


Figure 40. Comparison of Zhang [1] and CFD for Heat transfer coefficient variation along the heated surface for droplet impingement case 3 (180 ml/hr. – 3.6 W/cm$^2$ – We=328)

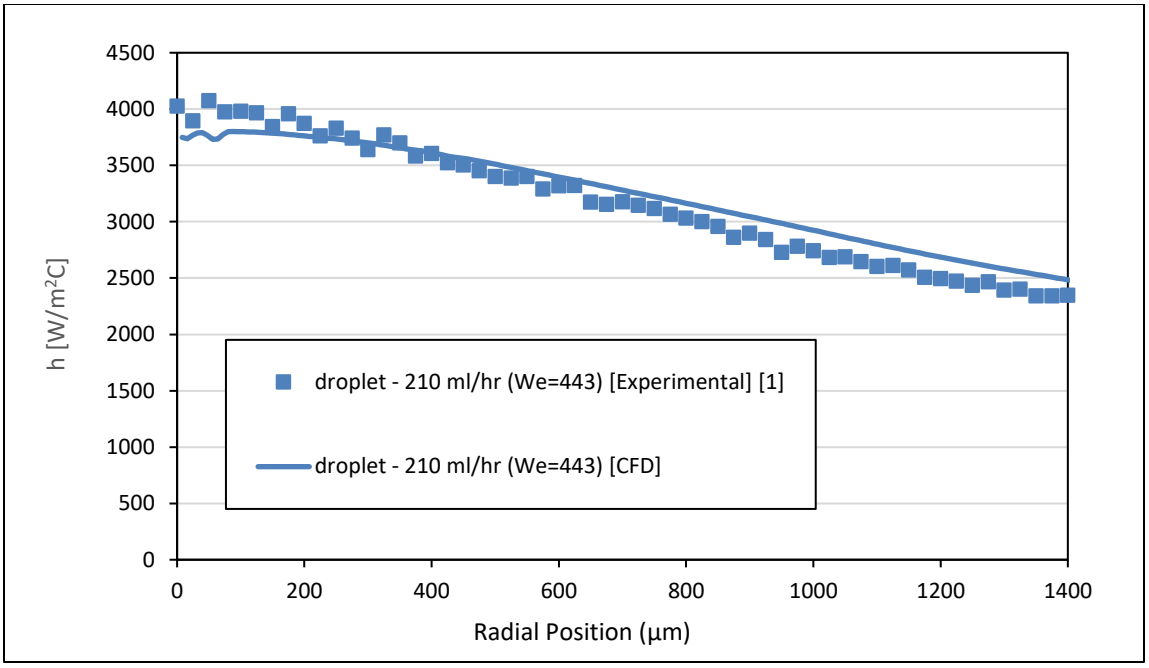


Figure 41. Comparison of Zhang [1] and CFD for Heat transfer coefficient variation along the heated surface fore for droplet impingement case 4 (210 ml/hr. – 3.6 W/cm$^2$ – We=443)

The numerical results obtained from a CFD solution were compared with experimental data and good agreement was found between the two data sets. Therefore, the CFD simulation results were validated and they were used for comparing the droplet and jet impingement cooling techniques as shown and described in the next section.

## 4.3 Comparison of Jet Impingement and Droplet Train impingement cooling

A detailed comparison between the jet impingement and droplet train cooling was performed. The parameters selected for the study were similar for both cooling techniques. These parameters were the volume flow rate, heat flux and the orifice diameter. Therefore, the results were comparable and were used to draw inferences about heat transfer performance. The details of these comparisons are shown in Table 13 and Table 14. Hydrodynamics and heat transfer behavior of both cooling techniques are compared in the following sections.

Table 13. Jet impingement vs droplet impingement parameters for 180 ml/hr.

| **Comparison A – 180 ml/hr. - 3.6 W/cm$^2$** | | |
|---|---|---|
| *Parameter* | *Case 1–Jet Impingement* | *Case 3–Droplet Impingement* |
| Heat Flux (W/cm$^2$) | 3.6 | 3.6 |
| Flow Rate (mL/hr.) | 180 | 180 |
| Impingement velocity (m/s) | 2.83 | 3.52 |
| Weber number | N/A | 328 |
| Frequency (Hz) | N/A | 6300 |
| Orifice Diameter (µm) | 150 | 150 |
| Fluid Diameter (µm) | 150 | 237 |

Table 14. Jet impingement vs droplet impingement parameters for 210 ml/hr.

| **Comparison B – 210 ml/hr. - 3.6 W/cm$^2$** | | |
|---|---|---|
| *Parameter* | *Case 2–Jet Impingement* | *Case 4–Droplet Impingement* |
| Heat Flux (W/cm$^2$) | 3.6 | 3.6 |
| Flow Rate (mL/hr.) | 210 | 210 |
| Impingement velocity (m/s) | 3.3 | 3.99 |
| Weber number | N/A | 443 |
| Frequency (Hz) | N/A | 6500 |
| Orifice Diameter (µm) | 150 | 150 |
| Fluid Diameter (µm) | 150 | 249 |

*4.3.1 Comparison of hydrodynamics*

In order to understand the behavior of convective heat transfer, it was necessary to compare and understand the hydrodynamics of both cooling techniques. Hydrodynamics features such as film thickness, different components of film velocity and the momentum of the fluid after impingement is compared for both cooling techniques using CFD results.

4.3.1.1 Film thickness

One of the most important parameter to check and compare for both cooling techniques was the film thickness. The layer of fluid that forms within the crater was carefully studied since most of the heat transfer occurred in this region. Film thickness values were calculated at the HFE-air interface from the Volume Fraction contours at radial position of 0.35 mm, as shown in Fig. 42. This location was selected to ensure comparability with experimental data. Both jet impingement cases had film thickness values close to each other since the difference between the flow rates was not large. Experimental values for film thickness were also available from Zhang [1]. CFD values were within 3% of the experimental data.

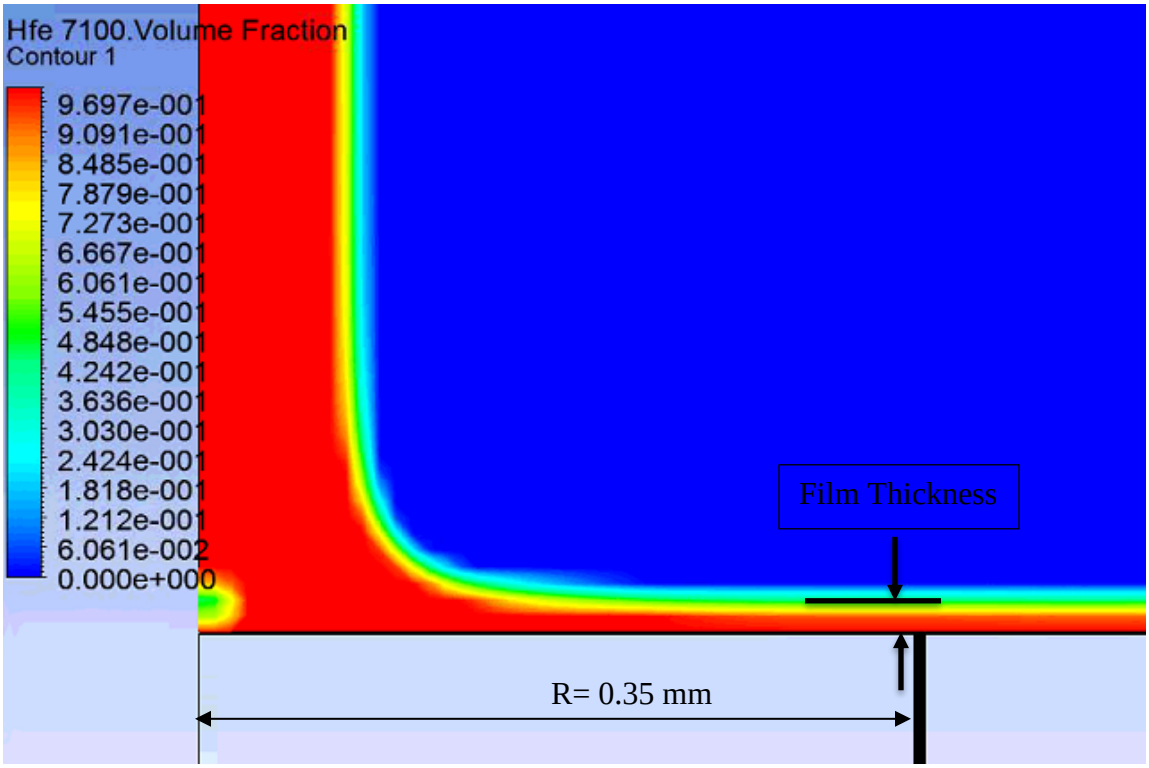


Figure 42. Volume Fraction contour from CFD used to calculated film thickness for jet impingement cases

Droplet impingement hydrodynamics was not steady and varied periodically due to droplet impingement at a certain frequency. Therefore, a steady film thickness was not observed. A volume fraction tracker was used to measure the film thickness value at radial position of 0.35 mm as the simulation progressed. The film thickness varied between 10 µm and 60 µm for both droplet impingement cases. The overall averaged film thickness of droplet impingement cases was found to be 3 times greater than in the jet impingement cases.

4.3.1.2 Crater diameter

Crater diameter provides an important location in both cooling techniques. It was found that by locating the point in the fluid where a sudden jump in fluid height is observed. This point is called hydraulic jump. Fig. 43 shows the hydraulic jump and the crater diameter for a jet impingement case.

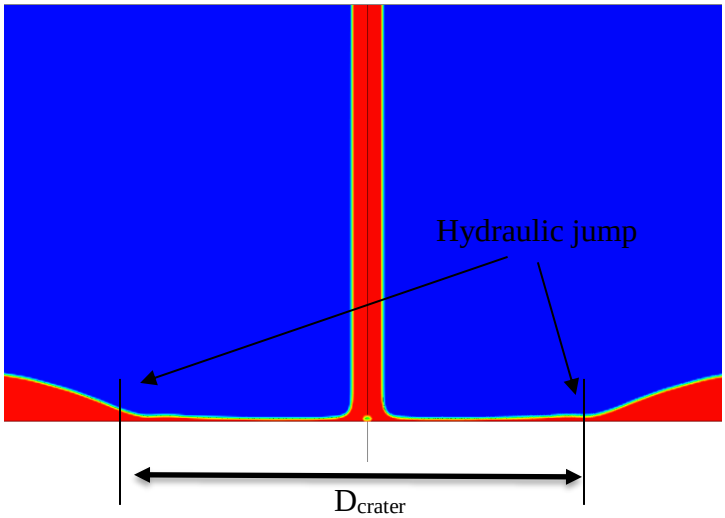


Figure 43. Location of crater diameter and hydraulic jump for jet impingement case

Crater Diameter for Comparison A and Comparison B are shown in Table 15. Droplet Train impingement formed larger craters compared to jet impingement cases. This is due to the higher velocity and impact momenta of the droplets.

Table 15. Crater diameter values from CFD results

| | **Comparison A (180 ml/hr. – 3.6 W/cm$^2$)** | | **Comparison B (210 ml/hr. – 3.6 W/cm$^2$)** | |
|---|---|---|---|---|
| | **Jet** | **Droplet Train** | **Jet** | **Droplet Train** |
| Crater Diameter (µm) | 1381.8 | 2428 | 1773 | 2632 |

4.3.1.3 Resultant velocity

Maximum velocity of the fluid was found at the liquid-air interface. Fig 44 shows the location of the liquid-air interface for jet impingement. These velocities were averaged over time and plotted against the radial position, as shown in Fig. 45 and Fig. 46. It can be observed that droplet impingement flow has higher velocities, as compared to jet impingement, and show wider spread. This trend supports the previous finding of large crater diameters of droplet impingement cases as compared to jet impingement cases. For higher flowrates, the crater diameters were larger for both cooling methods.

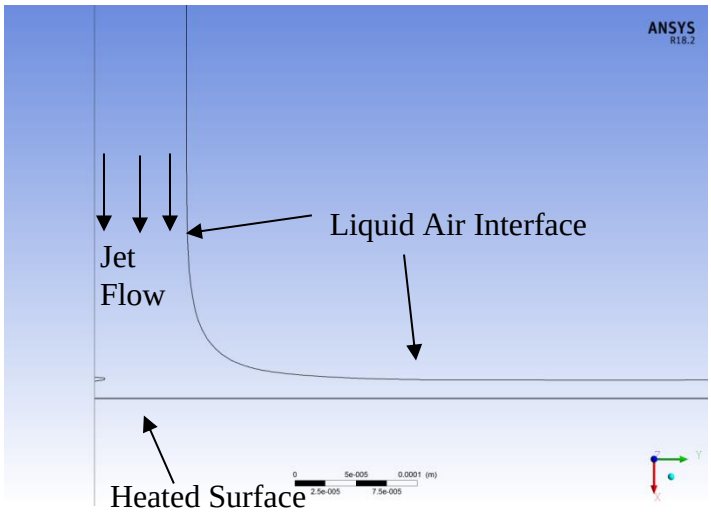


Figure 44. Liquid air interface for jet impingement – location of time averaged velocities

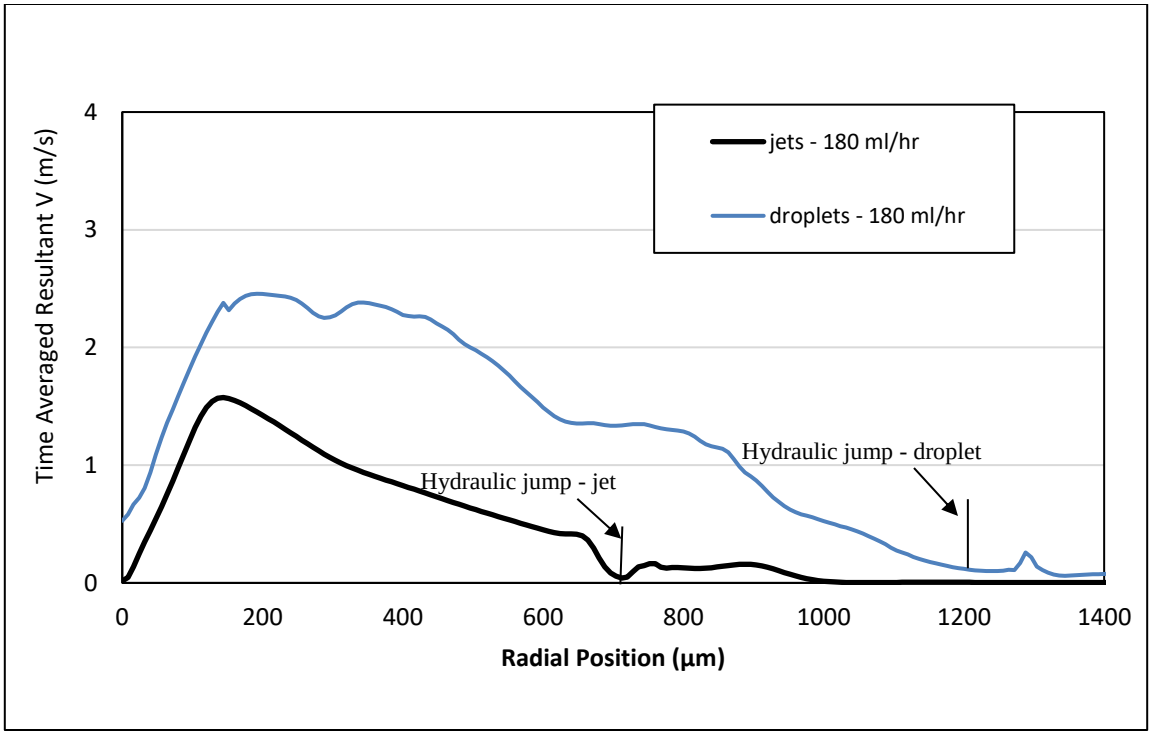


Figure 45. Velocity values for jet impingement and droplet impingement at the liquid-air interface (Comparison A - 180 ml/hr. - 3.6 W/cm$^2$)

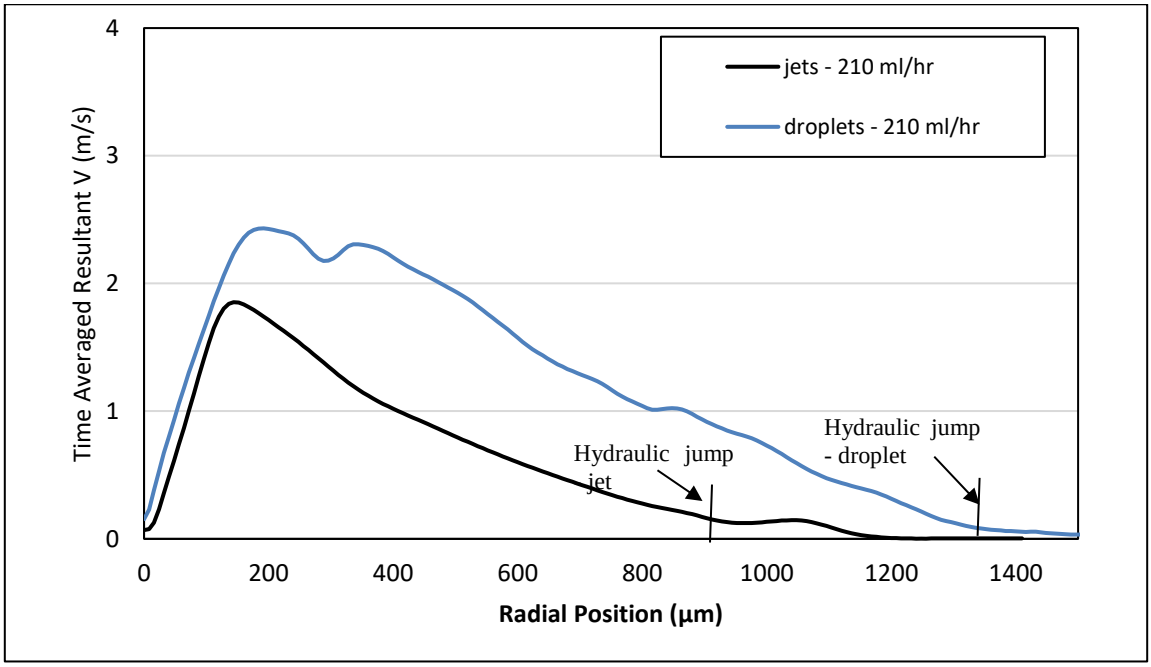


Figure 46. Velocity values for jet impingement and droplet impingement at the liquid-air interface (Comparison B - 210 ml/hr. - 3.6 W/cm$^2$)

4.3.1.4 Radial velocity

Radial velocity is the dominant component of velocity for both types of cooling techniques. Fig. 47 and Fig. 48 show the variation of time averaged radial velocity against radial position for jet impingement and droplet impingement. Similar trends to resultant velocity are observed for both flow rates. The fluid velocity initially rises as the fluid starts spreading radially after the impingement. Droplet impingement results in higher fluid velocities close the impingement zone. As the fluid spreads out, a gradual decrease is observed for both cooling techniques. A smoother velocity profile is observed in jet impingement, as compared to droplet impingement. Droplet impingement profile show a similar behavior but with slight variations, signifying the periodic nature of flow. As expected, Fig. 47 has higher velocities due to higher flow rates

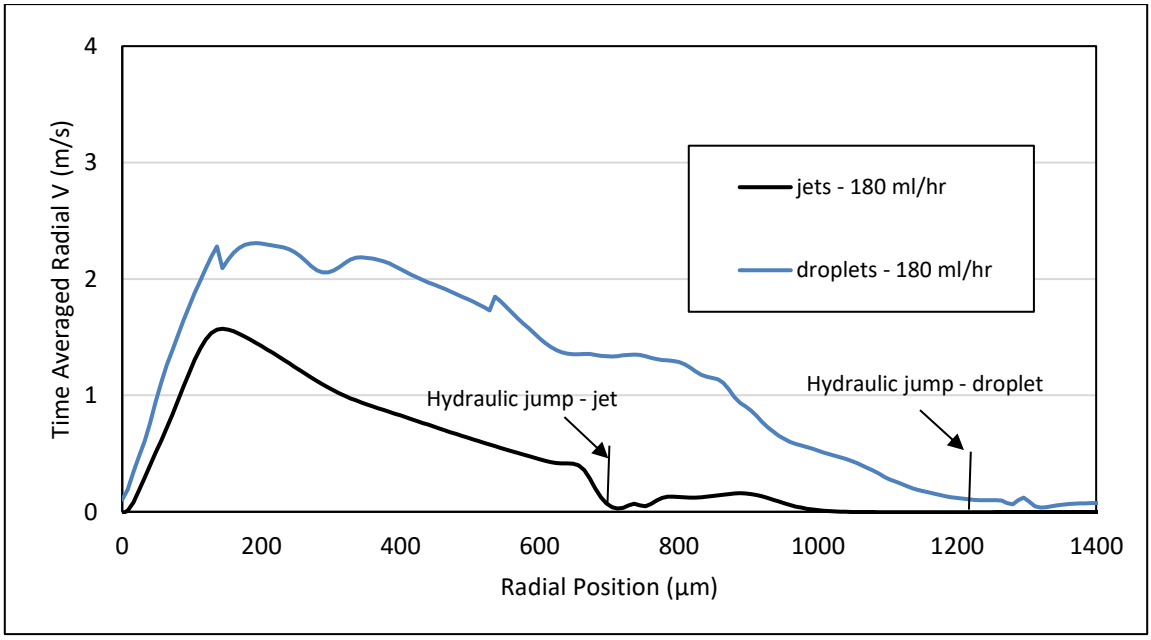


Figure 47. Time Averaged radial velocity at the liquid-air interface for jet and droplet impingement cases (Comparison A - 180 ml/hr. - 3.6 W/cm$^2$)

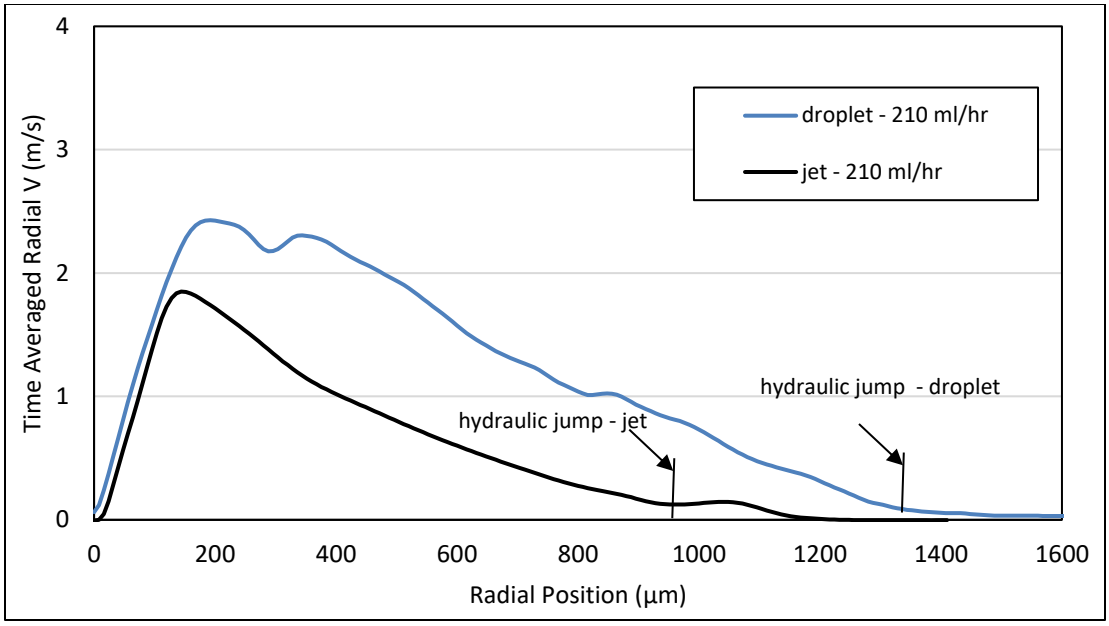


Figure 48. Time Averaged radial velocity at the liquid-air interface for jet and droplet impingement cases (Comparison B - 210 ml/hr. - 3.6 W/cm$^2$)

4.3.1.5 Axial velocity

Fig. 49 and Fig. 50 show the time averaged axial velocity trends at the liquid air interface. As expected, the axial velocity for jet impingement dies out within $3*r_j$ (radius of jet), as the fluid turns and starts flowing in the radial direction. For droplet impingement, the axial velocity component is much higher and spreads wider as compared to droplet impingement. This is due to larger diameter of the droplet, as compared to jets. After impingement, droplet spreads and forms a crown, which results in noticeable axial components of the velocity, up to the crown diameter. As the fluid reaches hydraulic jump in both types of fluid flow, abrupt variations in velocities were observed. Higher axial velocities are observed in Fig. 50 as the flow rate increases.

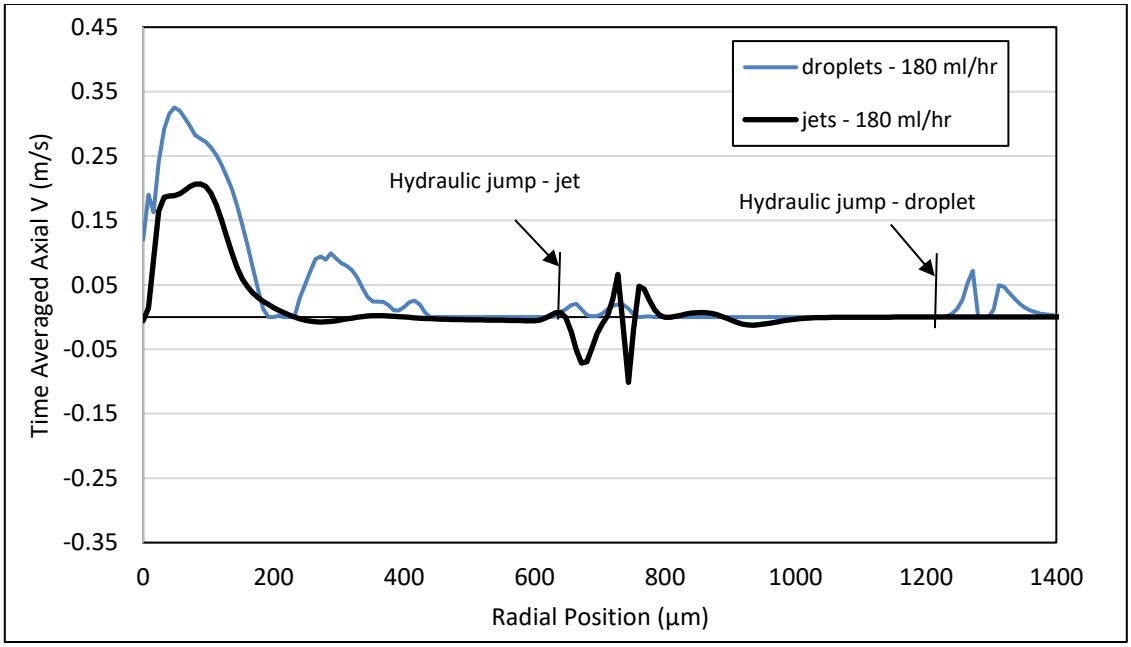


Figure 49. Time Averaged axial velocity at the liquid-air interface for jet and droplet impingement cases (Comparison A - 180 ml/hr. - 3.6 W/cm$^2$)

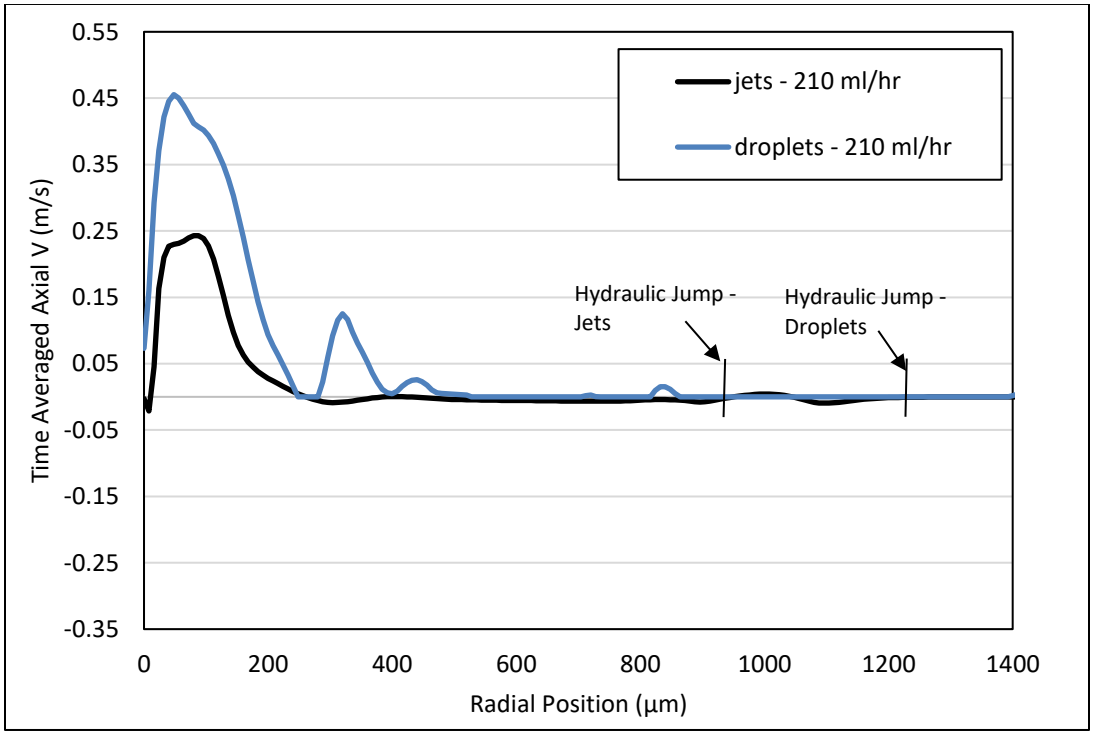


Figure 50. Time Averaged axial velocity at the liquid-air interface for jet and droplet impingement cases (Comparison B - 210 ml/hr. - 3.6 W/cm2)

4.3.1.6 Momentum

Two better understand the effect of hydrodynamics on heat transfer, a time averaged radial momentum was calculated for both jet impingement and droplet impingement. For estimating time averaged radial momentum, the liquid mass associated with the radial element (10 μm in width) was first calculated at each discrete radial location, as shown in Fig. 52.

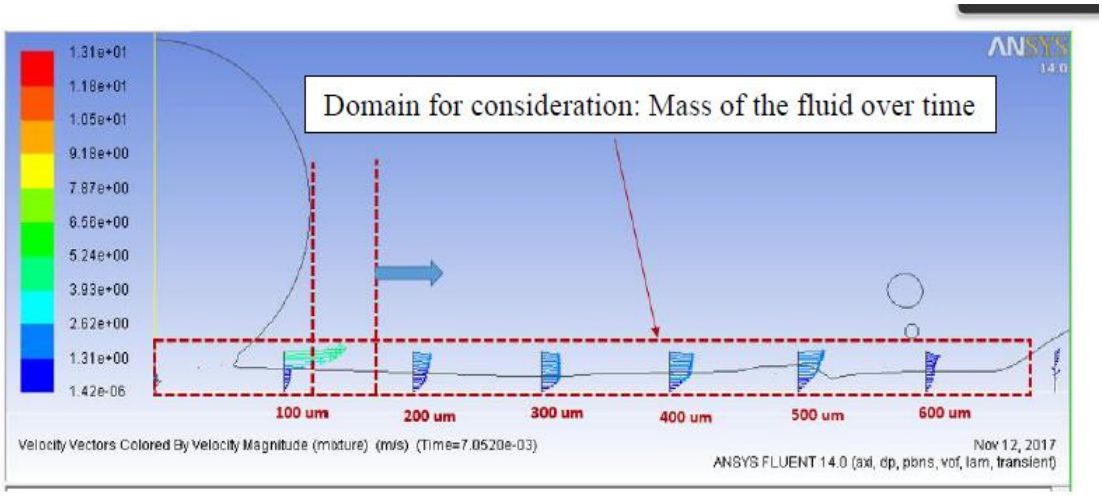


Figure 51. Method for calculating the radial momentum at discrete points within the impingement zone for droplet train impingement. Reprinted from Muthusamy [24]

The mass weighted integral of liquid volume fraction in the area of consideration was calculated using a custom field function using ANSYS-Fluent. Only the liquid volume fraction of 1 was considered for mass calculations. The resultant momentum at a particular time instant was calculated using equation (19):

$$M(r,t) = \int_{i=1}^{n} m(r,t).\vec{v}(r,t) \tag{19}$$

The elemental liquid mass and the face velocity of each cell confined between the wall and the corresponding liquid-gas interface were used to estimate local fluid

momentum. These momentum values were then time averaged over the course of each simulation. Fig. 52 and Fig. 53 show the momentum variation along the radial distance. It can be observed that as the fluid spreads radially, momentum decreases gradually. A sharp change in momentum is observed in the jet impingement case due to the hydraulic jump. Hydraulic jumps cause the fluid to slow down, thus reducing the momentum as well. As the flow rate increases, the momentum increase is noticeable in both jet and droplet train flows.

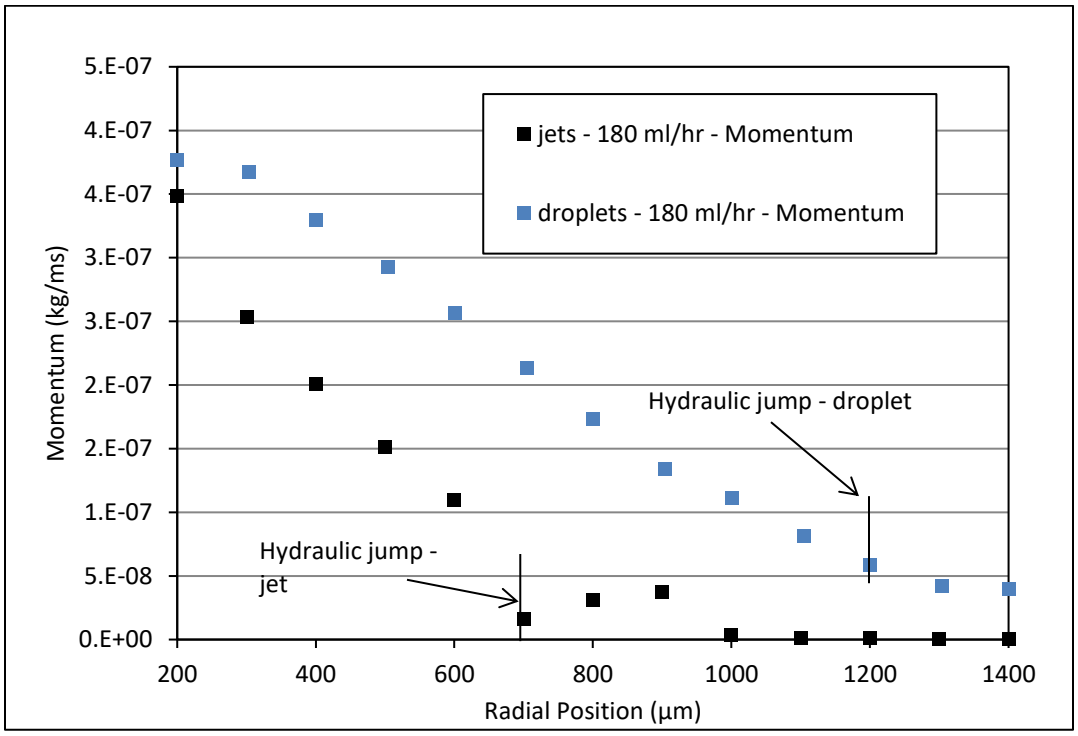


Figure 52. Time Averaged momentum for jet impingement and droplet impingement cases (Comparison A - 180 ml/hr. - 3.6 W/cm$^2$)

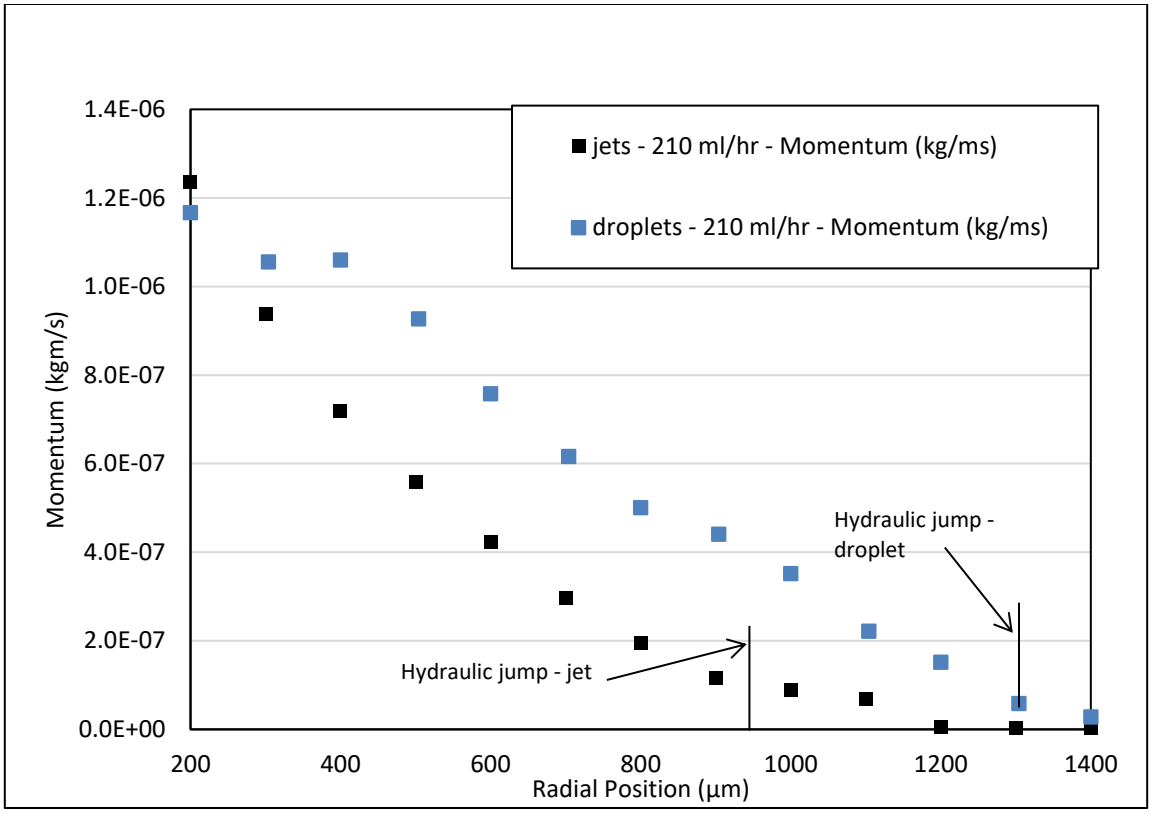


Figure 53. Time Averaged momentum for jet impingement and droplet impingement cases (Comparison B - 210 ml/hr. - 3.6 W/cm$^2$)

*4.3.2 Comparison of heat transfer behavior*

The effectiveness of each liquid impingement as a surface cooling technique is discussed in this section.

4.3.2.1 Temperature profile

Temperature profile across the heated surface for Comparison A is shown in Fig. 54. Surfaces under the effect of droplet impingement showed lower surface temperatures as compared to jet impingement cases. A maximum different of 7 °C can be observed from Fig. 54. It can also be noted that droplet impingement formed a smoother, uniform profile as compared to jet impingement. Also, jet impingement profile shows a sharper gradient in temperature after the hydraulic jump. Similar observations were made from temperature profiles of comparison B, shown in Fig. 55.

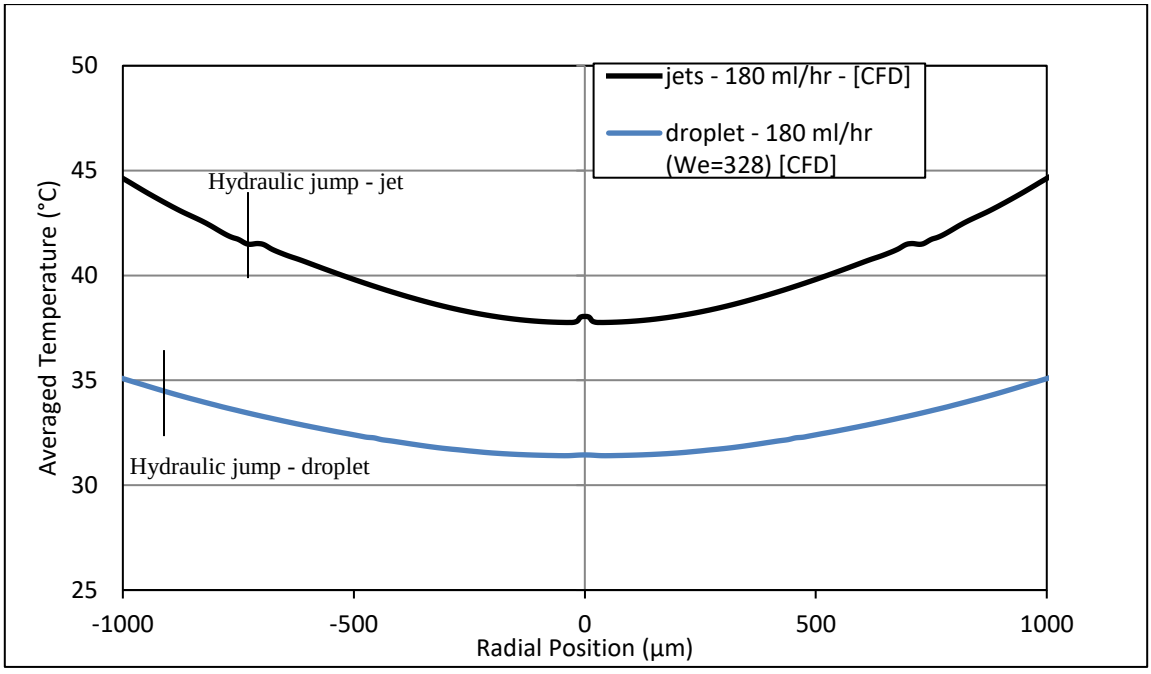


Figure 54. Comparison of temperature profiles along the heated surface for Comparison A (180 ml/hr. - 3.6 W/cm$^2$)

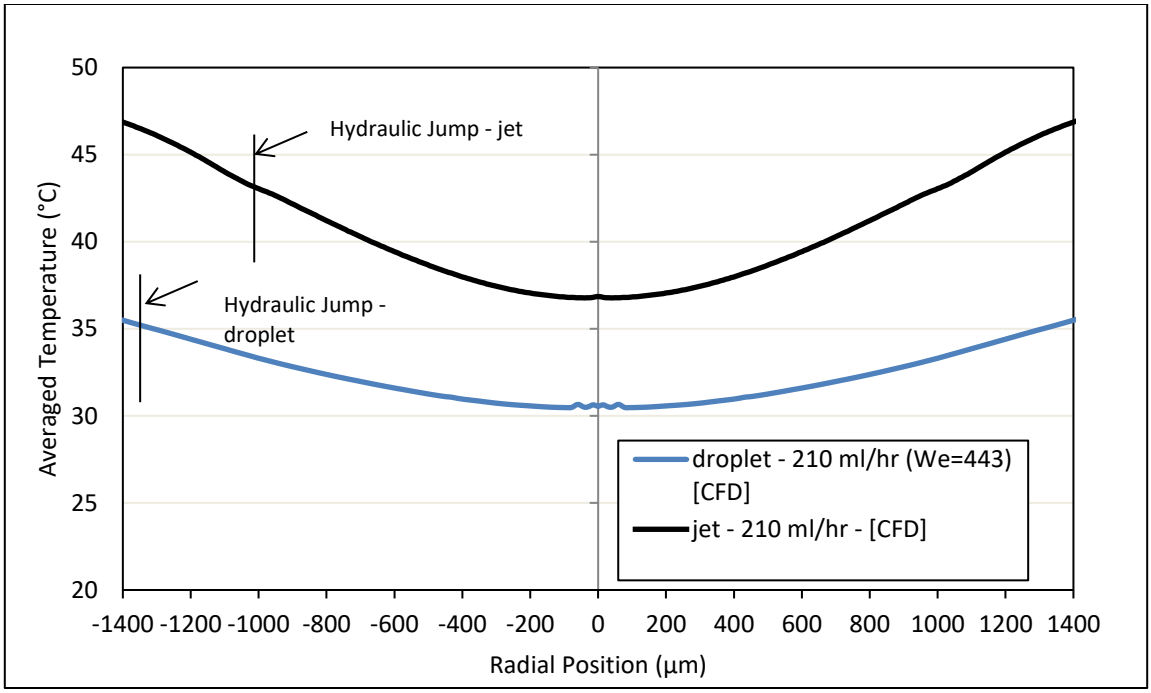


Figure 55. Comparison of temperature profiles along the heated surface for Comparison B (210 ml/hr. - 3.6 W/cm$^2$)

4.3.2.2 Nusselt number

Nusselt number comparison of jet and droplet impingement is shown in Fig. 56 and Fig. 57. The variation of the dimensionless number along the heated surface concurs with the temperature profile shown in Fig. 55 and Fig. 56. Highest Nusselt number values occur at the stagnation point, corresponding to lowest temperatures occurring in this region. As the fluid spread radially and fluid momentum is lost, and heat transfer reduced gradually. Droplet impingement has higher Nusselt numbers than jet impingement, indicating better heat transfer performance of the cooling technique for the same fluid flowrate. An increase in flow rate resulted in increase in the Nusselt number, in both impingement cooling techniques. However, jet impingement with higher flow rate did not perform as well as the droplet impingement with lower flow rate.

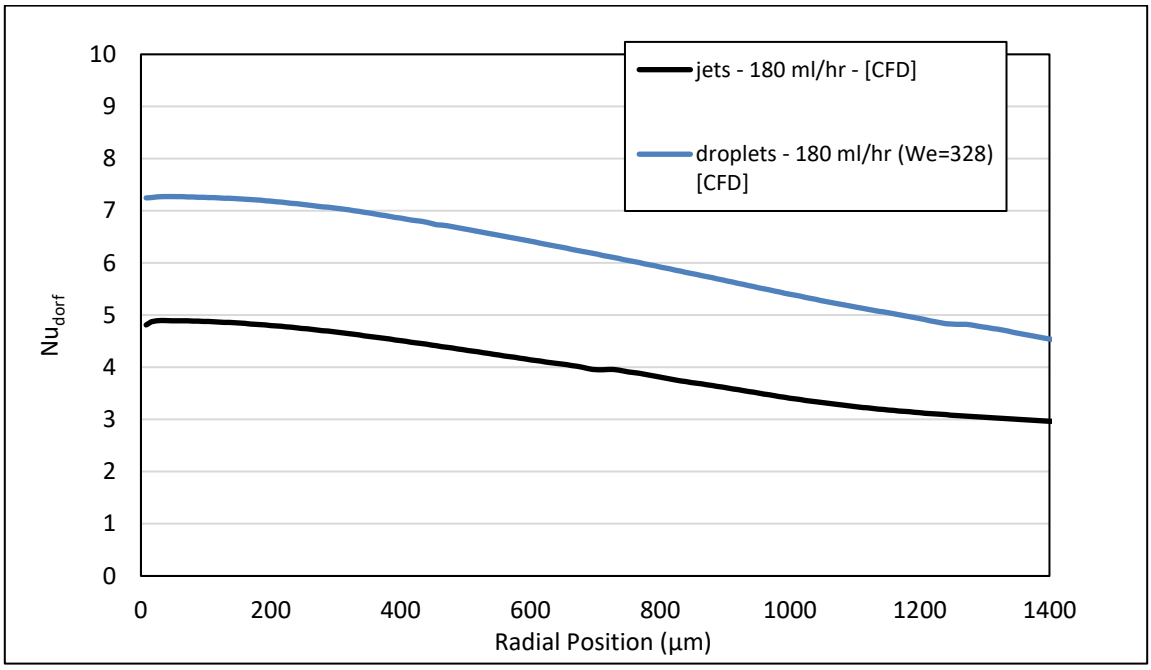


Figure 56. Nusselt number comparison for jet impingement and droplet impingement (Comparison A - 180 ml/hr. - 3.6 W/cm$^2$)

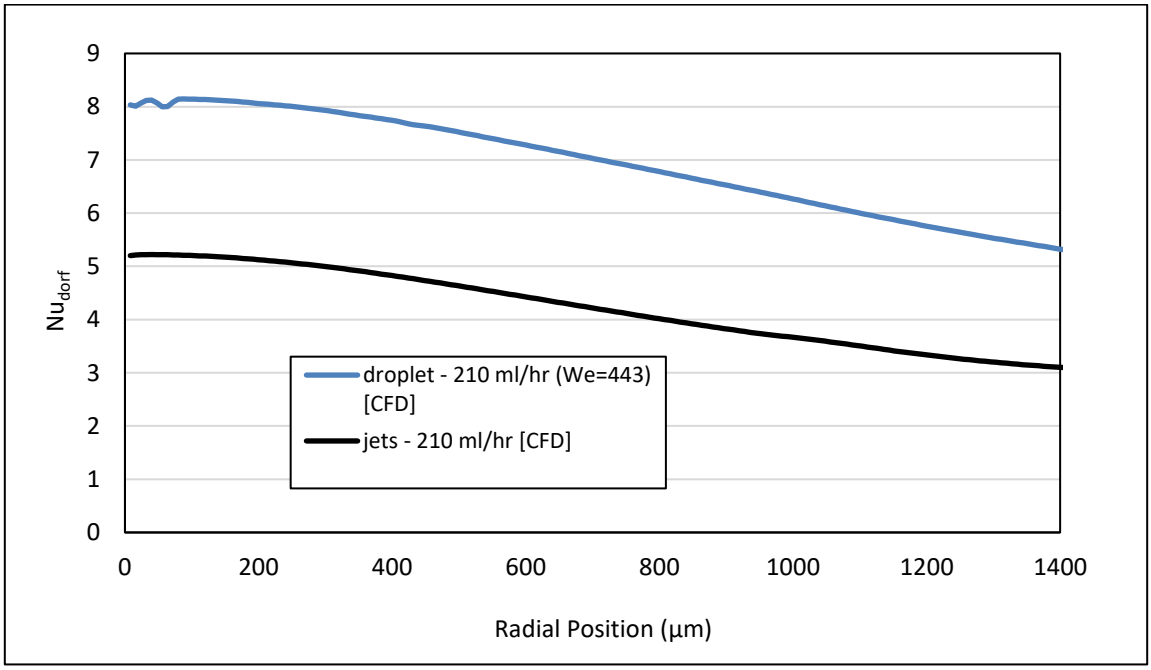


Figure 57. Nusselt number comparison for jet impingement and droplet impingement (Comparison B - 210 ml/hr. - 3.6 W/cm$^2$)

4.3.2.3 Heat Transfer Coefficient

Heat transfer coefficients for jet impingement and droplet impingement are shown in Fig. 58 and Fig. 59. Heat transfer coefficient values are higher for the droplet impingement case, as compared to jet impingement. Maximum difference of 35% was observed in heat transfer coefficient between jets and droplets in comparison A. In comparison B, a difference of 32% was noted. An increase in flow rate resulted in an increase of 10% in the heat transfer coefficient value for both, jet and droplet impingement.

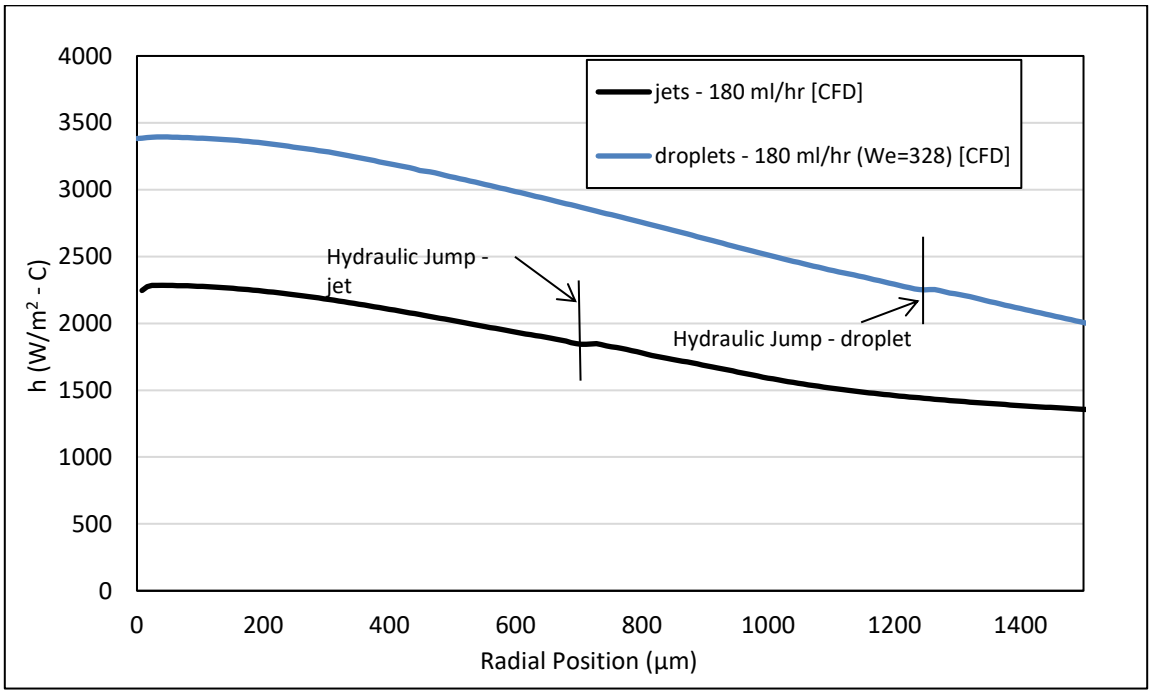


Figure 58. Heat transfer coefficient comparison for jet impingement and droplet impingement (Comparison A - 180 ml/hr. - 3.6 W/cm$^2$)

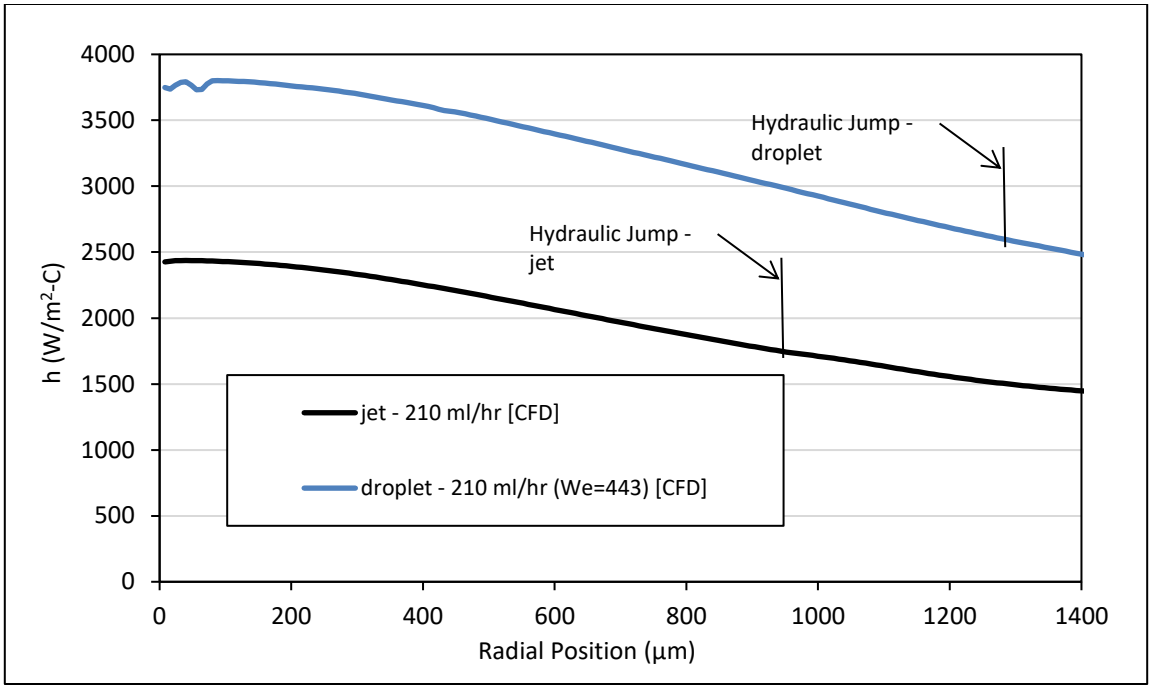


Figure 59. Heat transfer coefficient comparison for jet impingement and droplet impingement (Comparison B - 210 ml/hr. - 3.6 W/cm$^2$)

#### 4.3.2.4 Reason for better heat transfer performance of droplet impingement cooling

From all the previous plots, it is evident that heat transfer performance of droplet train impingement cooling is better than in jet impingement cooling. To gain a better understanding, momentum calculations, done in the previous section, were compared with the temperature profiles for jet impingement and droplet impingement. Fig. 60 and Fig. 61 show the trends for jet impingement and droplet impingement.

It can be seen from both figures that the changes in temperature profile occurs at locations where there is a change in momentum. In Fig 60, once the momentum drops after the hydraulic jump, the temperature values increase rapidly. Similar behavior can be observed in Comparison A and Comparison B. Therefore, it can be stated that the heat transfer is momentum driven in both cooling techniques. As shown previously, droplets have higher momentum, which leads to better heat transfer performance compared to droplets. A closer observation of these plot reveals how the temperature gradient depends on the momentum gradient. For jet impingement, the reduction in momentum is steep which leads to a sharper temperature rise. Droplet train impingement momentum loss is slower and thus results in a small temperature gradient. Similar behavior is observed in Fig. 61.

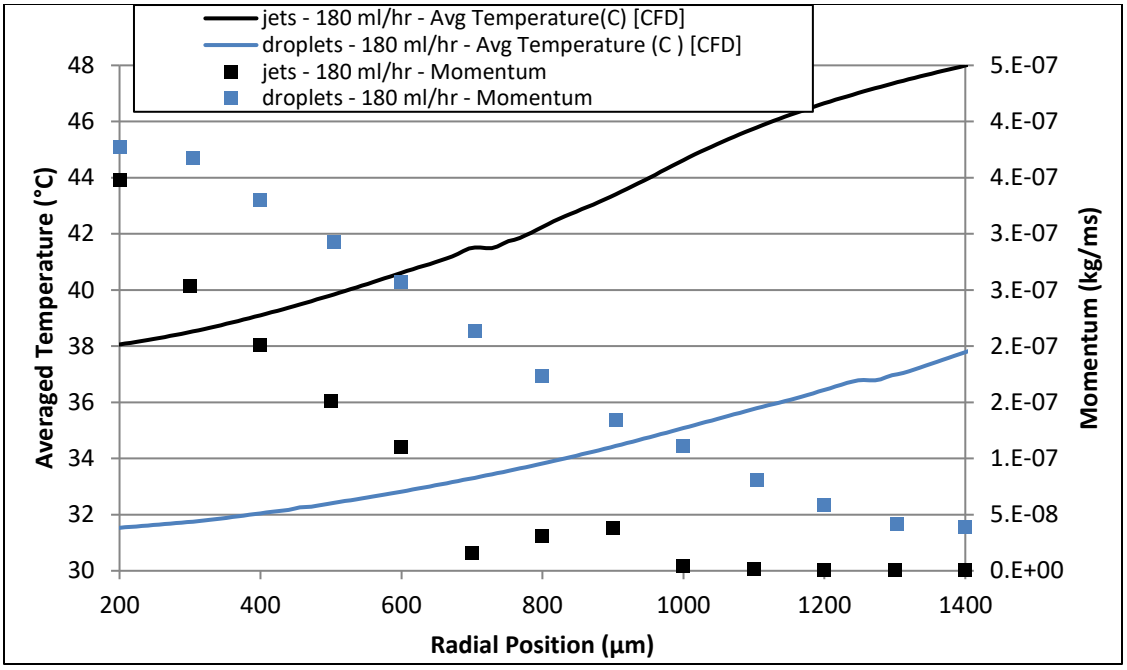


Figure 60. Averaged temperature and Averaged momentum compared for jet impingement case 1 (180 ml/hr. - 3.6 W/cm$^2$) and droplet impingement case 3 (180 ml/hr. - 3.6 W/cm$^2$ – We=328)

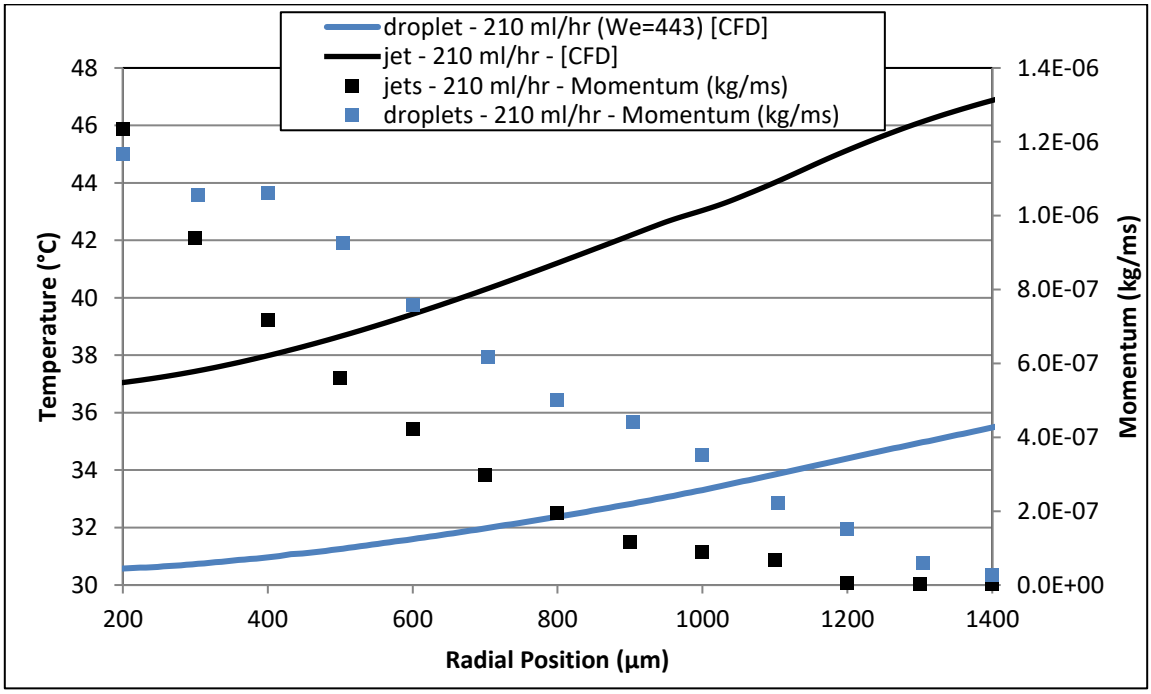


Figure 61. Averaged temperature and Averaged momentum compared for jet impingement case 2 (210 ml/hr. - 3.6 W/cm$^2$) and droplet impingement case 4 (210 ml/hr. - 3.6 W/cm$^2$ – We=443)

4.3.2.5 Thermal boundary layer, hydrodynamic boundary layer and averaged film thickness

Thermal boundary layer is another indicator of heat transfer performance. A thin boundary layer indicates better heat transfer. For calculating thermal boundary layer thickness, equation (20) was used

$$\delta_{Tdt} = \int_0^{r_d/2} \frac{T(r,z) - T_D}{T_w(r) - T_D}\, dz \tag{20}$$

Thermal boundary layers were plotted for jet impingement and droplet impingement cases, as shown in Fig. 62 and Fig. 63. As expected, droplet impingement case had a thinner thermal boundary layer compared to jet impingement for both identical flow rates. This is attributed to the higher momentum of droplet impingement.

A hydrodynamic boundary layer was used to further understand the behavior of fluid and heat transfer behavior. Hydrodynamic boundary layer was calculated using equation (21)

$$\delta^* = \int_0^{\infty} \left(1 - \frac{u_y}{u_0}\right) dy \tag{21}$$

For jet impingement, the hydrodynamic boundary layer calculation showed that it grew up to the film thickness within $r/r_j < 2$. Therefore, it was ideal to consider the average film thickness of the fluid inside the crater diameter as the hydrodynamic boundary layer. For both jet impingement cases, the hydrodynamic boundary layer was greater than thermal boundary layer within the crater. A separation occurs after the crater diameter and is not considered here.

Droplet impingement cooling had a periodic behavior; therefore the hydrodynamic boundary layer development was time dependent. In most instances, it reached the film thickness by $r/r_j=1.5$. To simplify the study, an average film thickness was used as the reference for boundary layer. Thermal boundary layer of droplet stream varied between 0~2 μm, and at least two times thinner than jet impingement boundary thermal boundary layer. It was also observed that difference between thermal boundary layer and film thickness of droplets was much larger, compared to jet impingement; however, it should be noted than the film thickness is highly transient in the droplet impingement case. The thermal boundary layer for droplet impingement cases remained low for longer period of time than in the jet impingement cases, and abruptly increasing once the fluid reached the hydraulic jump. In both cooling techniques, the thermal boundary layer is smaller than the hydrodynamics boundary layer, which leads a Prandtl number greater than unity, as expected from liquids.

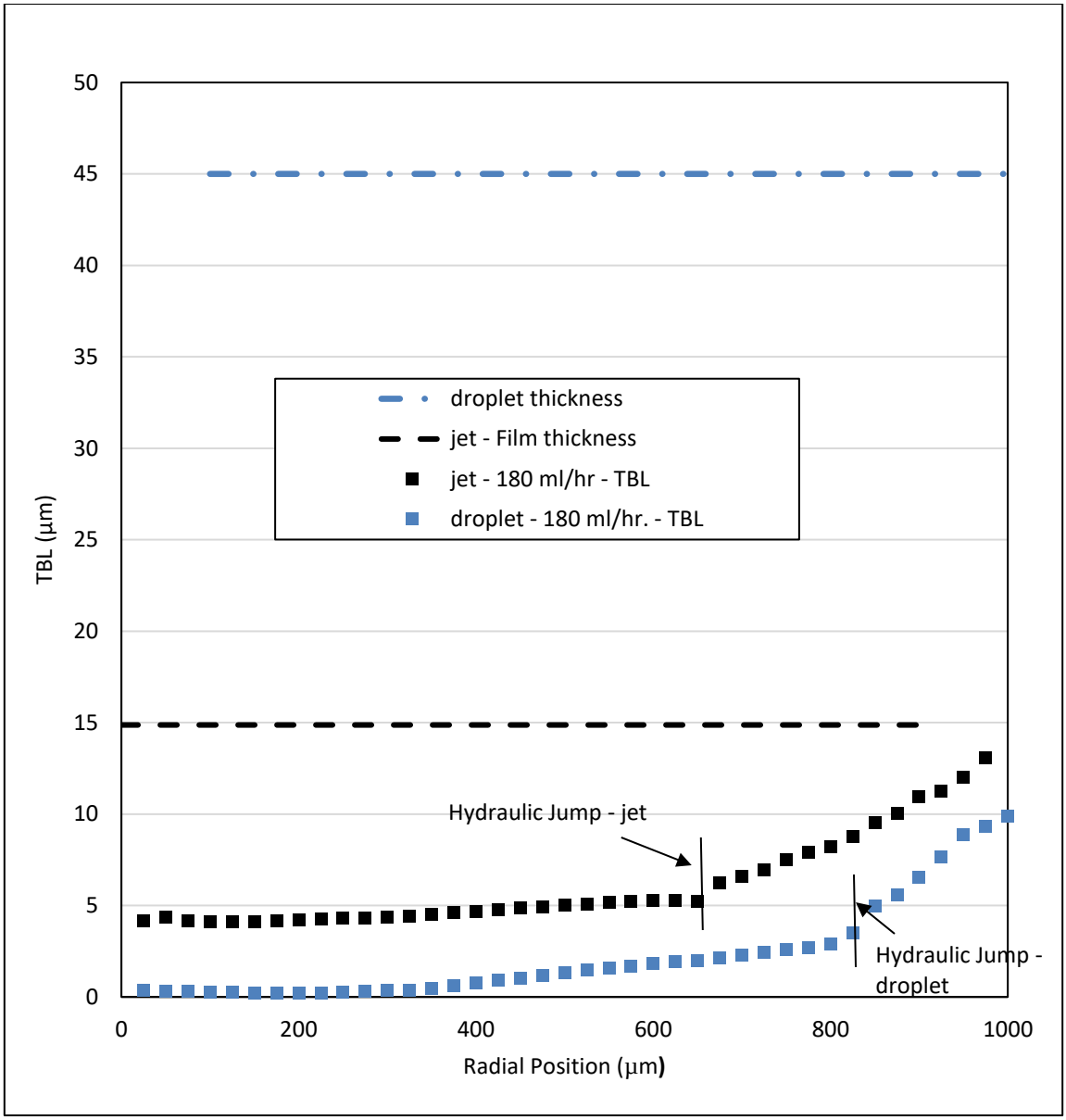


Figure 62. Thermal boundary layer profiles for jet impingement and droplet train impingement (Comparison A - 180 ml/hr. - 3.6 W/cm$^2$)

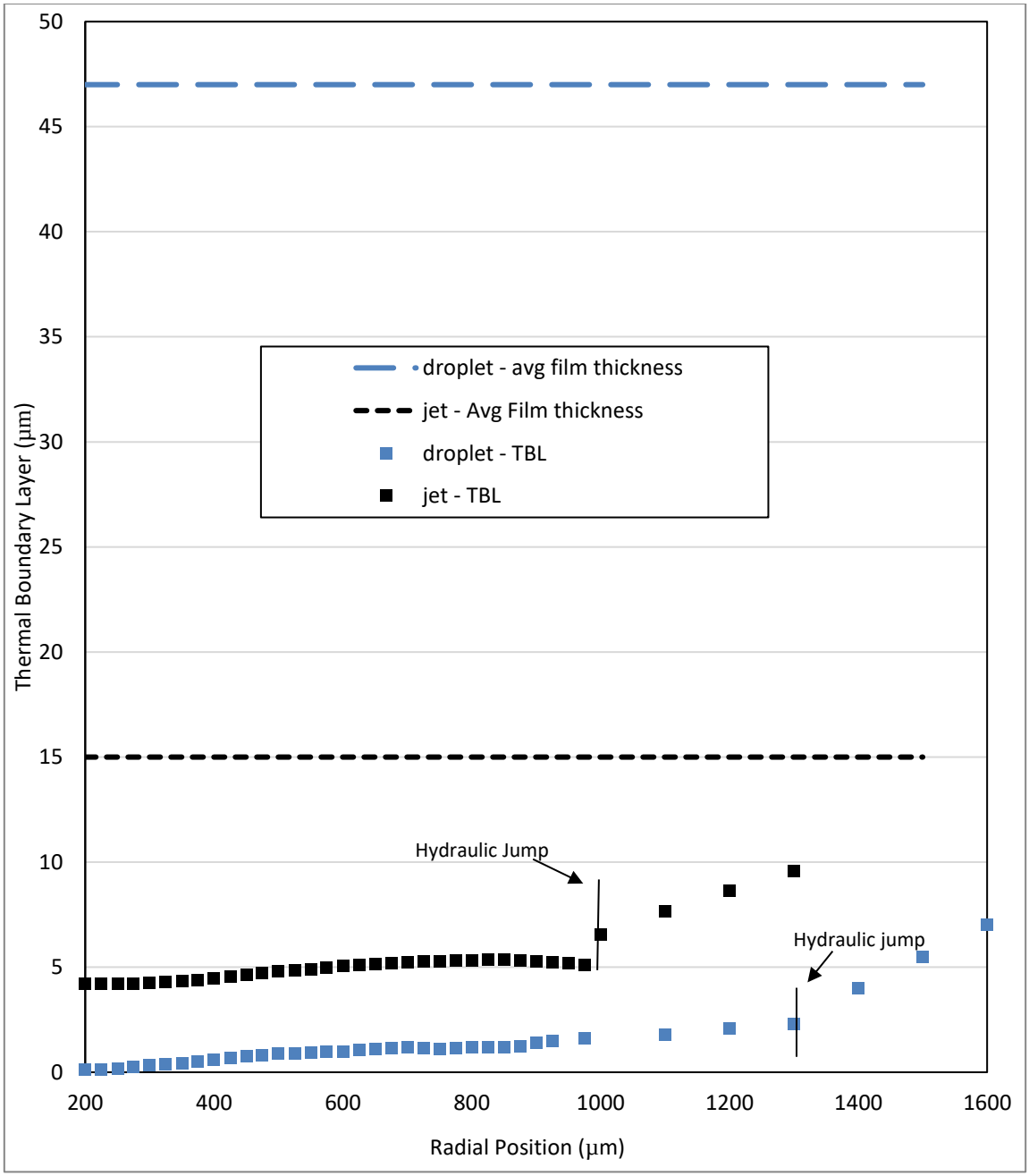


Figure 63. Thermal boundary layer profiles for jet impingement and droplet train impingement (Comparison B - 210 ml/hr. - 3.6 W/cm2)

# CHAPTER V

# CONCLUSIONS AND RECOMMENDATIONS

## 5.1 Conclusions from comparative study of jet impingement and droplet impingement cooling

The primary object of this study was to investigate and compare the heat transfer performance of jet impingement and droplet impingement cooling techniques. CFD simulations and results obtained were validated with experimental data available from Zhang [1]. The CFD results were then utilized to compare the cooling techniques

### *5.1.1 Concluding Remarks*

From the comparative study, following conclusions can be drawn:

1. It was found that heat transfer performance of monodispersed droplet impingement was better than jet impingement for the same flow rate and heat flux values.
2. Improved performance of droplet train impingement was due to the convective heat transfer across the surface, which was driven by fluid momentum. Although, at the same flow rate, droplets had a higher momentum due to their periodic impingement nature.
3. A more uniform spread of temperature was observed across the heated surface from the droplet impingement cooling, as compared to jet impingement
4. Thermal boundary layer for jet impingement was thicker than the thermal boundary layer for droplet impingement, indicating better heat transfer

from the latter. Hydrodynamic boundary layer for both impingement techniques was greater than thermal boundary layer.

5. As the fluid approached the hydraulic jump, a significant decrease in radial velocity and momentum was observed for both cooling techniques.
6. Highest heat transfer coefficients were observed at the center of the impingement zone, resulting in the lower temperatures. This region is defined as the stagnation zone.
7. Axial velocities are observed close to the impingement zone as the fluid is turning in both fluid flows. These values gradually reduce and become negligible by $r/r_j=6$.

## 5.2 Recommendation for future work

Based on the current level of understanding and results from this present study, the following suggestions for future studies are proposed:

1. Comparative studies of jets and droplets, that vary droplet parameters such as droplet spacing, frequency and jet impingement parameters such as nozzle diameter, should be performed for the same flow rates.
2. Studies involving turbulent flows in jets and droplets at greater Reynolds number after impingement need to be performed to study the effect of turbulence on heat transfer performance.
3. All the simulations in this study assumed that there is no phase change due to the lower heat flux assumption. However, future studies can explore the effects of higher heat flux heat transfer rates with phase change mechanisms such as boiling/evaporation.
4. To better simulate practical situations, studies involving heat surface boundary conditions, other than constant heat flux, should be conducted.

# REFERENCES


1. Zhang, T., *Study Of Hydrodynamics And Heat Transfer Induced By Multiple Droplet Train Impingements*, in *Mechanical Engineering*. 2017, Texas A&M University. p. 192.

2. Moore, G., *Cramming more components onto integrated circuits.* Electronics, 1965. **38**: p. 114-117.

3. Chaudhari, M., B. Puranik, and A. Agrawal, *Heat transfer characteristics of synthetic jet impingement cooling.* International Journal of Heat and Mass Transfer, 2010. **53**(5): p. 1057-1069.

4. Mudawar, I., *Assessment of high-heat-flux thermal management schemes.* 2000: p. 1-20.

5. Lienhard, J.H., *Heat Transfer by Impingement of Circular Free-Surface Liquid Jets.* 2005.

6. *Spray cooling*. Available from: http://www.directindustry.es/fabricante-industrial/boquilla-pulverizacion-146983-_2.html.

7. Bolle, L. and J.C. Moureau, *Theory and Application on Spray Cooling of Hot Surfaces.* Multiphase Science and Technology, 2016. **28**(4): p. 321-417.

8. Faghri, A., S. Thomas, and M.M. Rahman, *Conjugate Heat Transfer From a Heated Disk to a Thin Liquid Film Formed by a Controlled Impinging Jet.* Journal of Heat Transfer, 1993. **115**(1): p. 116.

9. Monde, M. and Y. Katto, *Burnout in a high heat-flux boiling system with an impinging jet.* International Journal of Heat and Mass Transfer, 1978. **21**(3): p. 295-305.

10. Moriyama, A., et al., *Local heat-transfer coefficient in spray cooling of hot surface.* Transactions of the Iron and Steel Institute of Japan, 1988. **28**(2): p. 104-109.

11. Wachters, L.H.J., et al., *The heat transfer from a hot wall to impinging mist droplets in the spheroidal state.* Chemical Engineering Science, 1966. **21**(12): p. 1231-1238.

12. Lewis, S.R., L. Anumolu, and M.F. Trujillo, *Numerical simulations of droplet train and free surface jet impingement.* International Journal of Heat and Fluid Flow, 2013. **44**: p. 610-623.

13. Watson, E.J., *The radial spread of a liquid jet over a horizontal plane.* Journal of Fluid Mechanics, 2006. **20**(3): p. 481-499.

14. Azuma, T. and T. Hoshino, *The Radial Flow of a Thin Liquid Film : 2nd Report, Liquid Film Thickness.* Bulletin of JSME, 1984. **27**(234): p. 2747-2754.

15. Chen, S.-J. and A.A. Tseng, *Spray and jet cooling in steel rolling.* International Journal of Heat and Fluid Flow, 1992. **13**(4): p. 358-369.

16. Seraj, M., & Gadala, *Numerical Assessments of Impingement Flow over Flat Surface due to Single and Twin Circular Long Water Jets.* Transaction Series on Engineering Sciences and Technologies, 2012. **1**(7).

17. Parneix, S., M. Behnia, and P.A. Durbin, *Predictions of Turbulent Heat Transfer in an Axisymmetric Jet Impinging on a Heated Pedestal.* Journal of Heat Transfer, 1999. **121**(1): p. 43-49.

18. 阎晓君著 and 闫晓君, *出土文献与古代司法检验史研究*. Di 1 ban. ed. Kao gu xin shi ye cong shu. 2005, Beijing: Wen wu chu ban she.

19. Liu, X., V.J.H. Lienhard, and J.S. Lombara, *Convective Heat Transfer by Impingement of Circular Liquid Jets.* Journal of Heat Transfer, 1991. **113**(3): p. 571-582.

20. Narumanchi, S., V. Hassani, and D. Bharathan, *Modeling Single-Phase and Boiling Liquid Jet Impingement Cooling in Power Electronics*. 2005.

21. Womac, D.J., S. Ramadhyani, and F.P. Incropera, *Correlating Equations for Impingement Cooling of Small Heat Sources With Single Circular Liquid Jets.* Journal of Heat Transfer, 1993. **115**(1): p. 106-115.

22. Morris, G.K., S.V. Garimella, and R.S. Amano, *Prediction of Jet Impingement Heat Transfer Using a Hybrid Wall Treatment With Different Turbulent Prandtl Number Functions.* Journal of Heat Transfer, 1996. **118**(3): p. 562-569.

23. Garimella, S.V. and R.A. Rice, *Confined and Submerged Liquid Jet Impingement Heat Transfer.* Journal of Heat Transfer, 1995. **117**(4): p. 871-877.

24. muthusamy, J., *Numerical Investigation Of Thermo-Hydrodynamics Of Multiple Droplet Train Impingement For Surface Cooling*, in *Mechanical Engineering*. 2018, Texas A&M University. p. 192.

25. Angioletti, M., E. Nino, and G. Ruocco, *CFD turbulent modelling of jet impingement and its validation by particle image velocimetry and mass transfer*

*measurements.* International Journal of Thermal Sciences, 2005. **44**(4): p. 349-356.

26. Bush, J.W.M. and J.M. Aristoff, *The influence of surface tension on the circular hydraulic jump.* Journal of Fluid Mechanics, 2003. **489**: p. 229-238.

27. Sussman, M. and E.G. Puckett, *A Coupled Level Set and Volume-of-Fluid Method for Computing 3D and Axisymmetric Incompressible Two-Phase Flows.* Journal of Computational Physics, 2000. **162**(2): p. 301-337.

28. Lorenzini, D. and Y. Joshi, *Comparison of the Volume of Fluid and CLSVOF Methods for the Assessment of Flow Boiling in Silicon Microgaps.* Journal of Heat Transfer, 2017. **139**(11): p. 111506-111506-10.

29. Incropera, F.P. and D.P. DeWitt, *Fundamentals of heat and mass transfer*. 5th ed. ed. 2002, New York: J. Wiley.

30. Chen, R.-H., L.C. Chow, and J.E. Navedo, *Effects of spray characteristics on critical heat flux in subcooled water spray cooling.* International Journal of Heat and Mass Transfer, 2002. **45**(19): p. 4033-4043.

31. Chen, R.-H., L.C. Chow, and J.E. Navedo, *Optimal spray characteristics in water spray cooling.* International Journal of Heat and Mass Transfer, 2004. **47**(23): p. 5095-5099.

32. Cheng, W.-L., et al., *Experimental and theoretical investigation of surface temperature non-uniformity of spray cooling.* Energy, 2011. **36**(1): p. 249-257.

33. Mudawar, I. and K.A. Estes, *Optimizing and Predicting CHF in Spray Cooling of a Square Surface.* Journal of Heat Transfer, 1996. **118**(3): p. 672-679.

34. Haas, G. and A.P. Wemhoff, *Nano-Droplet Impingement Heat Transfer on a Solid Surface.* 2010(44441): p. 83-88.

35. Trujillo, M.F., et al., *Numerical Simulations and Experimental Characterization of Heat Transfer From a Periodic Impingement of Droplets.* Journal of Heat Transfer, 2011. **133**(12): p. 122201-122201-10.

36. Soriano, G.E., T. Zhang, and J.L. Alvarado, *Study of the effects of single and multiple periodic droplet impingements on liquid film heat transfer.* International Journal of Heat and Mass Transfer, 2014. **77**: p. 449-463.

37. Oliphant, K., B.W. Webb, and M.Q. McQuay, *An experimental comparison of liquid jet array and spray impingement cooling in the non-boiling regime.* Experimental Thermal and Fluid Science, 1998. **18**(1): p. 1-10.

38. Blazek, J., *Chapter 1 - Introduction*, in *Computational Fluid Dynamics: Principles and Applications (Third Edition)*, J. Blazek, Editor. 2015, Butterworth-Heinemann: Oxford. p. 1-5.

39. Slater, J.W. *CFD Analysis Process*. NPARC Alliance CFD Verification and Validation Website 2008 [cited 2018 08/15/18]; Available from: https://www.grc.nasa.gov/www/wind/valid/tutorial/process.html.

40. 3M. *3M™ Novec™ 7100 Engineered Fluid*. 2009 [cited 2018; Available from: http://multimedia.3m.com/mws/media/199818O/3mtm-novectm-7100-engineered-fluid.pdf.

41. Reddy, I.N., et al., *Development of SiO2 based thin film on metal foils for space application.* Ceramics International, 2013. **39**(7): p. 8493-8498.

42. Zhang, T., et al., *Numerical and experimental investigations of crown propagation dynamics induced by droplet train impingement.* International Journal of Heat and Fluid Flow, 2016. **57**: p. 24-33.

43. Zhang, T., *Study Of Hydrodynamics And Heat Transfer Induced By Multiple Droplet Train Impingements.* 2017.

44. Bohr, T., P. Dimon, and V. Putkaradze, *Shallow-water approach to the circular hydraulic jump.* Journal of Fluid Mechanics, 2006. **254**: p. 635-648.

45. Munson, B.R., D.F. Young, and T.H. Okiishi, *Fundamentals of fluid mechanics*. 5th ed. ed. 2006, Hoboken, NJ: J. Wiley & Sons.

46. White, F.M., *Heat and mass transfer*. 1988, Reading, Mass.: Addison-Wesley.

47. *Fluent User Guid*. Approaches to Multiphase flow modeling 2006; A complete manual of Fluent software]. Available from: https://www.sharcnet.ca/Software/Fluent6/html/ug/node876.htm.

48. Youngs, D., *Time-Dependent Multi-material Flow with Large Fluid Distortion*. Vol. 24. 1982. 273-285.